STUDY OF IRON OXIDE MAGNETIC NANOPARTICLES IN CANCER CELL DESTRUCTION AND CELL SEPARATION

by

Jiaqi Zhao

B.S., Dalian University of Technology, 2013

Submitted to the Graduate Faculty of

Swanson School of Engineering in partial fulfillment

of the requirements for the degree of

Doctor of Philosophy in Chemical Engineering

University of Pittsburgh

2018

UNIVERSITY OF PITTSBURGH

SWANSON SCHOOL OF ENGINEERING

This dissertation was presented

by

Jiaqi Zhao

It was defended on

November 16, 2017

and approved by

Robert M. Enick, Ph.D., Professor, Department of Chemical and Petroleum Engineering

Susan Fullerton, Ph.D., Assistant Professor, Department of Chemical and Petroleum Engineering

Dexing Zeng, Ph.D., Assistant Professor, Department of Medicine

Dissertation Director: Lei Li, Ph.D., Associate Professor, Department of Chemical and Petroleum Engineering

STUDY OF IRON OXIDE MAGNETIC NANOPARTICLES IN CANCER CELL DESTRUCTION AND CELL SEPARATION

Jiaqi Zhao, PhD

University of Pittsburgh, 2018

Due to their adjustable physiochemical properties and proven biocompatibility, iron oxide (Fe_3O_4) magnetic nanoparticles are promising in drug delivery, magnetic resonance imaging and catalysis. In this thesis, we have utilized two types of iron oxide nanoparticles: i) superparamagnetic iron oxide nanoparticles (SPION) for targeted destruction of cancer cells, and ii) poly(N-isopropylacrylamide) (pNIPAM) coated magnetic particles (MNP) for multistage cell separation.

SPION are generally considered as drug delivery vehicles for the enhanced permeability and retention (EPR) effect. SPION possess the intrinsic peroxidase-like activity as Horseradish peroxidase (HRP), which can generate reactive oxygen species (ROS) from H_2O_2 via Fenton's reaction. ROS regulate cell signaling, but a significant ROS stress can disrupt the redox homeostasis of cancer cells leading to selective tumor cell toxicity and destruction. Hereby, we developed ROS-induced targeted cell destruction with SPION-GOx bioconjugates platform. GOx catalyzes glucose oxidation in cancer cells to produce H_2O_2. 24 h incubation with 10 μg/mL SPION-GOx on 4T1 cells resulted in almost zero cell viability. *In vivo* evaluation showed SPION-GOx led to a much slower tumor growth compared to control groups.

Additionally, magnetic activated cell sorting (MACS) has become a common technique for the separation of target cell populations from biological suspensions. A major obstacle preventing current single stage MACS from achieving satisfying separation efficiency is the non-specific interactions between the cells and MNP. Thus, we designed a multistage separation platform similar to distillation concept in chemical engineering. The repeated capture-and-release separation process is enabled by attaching the temperature responsive polymer- pNIPAM to both MNP and target cells. We manipulate the reversible hydrophobic-hydrophilic interactions between such functionalized MNP and target cells through temperature cycling to capture and release target cells at a higher efficiency than non-target. After several temperature cycles, target cells are enriched in the product. Flow cytometry results suggest that A431 cells (target) could be effectively separated from HeLa cells (non-target) after three separation stages resulting in an enrichment factor of 3.69 when the starting ratio of target to non-target is 1:2.

TABLE OF CONTENTS

LIST OF TABLES

LIST OF FIGURES

PREFACE

Acknowledgement

I would like to thank my committee chair, Dr. Lei Li for his extraordinary mentoring and support. He showed me what the best mentor a student can ever have in his/her early life is like. He gave me hope and tremendous help when there were difficulties in the lab, in the classroom, and even in life. He guided me through the hard time. It was a privilege for me to have an advisor like Dr. Li.

Dr. Di Gao gave me the great opportunity to work on interesting projects with a group of most intelligent and kind people, especially with Dr. Dexing Zeng who worked with me side by side to instruct me. He is the best example of an enthusiastic and hardworking scientific researcher that pursues his dream no matter what.

I am very thankful that Dr. Susan Fullerton and Dr. Robert Enick gave me valuable advice and recommendations on my defenses and dissertation writing. This dissertation could not have been done without their kind understanding and guidance.

Last but not least, I am grateful for my friends, family, people cheering for me along the road. The last five years of my life has been wonderful because of them. And thank you, Bobbi, for being awesome.

1.0 INTRODUCTION

This dissertation consists of two parts of work: 1) targeted destruction of cancer cells by glucose oxidase-iron oxide bioconjugates, and 2) multistage separation of cells using hydrophobic interactions enabled by temperature responsive polymers. Both projects utilized iron oxide (Fe_3O_4) magnetic nanoparticles for their adjustable physiochemical properties and proven biocompatibility.

Fe_3O_4 magnetic nanoparticles are a promising candidate in varieties of biomedical applications such as drug delivery, cell sorting, magnetic resonance imaging (MRI) and catalysis. It is highly desirable to have the particles with controllable sizes so that they are comparable with different biological entities of interest.

Superparamagnetic iron oxide nanoparticles (SPION) with sizes under 50 nm possess the same intrinsic peroxidase-like activity as Horseradish peroxidase (HRP). This property is widely used in wastewater treatment and detection tools. SPION generate reactive oxygen species (ROS, which play an important role in cell signaling) from H_2O_2 via Fenton's reaction. A significant oxidative stress from ROS can overwhelm the relatively low antioxidant capacity and disrupt the redox homeostasis of cancer cells, leading to selective tumor cell toxicity and destruction. Therefore, we developed a novel approach for ROS-induced targeted cell destruction with SPION-GOx bioconjugates. GOx stands for glucose oxidase, which is an enzyme that

catalyzes the oxidation of glucose to produce H_2O_2. Along with the enhanced permeability and retention (EPR) effect that enables SPION to accumulate passively in tumor, the synergetic effect of SPION-GOx provides a great opportunity to significantly reduce the side effects from the conventional ROS based chemotherapy and radiotherapy on normal tissues. This work is a novel cancer therapy strategy as a substitute or supplement treatment method of radiotherapy and photodynamic therapy (PDT).

Additionally, magnetic activated cell sorting (MACS) has become a common technique for the separation of target cell populations from biological suspensions. A major obstacle preventing MACS from achieving satisfying separation efficiency is the non-specific interactions between the cells and MNP. Thus, we designed a multistage separation scheme by introducing multiple capture-and-release cycles to the separation process. By attaching pNIPAM to both MNP and target cells, we are able to manipulate the reversible hydrophobic-hydrophilic interactions between the functionalized MNP and target cells. This multistage separation approach is a promising MACS strategy in clinical prognosis and environment engineering, for example, detecting the rare circulating tumor cells (CTCs) from large volume blood samples and wastewater treatment.

The following topics are discussed in this dissertation: synthesis, stabilization, unique properties, and applications of Fe_3O_4 magnetic nanoparticles; cancer treatment by reactive oxygen species (ROS); cancer prognosis by isolation and analysis circulating tumor cells (CTCs), targeted destruction of cancer cells by glucose oxidase-iron oxide bioconjugates and multistage separation of cells using hydrophobic interactions enabled by temperature responsive polymers.

1.1 IRON OXIDE MAGNETIC NANOPARTICLES: SYNTHESIS, STABILIZATION, PROPERTIES AND APPLICATIONS

The research on nanoparticles has been growing so explosively in recent years that researchers are able to fabricate, characterize and functionalize particles for specific clinical purposes in a variety of biomedical applications including drug delivery, hyperthermia, MRI agent, separation and sorting biological organisms. Among several types of inorganic particles that have been investigated, the iron oxide (mostly Fe_2O_3 and Fe_3O_4) magnetic particle is a very promising candidate for its adjustable physical and chemical properties and proven biocompatibility. This provides great opportunity in site-specific drug delivery, hyperthermia treatment for malignant cells, magnetic resonance imaging contrast, cell labeling, targeting and as a tool for cell-biology research to separate and purify cell populations[1].

A major advantage of nanoparticles over bulk materials is the large surface area resulting in an improved reactivity[2]. It is necessary that the size and shape of the particles are controllable to be comparable with different biological entities of interest. In order to meet the requirements for different situations, particles with diameters ranging from a few nanometers to hundreds of nanometers can be synthesized through several approaches, including physical methods such as gas phase deposition, electron beam lithography, and wet chemical routes like co-precipitation of Fe^{2+} and Fe^{3+} aqueous salt solutions by adding a base. In the meantime, the magnetic nanoparticles are usually required to be well dispersed in suitable solvents, especially aqueous solution for biomedical applications since agglomeration and/or precipitation may prevent nanoparticles from being delivered to a specific area[3]. Therefore, surface coating that stabilizes the magnetic particles is an important step after synthesis. In this dissertation, two

types of iron oxide nanoparticles were synthesized using two different approaches: superparamagnetic iron oxide nanoparticles (SPION) were prepared using thermal precipitation and were conjugated with glucose oxidase (GOx) for targeted destruction of cancer cells; poly(N-isopropylacrylamide) (pNIPAM) coated PAA-MNP via hydrothermal method for multistage cell separation. Some popular synthesis and stabilization methods are reviewed and compared in this section as well as special features of iron oxide nanoparticles and their biomedical applications.

1.1.1 Synthesis

During the past decades, synthesis methods for stable and monodisperse magnetic nanoparticles have been well studied. Co-precipitation, thermal decomposition, hydrothermal synthesis, and microemulsion are popular approaches for the synthesis of high-quality nanoparticles.

Co-precipitation is a convenient way to synthesize iron oxides (Fe_2O_3 and Fe_3O_4) at temperature ranging from 20-90°C[1]. By adding a base to $Fe^{2+/}Fe^{3+}$ salt solution, magnetic nanoparticles can be prepared once the conditions are fixed, which include the type of salts used, Fe^{2+}/Fe^{3+} ratio, reaction temperature, pH, and the ionic strength of the media. Particles synthesized by co-precipitation tend to have a wide size distribution, which is non-ideal for many applications. The well-known nucleation and growth theory indicates that the key to produce monodisperse nanoparticles from solution is the fast nucleation and the following slow controlled growth. Oleic acid is considered the best candidate as a surfactant to passivate the particle surface and produce uniform products in extensive studies on the effect of several organic ions, such as carboxylate and hydroxyl carboxylate ions, on stabilizing the magnetite,

because spectroscopic characterizations showed that oleic acid ligand undergoes a structural change during γ-Fe_2O_3 nanocrystal synthesis[4]. The mechanism can be explained as the chelation of organic ions with metal ions reduces the number of nuclei, which leads to the particle growth step becoming dominant; in addition, the additives adhering to the nuclei and growing crystals may prevent the growth of particles, which favors the formation of small units [1].

Water-in-oil microemulsion (reverse micelles) can also be used as nanoreactor for the synthesis of magnetic nanoparticles. A microemulsion is thermodynamically stable dispersion with aqueous phase dispersed as microdroplets surrounded by a monolayer of surfactants in the continuous hydrocarbon phase. The resulting particles can be precipitated from the microemulsion by addition of acetone or ethanol, and subsequently extracted by centrifugal. Woo et al. reported Fe_2O_3 nanorods had been synthesized using the microemulsion method via a sol-gel-mediated route. The reverse micelles were formed from oleic acid and benzyl ether, with $FeCl_3$•$6H_2O$ as the iron source and propylene oxide as the proton scavenger[5]. The limitations of the microemulsion technique are that the particle shape (e.g., spheroids or tubes) and size may vary over a wide range. Moreover, it is not an efficient process and usually gives a low yield compared to other methods[1].

In this study, according to the specific size and property requirements we set for the nanoparticles, thermal decomposition and hydrothermal synthesis were used to prepare the two types of iron oxide nanoparticles for targeted cancer cell destruction and magnetic assisted cell separation, respectively. Thus, a detailed discussion of these two synthesis methods, including reaction condition, mechanism and limitations, is given in the following section.

1.1.1.1 Thermal decomposition

In order to produce highly uniform and small nanoparticles that can be used for cancer therapy study on animal models, the thermal decomposition method was taken to synthesize the ultra-small superparamagnetic nanoparticles (SPION). Thermal decomposition of organometallic compounds in high boiling point solvent in the presence of stabilizing surfactants can yield monodisperse magnetic nanoparticles with very narrow size distribution. In this system, iron acetylacetonate, Fe(acac)3, is the organometallic precursor and oleic acid is used as the surfactant. Iron in Fe(III) oxides could be replaced by other metals such as Mn, Co, Ni, Cr[6]; fatty acids and hexadecylamine are alternative surfactants. The size and morphology are determined mainly by the ratios of the reagents (organometallic compounds, surfactant, and solvent), but also affected by reaction temperature, reaction time, and in some cases, the aging period[7]. Examples showing the effects of these decisive factors will be given below.

Peng et al. reported a general and reproducible strategy using generic chemicals for controlling the size, shape, and the size distribution of magnetic oxide nanocrystals[8, 9]. Nearly monodisperse dot-shaped (as compared to tube- and wire-shaped) Fe_3O_4 nanocrystals were synthesized in the size range between about 6 and 50 nm, as shown in Figure 1. The method is based on the pyrolysis of metal fatty acid salts in nonaqueous solutions, which uses either octadecene (ODE), n-eicosane, tetracosane, or a mixture of ODE and tetracosane as the noncoordinating solvents. The corresponding free fatty acids were added into the system to tune the activity of the metal fatty acid salts. The size control of the Fe_3O_4 nanoparticles was realized by varying the concentration and/or the chain length of the fatty acids when the monomer concentration was fixed. In simple terms, the higher the ligand concentration is, the larger the size of the nanocrystals will be. This is because the ligand concentration greatly affects the

monomer reactivity in noncoordinating solvents, while the tunable reactivity of the monomers enables a balanced nucleation and growth which is the key to the control of size and size distribution[10]. The size remains at a fixed value when relatively long chain fatty acids like oleic acid or steric acid were used. However, an increase in particle size was observed, along with the acceleration in the overall reaction rate, when the chain was shortened in fatty acids. The researchers found that by adding activating reagents, primary amines or alcohols, the formation of nanocrystals was significantly accelerated. This is consistent with the increased reactivity coefficient of the precursors. Peng also stated that maintaining a balance between the nucleation and growth stages to prepare fine nanoparticles is better achieved by introducing noncoordinating solvent[8]. In noncoordinating solvents, the reactivity of precursors can be tuned by varying the bonding strength of the ligands to the monomers, concentration, chain length, and/or configuration of the ligands for the monomers.

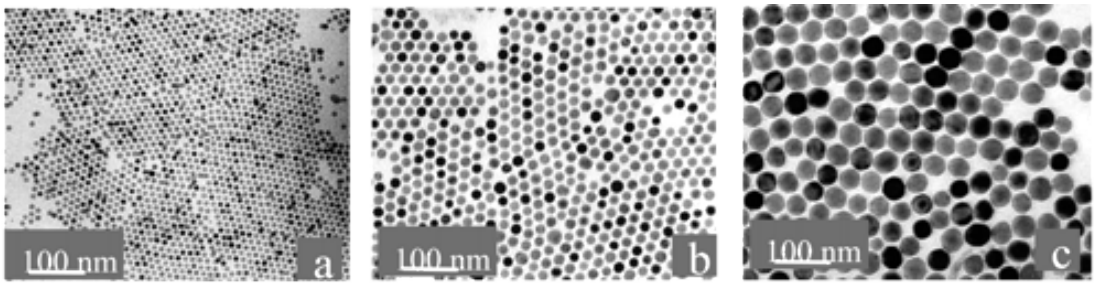

Figure 1. TEM images of as-prepared dot-shaped Fe_3O_4 nanocrystals. Reprinted (adapted) with permission from [8]. Copyright (2004) American Chemical Society.

Sun et al. reported a convenient organic phase process to make Fe_3O_4 particles with very narrow size distribution (i.e., standard deviation < 0.10) and diameter tunable from 3 to 20 nm [11, 12], as shown in Figure 2. Under high-temperature (265°C), the reaction of iron (III)

acetylacetonate, $Fe(acac)_3$, in phenyl ether in the presence of alcohol, oleic acid, and oleylamine can be used to make monodisperse magnetite nanoparticles. It was found that 1,2-hydrocarbon diols, such as 1,2-hexadecanediol, react well with the precursor, and both oleic acid and oleylamine are necessary for the formation of Fe_3O_4 particles. Larger particles can be made via seed-mediated growth starting with as-synthesized small nanoparticles as seeds[13]. Sun indicated that the key to successfully prepare monodisperse nanoparticles is to heat the reaction mixture at 200°C before starting reflux in phenyl ether at 265°C, which indicates that under this reaction condition, the nucleation and growth of nuclei processes are not fast as demonstrated above[12].

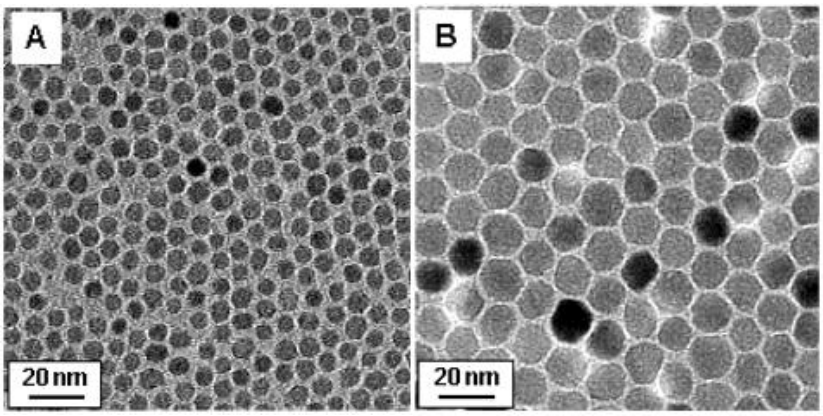

Figure 2. TEM bright field images of (A) 6 nm and (B) 12 nm Fe_3O_4 nanoparticles. Reprinted (adapted) with permission from [9]. Copyright (2004) American Chemical Society.

Particles as prepared, precipitated and dispersed in organic phase are sterically stabilized by the fatty acid and surfactants. The functionalization methods to convert hydrophobic nanoparticles to hydrophilic ones will be discussed in the following chapter.

After reviewing various approaches for monodisperse nanoparticle synthesis, this high temperature organic phase procedure that Sun et al[12] reported was utilized in our cancer cell destruction project to prepare the ultra-small nanoparticles (SPION) due to its low cost and high yields, in addition to the advantage of size-tunable technique.

1.1.1.2 Hydrothermal synthesis

Even though the synthesis strategies discussed in thermal decomposition can produce nearly monodisperse nanoparticles as the most desired feature, the conditions including the preheating step, relatively high reaction temperature (for example, 265°C in Sun's procedure[12]), and inert atmosphere are not very convenient. Alternatively, hydrothermal synthesis, which includes various reactants in a sealed container at high vapor pressure (generally in the range from 0.3 to 4 MPa) and high temperature (generally from 130 to 250 °C), is more convenient. It is prone to obtain the highly crystalline iron oxide nanoparticles since grains formed in hydrothermal synthesis have a higher crystallinity[14]. Instead of using organic compound as solvent, hydrothermal synthesis is usually in a water-ethanol aqueous solution.

Li et al. developed a general procedure to synthesize monodisperse ferrite microspheres, which produces particles with diameters of about 200–800 nm using hydrothermal reduction[15]. The system consists of $FeCl_3$, ethylene glycol, sodium acetate, and polyethylene glycol. The mixture was first stirred to form a clear solution, then sealed in Teflon-lined-stainless-steel autoclave and heated at 200°C for various periods of time. With constant precursor concentration and temperature, the diameter of the microsphere was observed to be increasing from 200 nm (at 8 h) to 800 nm (at 72 h). The components of reaction mixture in this system were skillfully designed: ethylene glycol, as part of the family of polyol, is the reducing agent with high boiling

point; sodium acetate salt can prevent particle agglomeration by electrostatic stabilization; last but not least, polyethylene glycol works as the surfactant also inhibiting agglomeration. Interestingly, Li claimed that[15], in their system, NaOAc seemed to assist in the ethylene glycol mediated reduction of $FeCl_3$ to Fe_3O_4, as it showed that Fe^{3+} could not be reduced solely by ethylene glycol under the same reaction conditions in the control experiment. The magnetic particles prepared from Li's synthetic strategy could remain in suspension for more than 1 day after being suspended in doubly distilled water by sonication, which demonstrates a great systematic colloid stability.

This study conducted by Li's group showed that the microsphere size is controllable with diameters ranging from 200 to 800 nm using the hydrothermal synthetic strategy. These microspheres are colloidal stable and very hydrophilic, which made them good candidates for clinical diagnosis and in the transport of drugs, proteins after proper surface modification. The raw materials used in this synthesis method are inexpensive and the yields are ~92 %, which is relatively high. Therefore, these microspheres can be of great use in biomolecular separations, targeted drug delivery, cancer diagnosis and treatment, as well as MRI[15].

As for the cell separation project, we modified Li Group's strategy[15] by adding polyacrylic acid (PAA) as to meet our need for the subsequent modification with poly(N-isopropylacrylamide) (pNIPAM) on particle surface, since the carboxyl groups from PAA are able to react with the amine groups on the temperature-responsive polymer, pNIPAM terminated by $–NH_2$. Therefore, PAA acted both as a ligand and a surface functionalization agent in this solvothermal reaction system. Details of the synthesis, characterization, and the subsequent modification and application in multistage cell separation of the PAA-MNP will be described and discussed in chapter 3.0.

1.1.2 Stabilization

Maintaining the stability of particles from precipitation and oxidation from air is important after successful synthesis[1]. Therefore, protection to obtain physically and chemically stable colloidal system is crucial for any application of magnetic nanoparticles. At the same time, functionalization of particles for further conjugation with linkers or biomolecules can also be achieved through selected coating processes. Basically, all the coating strategies are to form a core-shell structure. The coating layer, i.e. the shell, protects the naked core (magnetic particle) from the environment where oxidation of Fe^{2+} and acid erosion could occur and induce damage to both particles and the colloidal system. Current coating strategies roughly fall into two major categories: organic coatings from surfactants/polymeric stabilizer, such as dextran[16], poly(ethylene glycol) (PEG)[17], etc.; inorganic shells from silica[18], carbon[19] or precious metals like Ag[20], Au[21].

Polymeric materials used as stabilizers act like a barrier between particles by absorption onto particle surface to provide steric repulsion. An amphiphilic copolymer, which bears a hydrophilic segment to spread into aqueous phase and a hydrophobic segment to anchor on the particle surface, provides the most efficient repulsion. If a polymer chain is charged, the additional electrostatic repulsion will further stabilize the particles[22]. A few characteristics of polymer stabilizer should be taken into consideration when the coating for MNPs is designed. For example, the chemical structure determines the biodegradability and hydrophilic/hydrophobic property; the conformation contributes to the overall size of the colloid, which plays an important role in minimizing the rapid blood clearance; the geometric arrangement and degree of surface coverage; the attachment mechanism (covalent or ionic

binding, hydrophobic interaction), etc. Researchers found that hydrophilic polymeric coatings may increase the plasma half-life resulting from the stealth properties of the shell[23, 24]. PEG is the most widely used hydrophilic polymer that is non-toxic and has great steric repulsive properties[25, 26]. PEG chain can be attached to MNPs by various approaches, such as polymerization at the particle surface[27], modification via sol-gel[28], and silane grafting[29]. Polysaccharide dextran has also been used on MNPs coating for in vivo imaging purpose[30]. Silica may also facilitate the stability and functional design by introducing alkoxysilanes (for example, 3-aminopropyltriethoxysilane)[31]. The advantage of SiO_2 coating is that it is easy to synthesize and its great stability in aqueous phase[32].

Alternatively, particles can be dispersed in a dense matrix (like polymer, silica or carbon) to form particle composites, which consist of a polymer matrix or a reservoir system[33, 34]. In this case, the polymeric shells that avoid size growth after nucleation can create repulsive force to balance the magnetic and the van der Waals attractive forces on particles. Surfactants and polymers that are either physically absorbed or chemically tethered to particle surfaces work similarly as the polymeric shell in particle composites to create repulsion to obtain the colloidal stability. Polymeric shell not only provides improved water dispersity and colloidal stability, but also introduces functional groups, such as amine and carboxyl groups to the surface. Relevant research using gelatin[35], poly(acrylic acid) (PAA)[36], poly(D,L-lactide)(PLA)[37, 38], poly(D,L-lactide-*co*-glycolide)(PLGA)[39-41] has been conducted for encapsulation of MNPs. Senna et al found from the XRD diffraction pattern that crystallinity of the particles decreased with increasing poly(vinylalcohol) (PVA) concentration[42], indicating defects in the crystal structure might occur due to the presence of polymer or copolymer during the nucleation and

growth. This may affect the magnetic features of MNPs, so that caution should be exercised for the selection of stabilizers.

Another way of particle stabilization is by encapsulating magnetic particles into liposome, which is a spherical vesicle used for administration of pharmaceutical drugs[43, 44]. Liposomes are mostly phospholipids with at least one lipid bilayer in aqueous solution[45]. A liposome has an aqueous core surrounded by a hydrophobic membrane. As a result, hydrophilic solutes dissolved in the core cannot pass the bilayer. The fact that liposomes can fuse with cell membrane, which is also a bilayer, provides great potential for drug delivery to a specific site, even though this process is not spontaneous[46]. Similar to encapsulation into polymeric shell, surface functionalization can be realized by liposomal methodology without modification of the MNP core, which makes the stabilization process convenient. Joniau et al. studied the adsorption of different phosphatidylglycerols onto MNPs in this liposomal magnetic system (also known as magnetoliposome) [47]. The bilayer configuration of magnetoliposome is formed with a quick absorption of inner monolayer orientated to MNP surface, followed by a much slower assembly of outer layer through interactions with the exposed hydrocarbon chains. The kinetics results showed that 30%-35% of the adsorption occurs within the first minute, which can be attributed to the high binding affinity character of the inner layer adsorption. The adsorption beyond the high-affinity zone was demonstrated to obey the Langmuir expression (shown in Figure 3):

$$\frac{c}{\Gamma_L} = \frac{1}{\Gamma_L^0}\left(c + \frac{1}{K_L}\right)$$

where Γ_L is the molar number of lipid adsorbed per gram of Fe_3O_4 in the Langmuir zone, Γ_L^0 is the number at saturation, c is the phospholipid equilibrium concentration and K_L is the association constant.

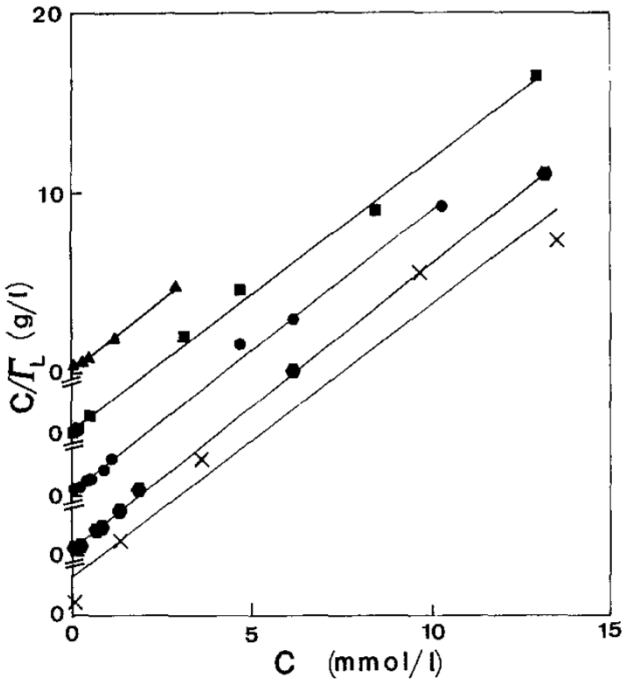

Figure 3. The adsorption of the outer layer on MNP surface beyond the high-affinity zone obeys the Langmuir adsorption isotherms. Reprinted by permission from Springer Nature[47] COPYRIGHT (1988).

Instead of incorporating magnetic particles into the aqueous interior of a vesicles during the preparation, Cuyper et al. developed another approach to adsorb a phospholipid bilayer onto the particle core that were already surfactant-coated[45]. Briefly, phospholipid was vacuum dried from the solvent chloroform and dispersed in TES buffer (4mM, pH 7.0), then sonicated to form small unilamellar vesicles. Afterwards, solid lauric acid was added to stabilize MNPs and

maintained at 90 ºC to improve the solubility of the detergent. Finally, the lauric acid was substituted by phospholipids using dialysis of Fe_3O_4 - lauric acid complex in the presence of vesicles for 3 days at 37 ºC. The author claimed that the encapsulation following this protocol for the preparation of magnetoliposomes could be considered to be 100%, since all the MNPs were found to be covered by a phospholipid bilayer.

1.1.3 Special features and biomedical applications

Controllable size and unique properties make iron oxide magnetic particles ideal candidates in plenty of biomedical applications. Firstly, owing to various and advanced synthesis methodology, the size of iron oxide particles may range from a few nanometers to tens of micrometers, which are comparable to the size of a cell (10 – 100 μm), a bacteria (0.2 – 10 μm), a virus (20 – 450 nm), a protein (5 – 50 nm) or a gene (2 nm wide and 10–100 nm long)[48]. This controllable size allows the particles to easily interact with or bind to almost any biological entity of interest. Moreover, the magnetic property of iron oxide [Fe_3O_4 and γ-Fe_2O_3 (one common form of Fe_2O_3, cubic structure)] allows particles to be manipulated remotely by external magnetic field gradient. By applying external magnetic fields and letting them penetrate into a particular tissue, magnetic nanoparticles, or magnetically tethered biological entities can be used to transport and/or immobilize drug vehicle, such as anticancer drug (doxorubicin)[49], or a cohort of radionuclide atoms to a targeted region of the body[50]. Third, the magnetic nanoparticles can resonantly respond to a time-varying magnetic field transforming electromagnetic energy from the high-frequency field to heat. In this case, particles can be heated up, providing the application opportunity as hyperthermia agents, delivering toxic amounts of

thermal energy to targeted bodies such as tumors; or as chemotherapy and radiotherapy enhancement agents, where a moderate degree of tissue warming results in more effective malignant cell destruction. The applications discussed above are made possible in biomedicine as a result of the special physical properties of magnetic nanoparticles.

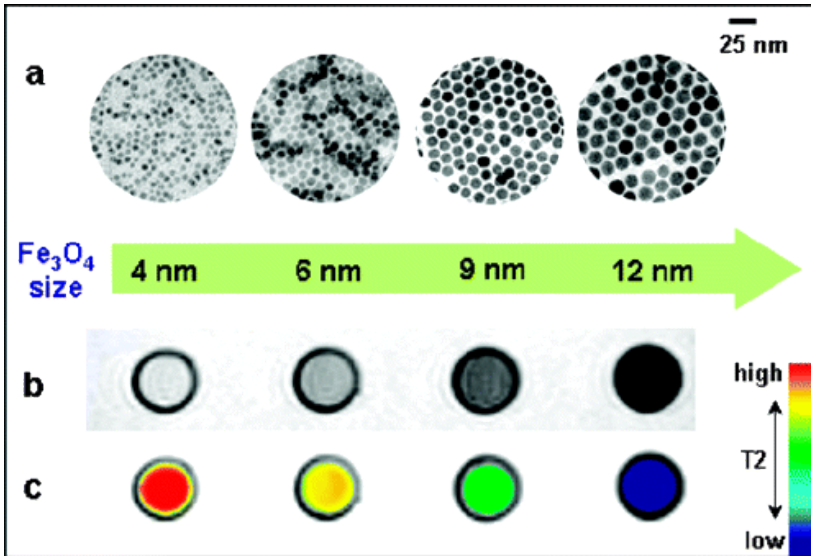

Figure 4. Nanoscale size effect of WSIO nanocrystals on magnetism and induced MR signals. (a) TEM images of Fe_3O_4 nanocrystals of 4 to 6, 9, and 12 nm. (b) Size-dependent T2-weighted MR images of WSIO nanocrystals in aqueous solution at 1.5 T. (c) Size-dependent changes from red to blue in color-coded MR images based on T2 values. Reprinted (adapted) with permission from [51]. Copyright (2005) American Chemical Society.

Cheon et al. investigated the effect of nanoparticle size on MRI signal intensity for their utilization in cancer diagnostics[51]. Highly monodisperse (σ = ~5%) water-soluble iron oxide nanoparticles with sizes of 4, 6, 9, and 12 nm using the thermal decomposition of $Fe(acac)_3$ were first synthesized, and then demonstrated the correlation between the particle size and magnetism by measuring the mass magnetization values. It is shown that as magnetic particle size increases, the *T2*-weighted MR signal intensity continuously decreases[51], as shown in Figure 4.

1.1.3.1 Gene and Drug Delivery

The idea of using magnetic particles to deliver therapeutic agents, such as gene and pharmaceutical agents, was first proposed in the late 1970s by Widder et al.[52]. The basic concept of magnetic drug delivery is to attach the magnetic nanoparticles to the drug, and thus to target at a specific site guided by the localized magnetic field. The drug-loaded magnetic particles can be held at the therapy location until the therapy is complete or the local concentration is high enough, which minimizes the side effects and toxicity in other normal organs and tissues. The therapeutic molecules can be attached to, or encapsulated within a vehicle which may be a core-shell structured magnetic particle with polymer coatings, or may be in the form of porous polymers with magnetic nanoparticles precipitated in the pores[53]. By modifying the polymer coating, drugs for targeted chemotherapy or therapeutic DNA to fix a genetic defect can be attached to magnetic particle carriers. Several approaches have been applied to attach the agents to particle, including conjugating cleavable linkers[54], incorporating therapeutic molecules into degradable shell, or simply taking advantage of electrostatic interactions between the positively charged particle surface and negatively charged backbone of DNA[55].

Even though the targeted drug delivery enabled by magnetic particles has been proven to be successful in many studies[32, 52, 53, 56], only a small number of clinical trials have been performed to date. A trial performed in 2004 examined the efficacy of magnetic targeted carrier bound to doxorubicin (MTC-DOX) for the treatment of four patients with inoperable hepatocellular carcinoma[57]. In this study, doxorubicin was absorbed to composite microparticles made from metallic iron and activated carbon following the Langmuir theory[58]. MTC-DOX was delivered via the hepatic artery using concurrent MR imaging to monitor, and

interim catheter manipulation was performed with fluoroscopic guidance to optimize delivery to the tumor and minimize the effects on normal tissue[57]. The particles were targeted to the tumor sites by using rare earth magnets placed on the body surface. The results indicated that the MTC-DOX microparticles were well targeted at the tumor sites with the tumor volumes shrinking down to 64%–91% of the originals, while the affected normal liver volume only ranged from 7%–30%. Despite of the drawbacks of the long duration of the treatment sessions, the expense of obtaining multiple MR images and the abnormal pain reported by all four patients, this study has provided very important information for future research in magnetic particle facilitated drug delivery.

1.1.3.2 Hyperthermia

Magnetic hyperthermia is an experimental treatment for cancer based on the fact that magnetic nanoparticles can transform electromagnetic energy from an external high-frequency field to heat. Hyperthermia is considered a supplementary treatment since a small temperature rise makes cancer cells more susceptible to radiation and chemotherapy[59]. The biological basis of hyperthermia is that temperature rise (to 40–45°C) initiates a series of subcellular events, rendering the cells susceptible to apoptosis or other forms of damage, leading to subsequent cell death. Because of the low efficiency of blood flow and oxygen transport through newly formed blood vessels within tumors, tumor cells in an acidotic and nutrient-deprived setting tend to be more thermosensitive[60]. Previous studies showed that intravenously injected nanoparticles prefer to accumulate in tumors rather than in normal tissues, which is often referred to as the enhanced permeability and retention (EPR) effect[61]. Therefore, when magnetic particles are exposed to alternating magnetic fields, heat is generated at tumor site from magnetic hysteresis,

Neel-relaxation and Brown-relaxation[62]. Tumor-targeted nanoparticles results in less non-specific accumulation in the other part of body, enabling a lower dosage for an equal therapeutic effect and a decreased toxicity induced by nanoparticles. A monolayer of PEG covering polymeric dextran shell could enhance the circulation half-life[63] to prevent bare iron oxide particles from being cleared from blood too fast and accumulation in liver, spleen and lymph instead of tumor[59]. To achieve adequate concentrations in the tumor, magnetic nanoparticles are modified by targeting molecules like peptides and antibodies. Triton BioSystems, Inc. (Chelmsford, MA) developed the system of alternating magnetic field (AMF) responsive nanoparticles and targeted these to cancerous tissues by conjugating with monoclonal antibodies[59]. The degree of heating is controlled by the AMF field. However, increasing the AMF field strength generates heat in normal tissues from eddy current losses. Therefore, the raised temperature in the normal tissues limits the extent to which the AMF field can be increased[64].

1.1.3.3 Diagnostic: MRI contrast

MRI is one of the most powerful non-invasive imaging modalities utilized in hospitals and clinics for medical diagnostic[65]. The process through which the hydrogen protons return to their original state from the alignment to the applied magnetic field is termed the relaxation. Longitudinal relaxation (T1) and transverse relaxation (T2) are two independent processes, which can be monitored to generate an MR image. Proton density, as well as the nature of the tissues, determines the local variation in relaxation, corresponding to image contrast. MNPs provide MR contrast enhancement when accumulated in tissues[56]. This ability of MNPs to

serve as MR imaging contrast agents provides great detection and diagnostics opportunities in cancer imaging, cardiovascular disease imaging and molecular imaging [30].

Helmberger et al. demonstrated that imaging of liver tumors and metastases through RES-mediated uptake of SPION is able to distinguish lesions as small as 2–3 mm[66]. Moreover, ultrasmall superparamagnetic iron oxide nanoparticles(USPIOs) have been proven effective identifying lymph node metastases with a diameter of 5–10 mm under MRI[67]. Another promising usage of MNPs in cancer therapy is to improve the delineation of brain tumor boundaries and quantify tumor volumes[68]. This is because MNPs improved cellular internalization and were cleared more slowly from tumor site, which prolonged the delineation of tumor margins[69].

1.1.3.4 Magnetic Assisted Separation

Magnetic particles have been proven to be effective and useful in magnetic-driven separation of biochemical products like protein, DNA, and cells[70-73]. It is a reliable and simple method to efficiently capture specific biomolecules from mixtures by applying external magnetic field. The unique superparamagnetic feature that magnetic particles in certain sizes have is of great usage since they can be magnetized from the external magnetic field and resuspended immediately as soon as the magnetic field is removed.

Xu et al. used dopamine (DA) as a novel anchor to immobilize functional molecules, nitrilotriacetic acid (NTA), on the iron oxide shell of magnetic nanoparticle, which exhibits high specificity and capacity for histidine-tagged protein purification from cell lysate[70]. The average sizes of M/Fe_2O_3 synthesized are 8.5 nm and 9.5 nm when the cores of nanoparticle are Co and $SmCo_{5.2}$, respectively. Dopamine was chosen to be the anchor on Fe_2O_3 shell for two

main reasons. Firstly, the bidentate enediol ligands of dopamine can convert coordinatively unsaturated Fe surface sites to a bulk-like lattice structure[74], which may result in high binding affinity of dopamine to Fe_2O_3 shell. Secondly, Langmuir isotherms indicate that the adsorption of dopamine from Fe_2O_3 nanoparticles is more favorable than desorption[75]. After removing the physically absorbed proteins on M/Fe_2O_3-DA-NTA-Ni^{2+} particles by deionized water, 10 and 500 mM of imidazole elutions were used to sequentially wash the protein-bound nanoparticles. It is shown in Figure 5A that only the target protein (6xHis-GFP, lanes 4, 5, and 7) existed in the imidazole elutions. In addition, electrophoresis traces in Figure 5B show that the fractions washed from the particles with $SmCo_{5.}2$ core that had been boiled in Tris buffer (pH = 7.9) for 20 min contain only the histidine-tagged protein, indicating the specificity and efficiency the particles remain unaffected from heating[70].

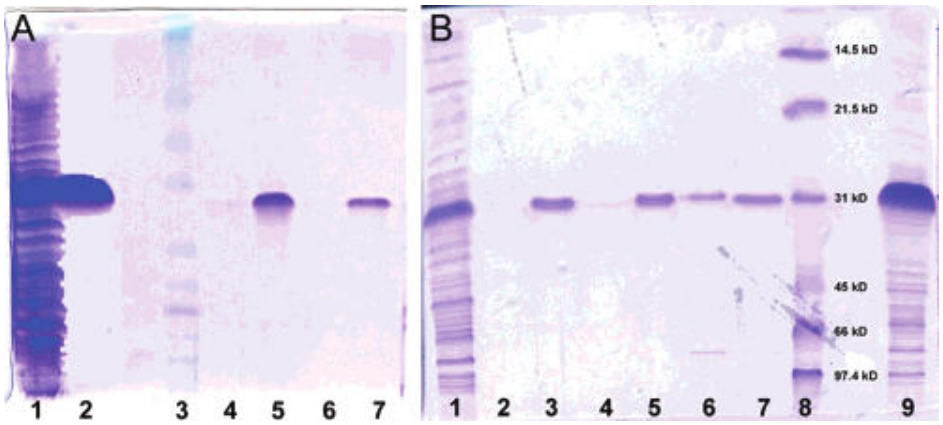

Figure 5. SDS/PAGE analysis of the purity of the proteins. (A) Cell lysate (lane 1), GFP standard (lane 2), molecular weight marker (lane 3), the fractions from freshly made $SmCo_{5.2}/Fe_2O_3$−NTA by washing with imidazole elutions (10 mM, lane 4; 500 mM, lane 5), fractions from the freshly made Co/Fe2O3−NTA using imidazole elutions (10 mM, lane 6; 500 mM, lane 7). (B) Cell lysate (lane 1), GFP standard (lane 7), the molecular weight marker (lane 8), the fractions washed from the freshly made 6b (lanes 2 and 3), boiled 6b (lanes 4 and 5), and the microbeads of the commercial HiTrap affinity column (lanes 6 and 9). The concentrations of imidazole are 10 mM (lanes 2, 4, and 6) and 500 mM (lanes 3, 5, 9). Reprinted (adapted) with permission from [70]. Copyright (2004) American Chemical Society.

Magnetic nanoparticles have also shown great capabilities in gene separation due to their high separation efficiency[71]. Separation of rare DNA/mRNA targets from complex matrix is critical in diagnostics, gene expression studies, and gene profiling. Weihong Tan et al. developed a novel genomagnetic nanocapturer (GMNC) for collection, separation, and detection of trace amounts of DNA/RNA molecules with one single-base difference[72]. The GMNC was coated with silica as the protection layer, where avidin-biotin was used as linkers to conjugate the molecular beacon DNA probes onto the particle surface. After being evaluated in both artificial buffer solution and in cancer cell samples containing different proteins and random DNA sequences, the GMNC was demonstrated to be highly efficient in collection of trace amount of DNA/mRNA samples down to femtomolar (10-15 M) concentrations. This newly developed genomagnetic nanocapturers have exceptional feature of real-time monitoring and product collection as well, which provides plenty of future application opportunities in gene separation.

1.2 CANCER TREATMENT BY REACTIVE OXYGEN SPECIES

Reactive oxygen species (ROS) are a wide range of critical signaling molecules[76, 77]. When the unpaired electron of oxygen reacts with other molecules, the partially reduced highly reactive products formed are defined as ROS. ROS consist of a group of chemicals, including superoxide anion radical, singlet oxygen, hydrogen peroxide and the hydroxyl radical. ROS can be produced from several enzyme systems, including the mitochondrial electron transport chain, cytochrome P450, lipoxygenase, cyclooxygenase, the NADPH oxidase complex, xanthine oxidase, and peroxisomes[78]. Among those systems, mitochondrial oxygen metabolism is the major source

of superoxide resulting from the electron transport chain. The hydroxyl radical, •OH, is the neutral form of the hydroxide ion (OH^-). The high reactivity of hydroxyl radical makes it a very destructive radical with a short half-life of approximately 10^{-9} s[79], which mostly leads to local reactions at the site where it is formed shortly beforehand.

ROS act as a second messenger in cell signaling and essentials for biological processes in normal cells, while they are ironically considered harmful to cells, tissues and organisms meantime[80]. ROS are physiologically produced intracellularly through multiple mechanisms depending on the cell type. The major process, oxidative phosphorylation in which adenosine triphosphate (ATP) is produced, involves the transport of protons via the electron transport chain. Electrons are transferred through proteins via redox reactions, and finally to oxygen molecule. In most cases, the oxygen is fully reduced to water by gaining four electrons; however, oxygen can sometimes be partially reduced to produce the superoxide radical ($•O_2^-$), the hydrogen peroxide (H_2O_2), and hydroxyl radical (•OH) by receiving one, two, three electrons, respectively[81]. ROS can also be generated by exogenous sources like radiation, and pathologically by inflammation of metal such as copper and iron. In human body, iron normally binds to transferrin, which is blood plasma glycoproteins that control the concentration of free iron in the blood[82]. When iron is not bound, it will generate ROS, particularly the most reactive hydroxyl radicals, via Fenton's reactions[83]:

$$Fe^{2+} + H_2O_2 \longrightarrow Fe^{3+} + {\cdot}OH + OH^-$$

$$Fe^{3+} + H_2O_2 \longrightarrow Fe^{2+} + {\cdot}OOH + H^+$$

ROS level is usually maintained very stable by scavenging systems, in which such ROS are involved in cell signaling[84]. Whereas redox balance, the ratio between oxidizing and

reducing species within cells, is achieved by a few enzyme systems that neutralize toxic oxidants like ROS. For example, superoxide dismutases (SOD) can catalyze the reaction of $\bullet O_2^-$ to H_2O_2, and subsequently H_2O_2 is converted to H_2O by gluthathione (GSH) peroxidase coupled with glutathione reductase[85]. A slight increase in ROS level may induce higher cell proliferation and differentiation rates, while a significant ROS stress resulting from the exogenous agents can overwhelm the relatively low antioxidant capacity and disrupt the redox homeostasis inside cancer cells, and cause damage to proteins, lipids and DNA, which can lead to cellular damage and death[86-88], as shown in Figure 6.

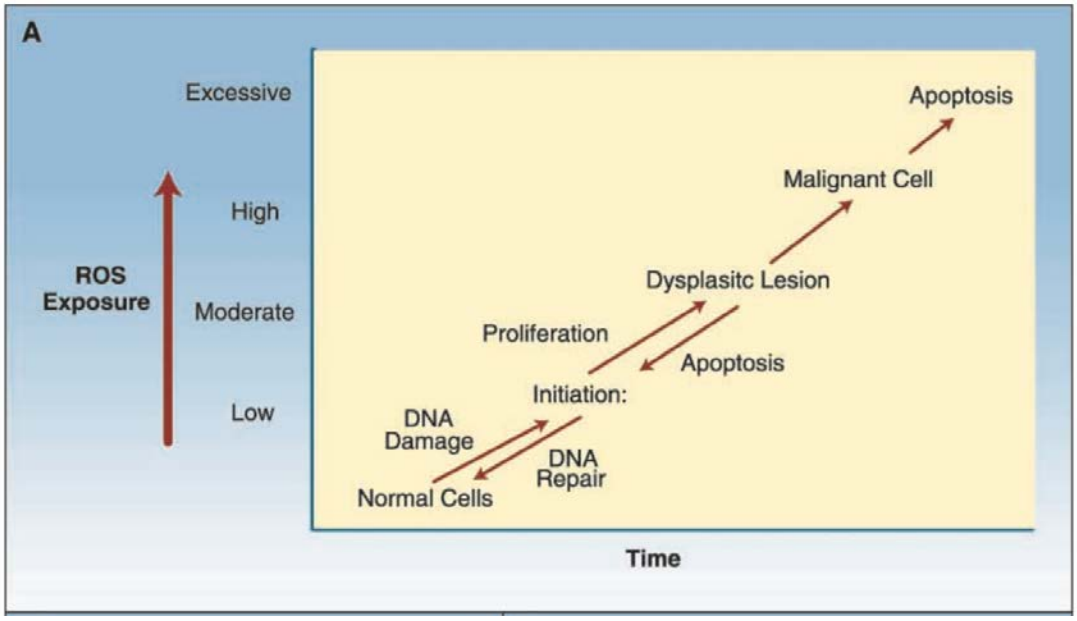

Figure 6. Influence of ROS exposure level on cell sinaling. Reproduced from [85], Copyright 2007 with permission from AACR.

DNA damage mediated by ROS plays an important role in carcinogenesis initiation and malignant transformation[89]. Hydroxyl radicals may react with pyrimidines, purines, and

chromatin protein, causing base modifications, genomic instability, and alterations in gene expression[85]. Chronic inflammation or chronic chemical irritants like tobacco smoking can be some pathologic sources of transforming ROS[90]. Due to the shortage or absence of cell cycle checkpoints, and the overexpress in oncogene growth factors and the receptor tyrosine, transformed cells ultimately end up with tumor formation and chronic hypoxia[91]. Inhibition of protein phosphatases caused by H_2O_2 induces proliferation and apoptosis suppression, and also associates oncogene overexpression with ROS-mediated signaling[92]. Abnormal cell proliferation driven by oncogene growth factor activation and signal transduction requires larger amount of oxygen which is beyond the capacity of the resting vasculature, and therefore stimulates the development of new blood vessels[93].

Among all the reactive oxygen species, the hydroxyl radical is extremely reactive because it is able to propagate a chain reaction by removing electrons from any molecule in its path, and turning that molecule into a free radical, which makes it the most damaging radical. Cancer cells are known for an exhibition of increased intrinsic oxidative stress. Therefore, the high level of ROS in cancer cells has provided opportunity to develop new therapeutic strategy to preferentially kill cancer cells rather than both the cancer cells and the healthy cells in current cancer treatments[94].

There are a few common approaches to generate ROS in current clinical research, including radiotherapy, photodynamic therapy and chemotherapy. During radiotherapy, there is a massive boost in ROS level initiated by X-rays, γ-rays, or heavy particle radiation such as protons and neutrons. However, concerns about the healthy tissue damage and radiation safety have been restricting the application of radiation therapy to a very large extent[95-98]. Whereas photodynamic therapy (PDT) uses ROS generated by irradiating nontoxic photosensitizer with

appropriate light in the presence of molecular oxygen to destroy tumor cells[99-101]. Even though the principle is simple, it is difficult and challenging to control the dose of drug and light, as well as the interval between drug and light administration[99, 102-104]. Moreover, PDT is limited by the penetration depth of the light that excites the photosensitizers.

Recently, a few studies utilized SPION in combination with ROS-based anticancer drugs to potentially improve drug targeting specificity and therapeutic efficacy in theranostic nanomedicine platforms for multimodal cancer image-guided cancer therapy[105, 106].

As described above, increased ROS level leads to enhanced cell proliferation and apoptosis suppression, therefore modulation of ROS to a certain level can be used as a therapeutic strategy in cancer therapy. The pathways in which ROS are increased in malignant cells are oncogene signaling via the NADPH oxidase complex and by hypoxia-related mitochondrial ROS. Therefore, two therapeutic approaches targeting the pathways are considered: (a) increasing ROS scavenging, thereby reducing H_2O_2 signaling and restraining tumor growth; (b) interfering with ROS scavenging within cells, causing excess ROS accumulation therefore triggering apoptosis[107, 108].

Cullen et al.[109] showed evidence to support that increasing ROS scavenging could be a promising therapeutic strategy using ROS. They investigated if the overexpression of phospholipid glutathione peroxidase (PhGPx), which decreases lipid hydroperoxides from biomembranes, could change pancreatic tumor cell behavior. Both mitochondrial PhGPx form (L-form) and nonmitochondrial PhGPx form (S-form) were used in the synthesis of adenovirus–PhGPx (L/S-form) construct. In the nude mice with pancreatic cancer cells implantation model, AdPhGPx-L- form decreased in vivo tumor growth to a greater extent than did AdPhGPx-S-form. Meanwhile, AdPhGPx-S-form demonstrated 80% tumor growth inhibition *in vitro*,

whereas AdPhGPx-L-form demonstrated 95% tumor growth inhibition. This growth-inhibitory effect showed that overexpression of glutathione peroxidase could depress tumor growth both in vitro and in vivo in mouse models.

On the other hand, interference with ROS removal can also result in the accumulation of excess ROS, which leads to apoptosis by triggering mitochondrial to open permeability transition pore and release pro-apoptotic factors[110]. ROS are one of the most efficient activators of the PTP for apoptosis[111]. When ROS are generated, Ca^{2+}, a potent stimulus for the PTP, is released from both intracellular stores and the extracellular environment [112], which put tumor cells under oxidative stress as well as a greater risk from the cytosolic calcium. Chandra et al stated that tumor cells which are resistant to chemotherapy drugs can isolate Ca^{2+} more efficiently[113]. The tumor cells also show a reduction in the release of Ca^{2+} from intracellular storage sites once apoptosis is inducted. Thus, these tumor cells are less sensitive to the stimulation caused by Ca^{2+}.

A platform that enables singlet oxygen ($^1O_2$) generation at specific tumor site for cancer cell destruction has been developed by Chen et al.[106] to show evidence of feasibility of ROS used as therapeutic agents in cancer treatment. The system was based on a reaction similar to Fenton reaction discussed above between linoleic acid hydroperoxide (LAHP) attached to iron oxide nanoparticles and the ferrous ions released from the particles under acidic condition. This system has been shown to lead to apoptosis of U87MG cell line both in vitro and in vivo through $^1O_2$ generation at tumor site and ROS mediated mechanism. This study[106] provided important evidence that moderating ROS level by introducing external ROS source can be a feasible approach for tumor specific cancer treatment.

1.3 CANCER PROGNOSIS BY ISOLATION AND ANALYSIS CIRCULATING TUMOR CELLS (CTC)

Despite of the advanced techniques in surgery, metastasis is still one of the most critical problems that affect the prognosis of cancer patients[114]. During metastasis, tumor cells are detached from the original site and shed into the bloodstream, then arrested in the small vessels. These so called circulating tumor cells (CTCs) can finally grow into secondary tumors after they successfully survived from the host defense mechanisms and establish a microenvironment. In other words, CTCs are the seeds for subsequent growth of additional tumors in fairly distant organs, resulting in the majority of cancer-related deaths.

It is clinically important to find out a way detecting a small quantity of CTCs in the relatively large amount blood sample. In previous studies, disseminated tumor cells in peripheral and mesenteric venous blood were detected by conventional cytology or immunocytological methods using monoclonal antibodies (mAbs) to cytokeratin (CK) or epithelial cell membrane markers[115-117]. However, these staining methods are too complicated for routine use, and the sensitivity was limited by the low analysis capacity. Developments in molecular technology have made it possible to detect small numbers of tumor cells in the peripheral blood, and several reports have described the usefulness[42, 47].

In addition to capturing CTCs from blood, cell separation processes also have broad application in isolation of immune cells from peripheral blood, isolation of white blood cells from tissue, and food industry such as separation of pathogenic bacteria from food. Three different cell separation approaches, which are classified based on if the cell type of interest is targeted and retained for subsequent analysis, include positive selection, depletion, and negative

selection[118]. With positive selection, the cell of interest is targeted by the removal mechanism and retained for downstream analysis. This typically is enabled by targeting a cell surface marker like receptor or antigen with a monoclonal antibody or peptide[119]. Alternatively, depletion is to remove a single cell type from a biological mixture. For example, removal of red blood cells (RBCs) from peripheral blood mononuclear cells (PBMCs)[120]. Similar to depletion, when several cell types are removed to leave only one cell type remained, it is called negative selection, for instance, depletion of all cells except for T-Cells, or removal of all cells except for B-Cells, from samples like whole blood or bone marrow[121]. Currently, various cell separation technologies have been studied and developed commercially, including fluorescence activated cell sorting (FACS), magnetic activated cell sorting (MACS), buoyancy activated cell sorting (BACS) and other technologies, such as microfluidics, centrifugation, and filtration.

The general idea of fluorescence activated cell sorting (FACS) is based on cell labeling with fluorescent markers, either internal or external markers of the cells. The cells are then measured and identified one at a time and then sorted based on the fluorescence signal generated from the marker using flow cytometry. Flow cytometry is a very informative and powerful method for the analysis and separation of cell populations. Its strength is to measure multiple parameters quantitatively from statistically adequate numbers of cells to define the properties of a cell population or its component subpopulations[122]. FACS can be widely utilized for cell separation thanks to the monoclonal antibodies, which have greatly increased the range and effectiveness of immunofluorescence measurements. Herzenberg et al.[123] reported in the 1960s that they used intracellular fluorescence, which was developed from fluorochromasia after exposure to fluorescein diacetate, as the sorting parameter for separation of cultured Chinese hamster ovarian (CHO) tumor cells from mouse spleen cells. The intracellular fluorescence in

CHO was realized by incubating the CHO live cells with fluorescein diacetate, which can enter the cells and be hydrolyzed by intracellular esterases. Since the fluorescein generated cannot exit the cell membrane, the CHO cells are able to show fluorescent signal when illuminated by the appropriate exciting beam, thus can be detected and analyzed in the flow cytometry. The method was also used to sort highly fluorescent fractions with similar procedure from mouse spleen cells immunized to sheep erythrocytes. The enrichment factor in antibody-producing cells reached 4 - 10.

FACS facilitated with flow cytometry is overall a rapid and simple procedure to sort and analyze cell populations. Appropriate combinations of fluorescence labeling and exciting wavelengths allow us to evaluate multiple parameters on each cell, and therefore to distinguish between cell types in mixed cell populations, or to assess the relationships between each cellular variable[124]. Taken the requirement to avoid coincidence counting and mechanical damage to the cells into consideration, the factors of the cell concentrations in the sample and linear flow rates usually yield that mostly 100 to 1,000 cells s^{-1} are analyzed by the instrument, which renders FACS a very high-speed analysis technology. The requirement of single cell suspensions for flow cytometry may pose certain limitations on its applicability, in addition to a substantial cost on the instrument[125].

Another widely used cell separation method is magnetic activated cell sorting (MACS), which is a gentle, fast and promising method for isolating and detecting a small amount of tumor cells that are functionally active from the blood circulation by magnetic labeling (shown in Figure 7)[126]. The technology is based on magnetic particles, in combination with an external magnetic field, a column or magnetic separator or simply a magnet. When a strong enough magnetic field is applied, the magnetically labeled cells (target cells) retain in the column, while

unlabeled cells pass through, which can be collected as the unlabeled fraction, which are non-target cells. The retained cells are eluted to form a new solution after removal from the magnet.

Typically, MNPs are functionalized with a receptor to bind the molecules on the surface of the specific cell, and high separation efficiency is enabled by the extremely high binding affinity and specificity of the receptor, such as an antibody, immobilized on the MNPs. However, a major obstacle that prevents the MACS technology from achieving satisfying separation efficiencies is the non-specific interactions between the cells and MNPs. Despite that the binding affinity of antibodies to the antigens is orders of magnitude greater than that of the nonspecific binding, the effect of nonspecific interactions becomes significant and eventually becomes a major challenge in the case of separation processes that require very large enrichment factors.

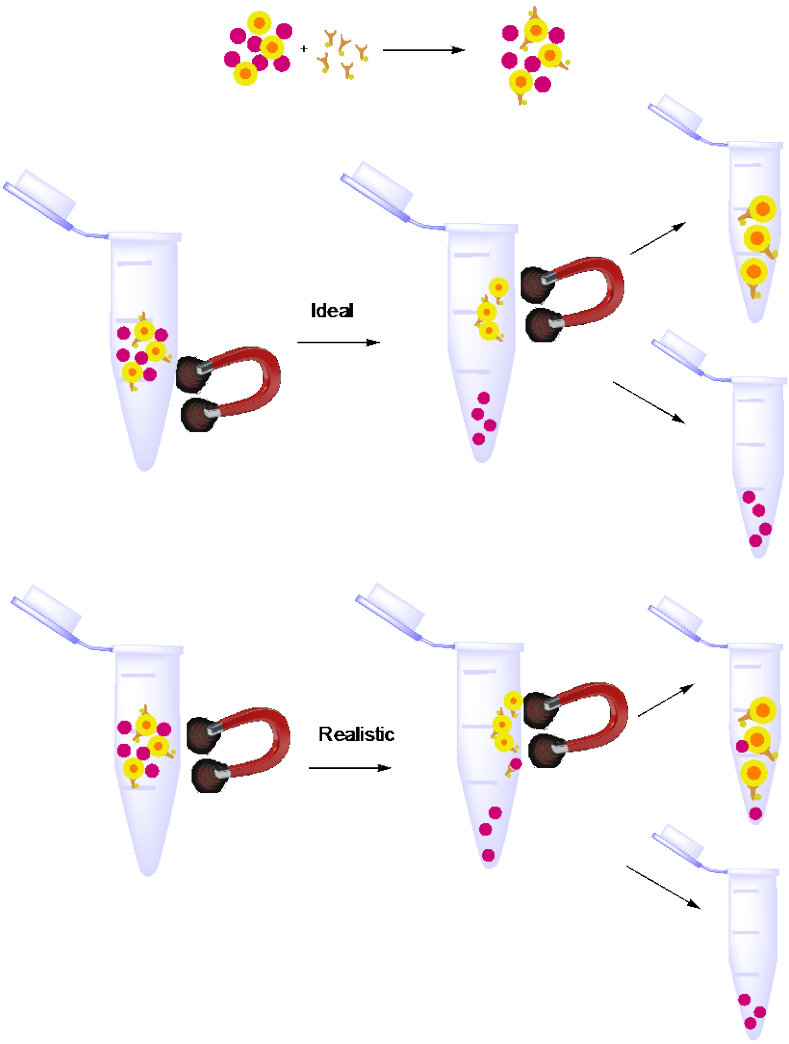

Figure 7. MACS separation scheme: ideal vs. realistic.

2.0 TARGETED DESTRUCTION OF CANCER CELLS BY GLUCOSE OXIDASE-IRON OXIDE BIOCONJUGATES

In this chapter, a platform was designed for ROS induced cancer cell destruction based on the fact that a significant increase in ROS level could lead to cell apoptosis and death. The ROS in this platform is generated via Fenton's reaction between Fe^{2+}/ Fe^{3+} provided by the iron oxide nanoparticles and H_2O_2 produced from glucose. Glucose oxidase and iron oxide were conjugated by click chemistry method to form SPION-GOx bioconjugates, which were able to passively accumulate in the tumor due to the EPR effect induced by nanoparticles.

The feasibility of the platform designed above has been demonstrated:

1) Both FPLC and DLS results showed that the SPION-TCO and GOx-Tz were successfully conjugated based on the increase in particle size;
2) TMB assay indicated that SPION-GOx bioconjugates generate ROS effectively from the substrate glucose;
3) *In vitro* cell viability assay showed that SPION-GOx bioconjugates efficiently destruct tumor cells;
4) *In vivo* cytotoxicity assessment indicated that SPION-GOx possess a low toxicity and side effect.

2.1 INTRODUCTION

Ultra-small superparamagnetic iron oxide nanoparticles (SPION) are a multi-duty platform with the particle diameter <50 nm. Small size enables cellular uptake, extravasation, and tissue localization in drug delivery. Smaller particles accumulate in pathological tissues with leaky vasculature via the enhanced permeability and retention (EPR) effect[127]. In addition, small size results in enhanced accumulation in target organs by minimizing nonspecific clearance in reticuloendothelial system tissues like liver and spleen[128].Furthermore, the mechanism of cellular uptake and subsequent intracellular routing is also affected by size, with smaller particles being internalized via clathrin-coated pits and more likely to reach lysosomes[129]. As a result, small particles reach cellular targets more efficiently, but require a mechanism to escape lysosomal degradation. While there are benefits of using small nanoparticles, there is also a need to give them complex function, so they can overcome obstacles presented by their small size. Despite of the fact that SPION have not shown toxicities after cell uptake and cellular internalization so far, the biological activities of them have hardly been developed for therapeutic applications. SPION are generally considered MRI contrast agents or drug delivery vehicles with no intended pharmacological functions. The possibility to modify the surface of the particles with biologically active compounds, like antibodies and peptides, enables transport of therapeutic agents into specific tumor cells, increasing specificity and avoiding the access of cytotoxic agents to healthy tissues during the delivery process.

Recently, a few studies utilized SPION in combination with ROS-based anticancer drugs to potentially improve drug targeting specificity and therapeutic efficacy in theranostic nanomedicine platforms for multimodal cancer image-guided cancer therapy[105, 106]. ROS are

a group of chemical species (including superoxide anion radical, singlet oxygen, hydrogen peroxide and the hydroxyl radical) that act as a second messenger in cell signaling and essentials for biological processes in normal cells, while they are ironically considered harmful to cells, tissues and organisms meantime[80]. ROS are physiologically produced intracellularly through multiple mechanisms depending on the cell types. The major process being the one called oxidative phosphorylation in which adenosine triphosphate (ATP) is produced, involves the transport of protons via the electron transport chain. Electrons are transferred through proteins via redox reactions, and finally to oxygen molecule. In most cases, the oxygen is fully reduced to water by gaining four electrons; however, oxygen can sometimes be partially reduced to produce the superoxide radical ($\bullet O_2^-$), the hydrogen peroxide (H_2O_2), and hydroxyl radical ($\bullet OH$) by receiving one, two, three electrons, respectively[81]. ROS can also be generated by exogenous sources like radiation, and pathologically by inflammation or metal such as copper and iron. In human body, iron normally bind to transferrin, which is blood plasma glycoproteins that control the concentration of free iron in the blood[82]. When iron is not bound, it will generate ROS, particularly the most reactive hydroxyl radicals, via Fenton's reactions[83]:

$$Fe^{2+} + H_2O_2 \longrightarrow Fe^{3+} + \cdot OH + OH^-$$

$$Fe^{3+} + H_2O_2 \longrightarrow Fe^{2+} + \cdot OOH + H^+$$

A slight increase in ROS level may induce higher cell proliferation and differentiation rates, while a significant ROS stress resulting from the exogenous agents can overwhelm the relatively low antioxidant capacity and disrupt the redox homeostasis inside cancer cells, and cause damage to proteins, lipids and DNA, which can lead to cellular damage and death[86-88].

Among all the reactive oxygen species, the hydroxyl radical is extremely reactive because it is able to propagate a chain reaction by removing electrons from any molecule in its path, and turning that molecule into a free radical, which makes it the most damaging radical. Cancer cells are known for an exhibition of increased intrinsic oxidative stress. Therefore, the high level of ROS in cancer cells has led us to develop new therapeutic strategy to preferentially kill cancer cells rather than kill the healthy cells simultaneously in current cancer treatments[94].

To avoid the healthy tissue damage, radiation safety issue caused by radiation therapy, and difficulties in controlling PDT light administration, in the past decades, some therapeutic drugs that either generate ROS or inhibit antioxidant enzymes have been investigated for cancer treatment [30-32]. Here we propose a new approach for ROS-induced cell destruction through passive accumulation of SPION-GOx bioconjugates in cancer cells by producing ROS from blood sugar.

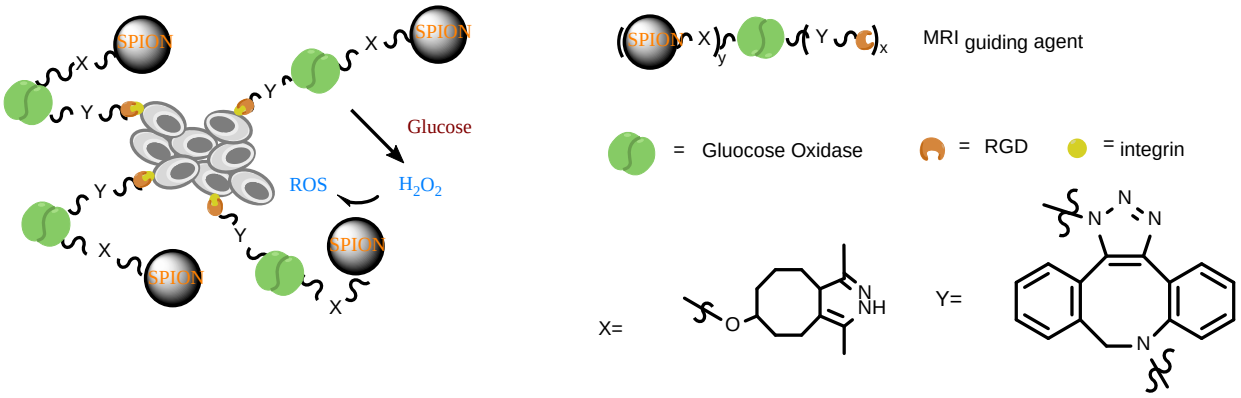

Figure 8. Schematics for targeted destruction of tumor cells by SPION-GOx bioconjugates.

As shown in Figure 8, The mechanism of the destruction of tumor cells is basically that: aggressive tumor cell proliferation induces elevated glucose concentration in tumor[130, 131]; H_2O_2 is released when glucose comes into contact with GOx and it is oxidized to gluconolactone; afterwards, H_2O_2 diffuses to the surface of SPION that catalyzes the production of ROS from H_2O_2; and high level of ROS, especially hydroxyl radicals results in highly efficient tumor cell destruction. It should be noted that RGD in this scheme is a peptide that specifically binds to the integrin $\alpha_v\beta_3$. RGD was conjugated onto GOx only when the biodistribution of GOx-RGD needed to be determined in this thesis. Cetuximab, a commercially available monoclonal antibody was also used in a previous preliminary study as a targeting agent, like RGD.

Our preliminary experimental results indicate this tumor cell destruction platform is effective and it could lead to a new cancer therapy with unprecedented low side effect and long-term effectiveness. In particular, we have demonstrated that GOx and SPION are not effective individually. Instead, they need to be conjugated in order to produce ROS in this platform. As a result, our strategy is to deliver SPION to tumor site in the first step facilitated by MRI providing the intrinsic MRI guidance ability of SPION, and then GOx will initiate production of hydroxyl radicals by forming a SPION-GOx bioconjugates. It is noteworthy that both GOx and SPION serve as catalysts in this reaction.

2.2 METHODS

2.2.1 Materials

All solvents and reagents were purchased from commercial sources and used without additional purifications, unless otherwise noted. DSPE-PEG (2000)-Amine was obtained from Alvanti (Alabaster, AL). The monoclonal antibody Cetuximab (Erbitux, 2.0 mg/mL) was purchased from ImClone Systems Incorporated (New York, NY). TCO-$(PEG)_4$-NHS and Tz-$(PEG)_4$-NHS were obtained from Fisher Scientific (Pittsburgh, PA). Sulfo Cyanine7(Cy7)-NHS ester was purchased from Lumiprobe Corporation (Hallandale Beach, FL). Glucose Oxidase was obtained from Crescent Chemical Company (Islandia, NY). All other chemicals and reagents were obtained from Sigma Aldrich (St. Louis, MO).

2.2.2 Synthesis of SPION

A narrow size distribution of the nanoparticles is the prerequisite for the uniform physical and chemical properties for further applications. Based on the prior studies, common methods to prepare Fe_3O_4 nanoparticles smaller than 20 nm include: co-precipitation of ferrous and ferric by a base[126, 132], solvothermal reaction of iron salt in a non-aqueous solvent (hexane) in presence of oleic acid and laurylamine[133], and thermal decomposition of organo-metallic compounds in an organic solvent at high temperature[12]. Hereby, SPION for the tumor cell destruction purpose were synthesized in an organic phase according to the method reported by Sun with slight modification[12]. Briefly, $Fe(acac)_3$ (2 mmol), 1,2-hexadecanediol (10 mmol),

oleic acid (6 mmol), oleylamine (6 mmol), and benzyl ether (20 mL) were mixed and magnetically stirred under a flow of nitrogen. The mixture was heated to 200 °C and stirred for 2 h, followed by reflux (~300 °C) for 1 h in nitrogen environment. After the reaction mixture was cooled down to room temperature, the SPION were precipitated by addition of ethanol into the mixture and washed with hexane and ethanol 3 times each. The as-synthesized SPION particles were dispersed in hexane.

2.2.3 Surface functionalization of SPION

SPION as synthesized from last step were well dispersed in the organic phase. However, SPION need to be hydrophilic and suspended in aqueous solution for further linkage and biological purposes. To this end, surface coating was applied to alter the hydrophobicity of the particles. Herein, the film hydration method was used to coat nanoparticles with a lipid, DSPE-PEG (2000)-amine to form micellar nanoparticles, shown in Figure 9. In aqueous solution, DSPE-PEG (2000) micelles are oblate spheroids with a maximum diameter of 18 nm. DSPE-PEG was firmly tethered to the iron oxide core via hydrophobic interaction between DSPE and oleic acid or oleylamine. At the free end of the PEG chain, amine groups were also introduced, which allowed further linkage to biological ligands[134]. Briefly, the SPION suspension was centrifuged to replace the original solvent hexane with chloroform. Subsequently, 40 mg DSPE-PEG (2000)-amine (25 mg/mL in chloroform) was added to 20 mg SPION (12 mg/mL in chloroform). The solvent was evaporated under a blanket of nitrogen to obtain the lipid film. The film was further dried in a vacuum chamber overnight to remove the remaining solvent. Finally, the coated particles were hydrated in PBS buffer.

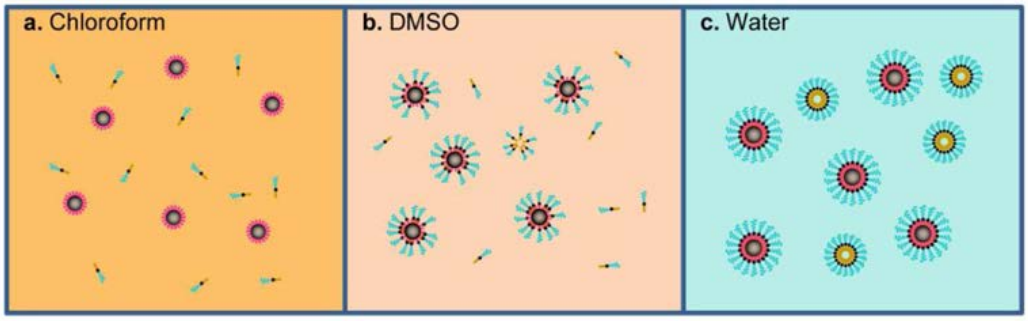

Figure 9. Stabilization of MNP using lipid DSPE-PEG (2000)-amine. Reprinted (adapted) with permission from [134]. Copyright (2010) American Chemical Society.

2.2.4 Determination of SPION concentration and amine density

The concentration of SPION dispersed in DI water was determined by measuring the Fe^{3+} concentration. After the addition of 12N HCl and 30% w/w H_2O_2, the mixture was incubated at 37°C for 2h. After being mixed with 5% KSCN, the absorbance of the resulting sample, which showed an intense red color from $FeSCN^{2+}$, was measured at 480 nm on a Plate Reader, and then compared to the standard curve.

To understand the available sites for the following NHS reactions, the density of primary amine on SPION particles after the surface functionalization was determined by a non-fluorescent reagent, fluorescamin, which reacts with primary amine to form a highly fluorescent complex (Excitation / Emission: 365/470 nm). The intensity of the fluorescence signals of the sample and standards were measured by BioTek Plate Reader.

2.2.5 Preparation of Cy7-GOx-Tz

Methyltetrazine-$(PEG)_4$-NHS ester (3.0 mg, 6.0 μmol) and Sulfo-Cy7-NHS (3.0 mg, 6.0 μmol) were added to a solution of GOx (14.6 mg, 70 nmol) in Na_2HPO_4 buffer (0.05 M, pH = 8.2, 7.3 mL), and the resulting mixture was incubated overnight in a 4 °C cold room with gentle rotation. The resulting Cy7-GOx-Tz conjugate was purified by passing through a Zeba™ spin desalting column (2 ml, MWCO 7k, Pierce) 2 – 3 times to remove excess small molecules. The concentration of Cy7-GOx-Tz was determined by Size Exclusion Chromatography (SEC) at 280nm. The retention time of Cy7-GOx-Tz under a flow rate of 0.6 mL/min was 17 min. The number of attached Tz group per GOx was determined by titration of Cy7-GOx-Tz with the fluorescent dye TCO-Cy5, which has the maximum absorbance at the wavelength of 650nm, and does not overlap with the spectrum of Cy7.

2.2.6 Preparation of SPION-TCO

Since the acylation of primary amines is favored at pH 7 – 9, in order to achieve high conjugating efficiency, SPION particles dispersed in PBS were firstly exchanged into Na_2HPO_4 buffer (0.05 M, pH = 8.2, 4.0 mL) by a Zeba™ spin desalting column (5 ml, MWCO 7k, Pierce). Then TCO-$(PEG)_4$-NHS ester (1.5 mg, 3.0 μmol) was added into the solution of the SPION (28 mg) and incubated overnight in the 4 °C cold room with gentle rotation. To lower the possibility of particle aggregation, the resulting SPION-TCO were purified using Slide-A-Lyzer™ Dialysis Cassettes (MWCO 10k, 0.5 – 3 ml, Pierce) to remove unreacted small molecules. The SPION-TCO conjugate was dialyzed in 1X PBS buffer 1h, 2h at room temperature, and overnight in the

4 °C cold room. Finally the conjugate was collected from the cassette and concentrated with Millipore® Amicon® Ultra-4 Centifugal Filter Concentrators (NMWL 30k). 20 mg of the purified SPION-Tz was obtianed in 4.0 mL 1X DPBS. The number of TCO group per SPION was determined by titration with the fluorescent dye Tz-Cy5, accordingly, in the SEC at the wavelength of 650 nm. The retention time of SPION-TCO under a flow rate of 0.6 mL/min was 10 min.

2.2.7 Preparation of SPION-GOx bioconjugates

The above SPION-TCO (20 mg in 4 mL 1X DPBS) were mixed with the prepared Cy7-GOx-Tz (2.0 mg in 1 mL 1X DPBS), and the resulting reaction mixture was incubated 1h at room temperature with gentle rotation. The resulting SPION-GOx were injected into the SEC to confirm the conjugation efficiency. No peak of the Cy7-GOx-Tz at 750 nm would be observed if the bioorthogonal linkage between GOx and SPION was complete. 15 mg of purified GOx-SPION was obtianed in 3.0 mL 1X DPBS. The amount of immobilized GOx protein was estimated to be 45 μg/mL based on the Bradford protein assay.

2.2.8 Determination of hydrodynamic diameters of SPION-GOx bioconjugates using Dynamic Light Scattering (DLS)

Since the SPION-GOx bioconjugates are dispensed in PBS buffer when injected intravascularly into mice, the hydrodynamic diameter is an important parameter that needs to be measured and taken into consideration to ensure that no particles are with the size over 200 nm, nor

aggregation are present in the injection solution. The sizes and size distributions of the SPION, GOx, and the SPION-GOx were determined by DLS (dynamic light scattering) technique with a Zetasizer Nano ZS (Malvern Instruments, Massachusetts). Samples of 0.1mg SPION-GOx, SPION-TCO, GOx in 600 µL PBS buffer were prepared and pipetted into cuvettes that have a light path of 10 mm. A refractive index of 2.45 as that of Fe_3O_4 was obtained from the handbook[135] and used for SPION-TCO and SPION-GOx samples, while a default refractive index of protein was used in the measurement of GOx.

2.2.9 TMB based ROS assay

20 µL SPION (5.0 mg/mL), GOx (1.0 mg/mL), mixture of GOx (0.5 mg/mL) and SPION (2.5 mg/ML) without conjugation, GOx-SPION (5.0 mg/mL), and cetuximab-GOx-SPION (5.0 mg/mL) was added into 380 µl reaction buffer (0.1 M NaAc, pH 4, 50 µg TMB), followed by addition of either 100 µL of 100 mM glucose or 100 µL of DiH_2O. After the mixtures were incubated at 37 °C for 6 h on the shaker, the absorbance was scanned and measured from 800 nm to 200 nm using Cary Bio 100 UV-Vis spectrophotometer.

2.2.10 Cell Culture

4T1 cancer cells were purchased from ATCC. They were cultured in the RPMI-1640 medium containing 10% FBS, penicillin (100 U/ml), and streptomycin (100 µg/ml) at 37°C in a humidified atmosphere containing 5% CO_2 and 95% air. They were subcultured every 2 – 3 days with 0.25% trypsin-0.53mM EDTA solution at a subcultivation ratio of 1:5.

2.2.11 *In vitro* cytotoxicity evaluation of SPION-GOx bioconjugates

4T1 cells were seeded into a 96-well plate at a density of 10^4 per well and cultured at 37°C for 24h. 50 μL SPION (10 μg/mL), GOx (0.0688 μg/mL), mixture of GOx (0.0688 μg/mL) and SPION (10 μg/mL) without conjugation, SPION-GOx (10 μg/mL), or PBS (as control) was added to each well respectively, followed by addition of 100 μL of Dulbecco's Modified Eagle's medium (DMEM) containing 4 g/L glucose. After incubation for various time periods, the old DMEM medium was removed and the cells were washed with PBS 3 times. Cell viability was measured by using CellTiter-Glo viability assay kit. Basically, 100 μL CellTiter-Glo reagent was added to each well that contained 100 μL fresh DMEM. Control wells with medium but no cells were prepared for background luminescence. The contents were mixed on an orbital shaker for 2 min to induce cell lysis and incubated at room temperature for 10 min to stabilize the luminescence signal.

2.2.12 *In vitro* assessment of glucose for 4T1 cells proliferation

4T1 cells were seeded into a 96-well plate at a density of 10^4 per well and cultured at 37°C for 24h. To study the cytotoxic effects as the function of the concentration of cetuximab-GOx-SPION and glucose, 50 μL cetuximab-GOx-SPION at various concentrations was added to a 96-well plate seeded with A431 cancer cells, followed by addition of 100 μL of DMEM that contains different concentrations of glucose (4 and 20 g/L). After 1.5 h incubation, the cells were washed with PBS 3 times and then cultured in 200 μL of DMEM. After being incubated for another 12 h, cell viability was measured by using CellTiter-Glo viability assay kit.

2.2.13 *In vivo* cytotoxicity evaluation of SPION-GOx bioconjugates

Healthy female Balb/c mice (~20g) were obtained and raised under a National Institutes of Health Animal Care and Use Committee (NIHACUC) approved protocol. 16 mice were randomly divided into 8 groups, administered with a single dose of 5 mg/mL SPION-GOx in PBS at a dosage of 1, 2, 3, 4, 5, 7.5, 10, 12.5 mg/kg mouse via tail vein injection. 2 other mice were used as control with 200 μL saline administrated at the same time point. The Size and size distribution of SPION-GOx bioconjugates were determined using DLS before injection to ensure the conjugation was complete. Meanwhile, a sample from the SPION-GOx PBS solution to be used on animal study was also taken to run a TMB assay, in order to verify the effective generation of ROS. The weights and health situation of mice were monitored every day.

2.2.14 *In vivo* therapeutic efficacy of SPION-GOx on female Balb/c mice

4T1 cells (2×10^5 cell/mouse) were implanted subcutaneously into the right shoulders of female balb/c nude mice (~20 g). *In vivo* therapy experiments were performed when the tumor reached 6~8 mm in average diameter (10 days after implant). 3-5 mice were randomly assigned to 4 groups, including **Group A**: SPION-GOx, **Group B**: SPION and GOx mixture (not conjugated), **Group C**: GOx and **Group D**: blank group where only saline was injected as control. Group A were administered with a single dose of 5 mg/mL SPION-GOx in saline at a dosage of 5 mg/kg mouse via tail vein injection. Group B were injected with the mixture of unconjugated SPION and GOx at the dosage of 5 mg/kg and 8.5 nmol/kg mouse respectively. Group C received the 8.5 nmol GOx/kg mouse, while Group D were administrated with 200 μL saline as control. All

the administration was made around the same time of the day. The size and size distribution of SPION-GOx bioconjugates were determined using DLS before injection to ensure the conjugation was complete. Meanwhile, a sample from the SPION-GOx PBS solution to be used on animal study was also taken to run a TMB assay, in order to verify the effective generation of ROS. The weights and health situation of mice were monitored every day. The mice were anesthetized and dissected in 21 days of post-injection.

2.2.15 Biodistribution of SPION, GOx, and SPION-GOx bioconjugates

Healthy female Balb/c mice (~20g) were obtained and raised under a National Institutes of Health Animal Care and Use Committee (NIHACUC) approved protocol. The mice were intravenously administered with a single dose of SPION-Cy5.5 in PBS (5 mg/kg) via tail vein injection. Several other mice were used as control. The mice were anesthetized and dissected in 14 days of post-injection. The major organs (heart, liver, spleen, lung, kidney, pancreas) were dissected.

2.2.16 Evaluation of mice survival

All experiments with live animals were performed in accordance with a protocol approved by the National Institutes of Health Committee (NIHCC). Briefly, the mice were euthanized when either the tumor size reaches 1.5 cm or 21 days after treatment, whichever comes first. Therefore, the mice survival was calculated based on the life span from the date when the mice received treatment to the date when the tumor size reached 1.5 cm. For each group subjected to the

corresponding treatment, the survival rate was calculated by dividing the number of surviving mice at different days of post-treatment by the total number of mice before treatment in that group. A survival curve was then plotted.

2.3 RESULTS

2.3.1 Characterization of SPION

The SPION was synthesized through a high-temperature solution phase reaction of iron (III) acetylacetonate with 1, 2-hexadecanediol in the presence of oleic acid and oleylamine[136]. Then the amine groups were coated onto the as-synthesized SPION by ligand exchange with aminosilane to produce SPION-NH_2. The amount of amine groups on the surface of each SPION was estimated to be around ~200 based on a fluorescein quantification assay. Figure 10 shows a transmission electron microscopy (TEM) image of the SPIONs. The particles were uniform and have an average size of 8 nm. Figure 11 shows the SPION was successfully dispersed in aqueous solution after the modification with the lipid. The suspension was stable at 4°C for more than 6 months.

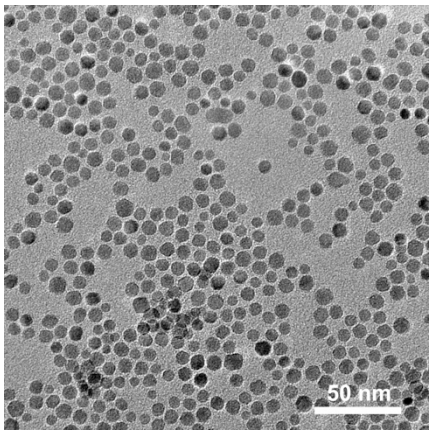

Figure 10. TEM image of SPION.

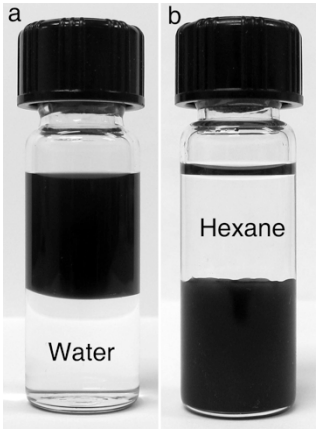

Figure 11. SPION before and after ligand exchange. a, as-synthesized SPION dispersible in hexane (upper). b, SPION-NH_2 dispersible in water (lower) after exchanging the ligand with amine groups.

2.3.2 Determination of SPION-GOx bioconjugates' hydrodynamic size and size distribution

Dynamic light scattering is a common physical method to measure molecule size and distribution in suspensions. A monochromatic light source, usually a laser, is shot into the sample. The principle of DLS is that when the light hits the molecules (smaller than 250 nm) in the solution, it gets diffracted in all directions, i.e., Rayleigh scattering. The scattering intensity fluctuates over time because the small molecule undergoes Brownian motion. Then the scattered lights from different molecules interfere with each other constructively or destructively, which also contributes to the information of time scale of scatters' movement. The dynamic information of the particles is then derived from an autocorrelation of the intensity trace recorded. The second order autocorrelation curve is generated from the intensity trace:

$$g^2(q;\tau) = \frac{\langle I(t)I(t+\tau)\rangle}{\langle I(t)\rangle^2}$$

where $g^2(q;\tau)$ is the autocorrelation function at a particular wave vector, q, and delay time, τ, and I is the intensity. The angular brackets < > denote the expected value operator. The Siegert equation[137] relates the second-order autocorrelation function with the first-order autocorrelation function $g^1(q;\tau)$ as follows:

$$g^2(q;\tau) = 1 + \beta\left[g^1(q;\tau)\right]^2$$

where the parameter β is a correction factor that depends on the geometry and alignment of the laser beam in the light scattering setup. Cumulant method is a common mathematics approach and also the method used in the Malvern software to derive information from the first-order autocorrelation function:

$$g^1(q;\tau) = \exp\left(-\bar{\Gamma}\left(\tau - \frac{\mu_2}{2!}\tau^2 + \frac{\mu_3}{3!}\tau^3 + \cdots\right)\right)$$

$$\bar{\Gamma} = q^2 D_z, \text{ with}$$

$$q = \frac{4\pi n_0}{\lambda}\sin\left(\frac{\theta}{2}\right)$$

where Γ is the average decay rate, μ_2/Γ^2 is the second order polydispersity index (PDI) which indicates the variance. The z-averaged translational diffusion coefficient D_z is derived at a single angle or at a range of angles depending on the wave vector **q**. λ is the incident laser wavelength, n_0 is the refractive index of the sample and θ is angle at which the detector is located with respect to the sample cell. Parameters beyond μ_3 should barely be used, because overfitting data with too many parameters in a power-series expansion will make all the parameters less precise[138]. Three types of distributions are commonly encountered when particle size distribution needs to be characterized. The number distribution shows the number of particles in the different size bins. The intensity distribution describes how much light is scattered by the particles in the different size bins. The volume distribution shows the total volume of particles in the different size bins. For isotropic particles, the scattering intensity from a spherical particle is proportional to the size to the sixth power. Intensity distributions emphasize the larger particles in the distribution, whereas the number distributions emphasize the smaller particles in the distribution. However, it is important to know that both are just different representations of the same physical reality of a distribution of different sizes.

Therefore, the size distributions both by number and intensity of SPION and SPION-GOx are shown in Figure 12-15 to provide more detailed information on the size and size distribution changes before and after the SPION-GOx bioconjugates being formed. The Z-average diameter and polydispersity index (PDI) characterizing the size distribution are

summarized in **Table 1.** Basically, the Z-average size of SPION is approximately 62.74 nm, while the SPION-GOx bioconjugates are 76.53 nm. The 14 nm in size difference is the exact size of the globular protein GOx, indicating the successful conjugation formed between SPION and GOx.

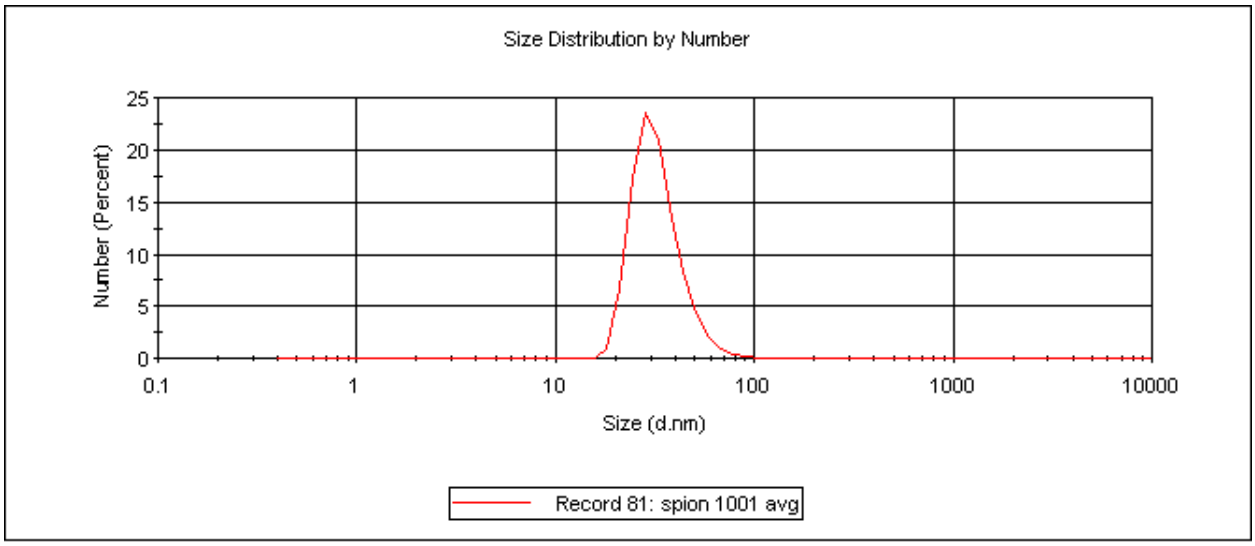

Figure 12. Size distribution by number of SPION.

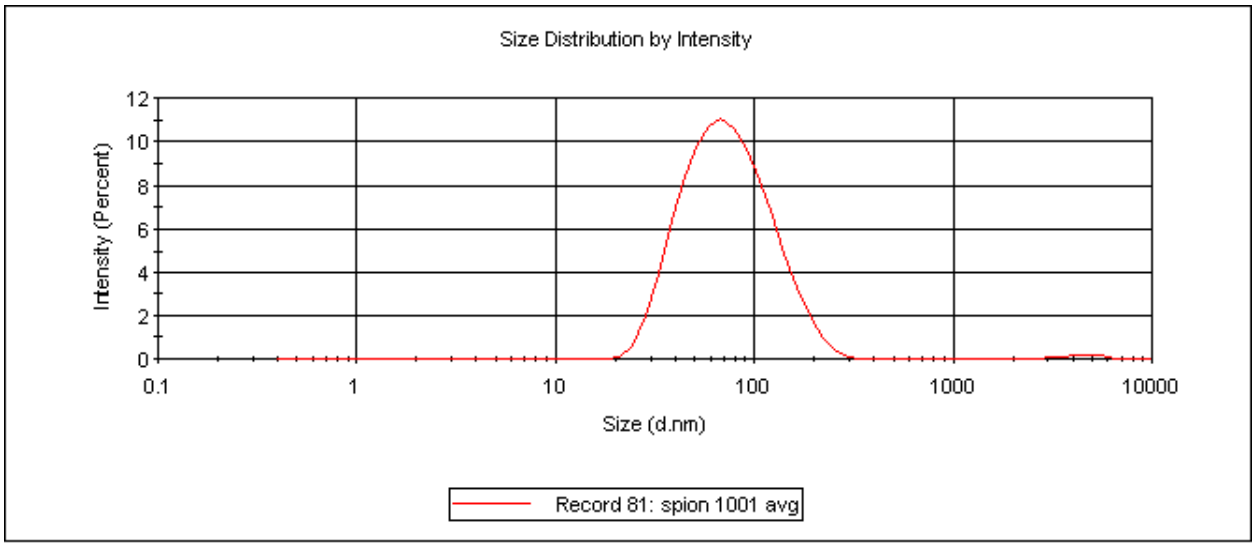

Figure 13. Size distribution by intensity of SPION.

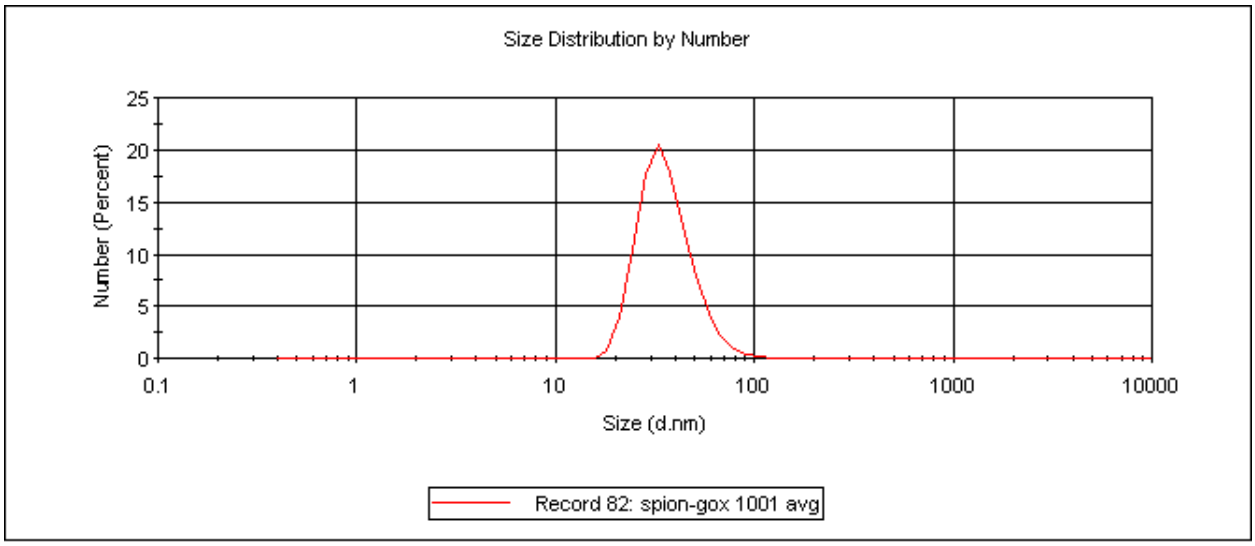

Figure 14. Size distribution by number of SPION-GOx.

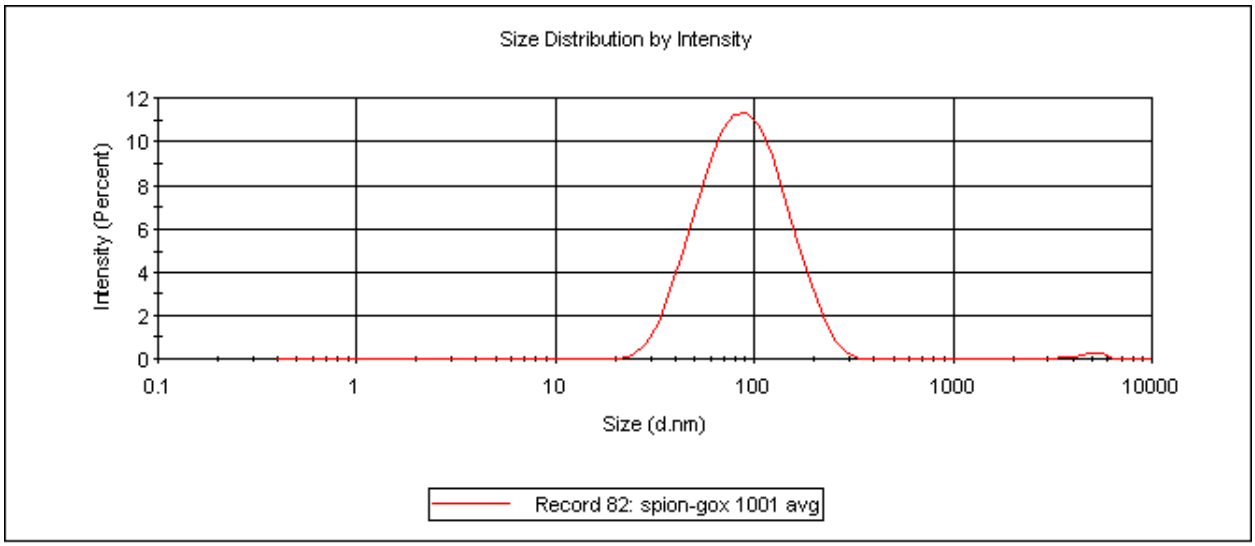

Figure 15. Size distribution by intensity of SPION-GOx.

Table 1. Summary of DLS results

Particles	Z-average (avg ± sd) /nm	PDI
SPION-GOx	76.53 ± 1.18	0.169 ± 0.0095
SPION	62.74 ± 1.28	0.151 ± 0.019

2.3.3 Determination of ROS generation by TMB assay

Formation of ROS from the SPION-GOx bioconjugates was visualized by using a chromogenic substrate 3, 3', 5, 5'-tetramethylbenzidine (TMB). It produces a blue color when highly active ROS is present in the solution so that it can be detected at the wavelength of 650 nm using a UV-Spectroscopy [139-141]. In the *in vitro* study, we used an antibody, Cetuximab, instead of the

peptide RGD as targeting probe, to characterize the levels of ROS produced by GOx and SPION alone, mixture of GOx and SPION with no conjugation, as well as GOx-SPION, and Cetuximab-GOx-SPION. The result is presented in Figure 16, in which the peak appears at 650 nm on the UV-vis spectroscopy indicating the existence of ROS in the system. The result shows that presence of glucose, as a substrate, in the system is essential for producing ROS. Moreover, it suggests that neither GOx nor SPION alone is able to produce highly active ROS from glucose. It is interesting that even a mixture of unconjugated GOx and SPION cannot generate ROS. This result suggests that synergistic activity between GOx and SPION plays a key role in the process of ROS, where GOx generates hydrogen peroxide from glucose and SPION catalyzes the production of ROS from hydrogen peroxide. If GOx and SPION are not in a close distance as in the case of Cetuximab-GOx-SPION bioconjugates, the intermediate hydrogen peroxide may react with other chemicals in the system very quickly before it reaches SPION to generate ROS. The result in Figure 17 also shows that Cetuximab does not significantly change the activity of SPION-GOx in producing ROS. Figure 18 shows the change of ROS concentration in the solution as a function of time. The level of ROS in this system keeps increasing till 1 h after the reaction starts. After incubated at 40°C overnight, the blue color of the solution faded and some precipitation and aggregation of SPION-GOx were observed.

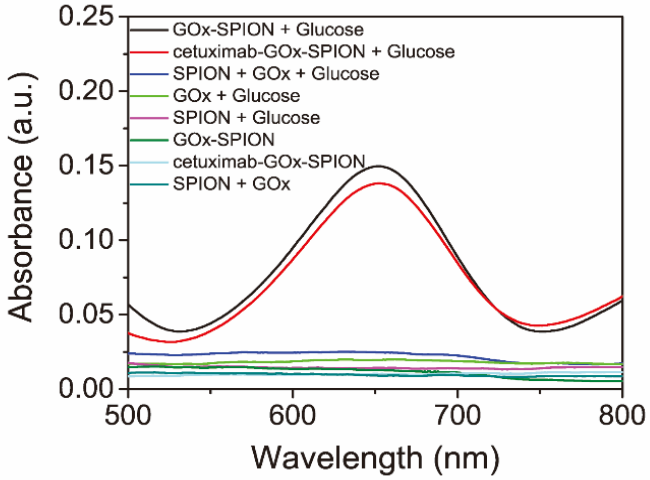

Figure 16. TMB assay absorption spectra produced by: GOx, SPION, mixture of GOx and SPION without conjugation, GOx-SPION, and Cetuximab-GOx-SPION, with and without the presence of glucose.

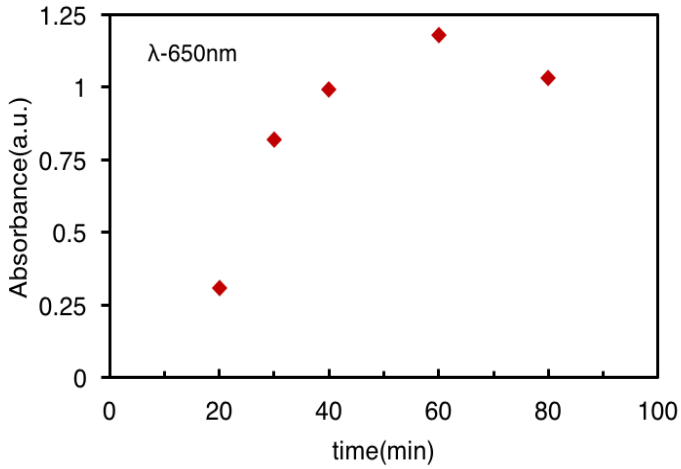

Figure 17. TMB assay absorption as results of different incubation SPION-GOx.

2.3.4 Cytotoxicity of SPION-GOx bioconjugates *in vitro* and *in vivo*

4T1 murine breast cancer cell line was used to demonstrate the tumor cell destructive capability of the SPION-GOx-RGD bioconjugates. 4T1 cells were incubated with SPION-GOx-RGD, SPION-GOx and other parallel treatments, including SPION with no conjugation, GOx, mixture of unconjugated SPION and GOx under the same condition. Cell viabilities after different treatments are shown in Figure 18, where 1X PBS buffer is used as negative control (assuming 100% viability, not shown in the chart). Treatment with 10 μg/mL SPION-GOx-RGD and SPION-GOx resulted in comparable cell viabilities after 24 h, that is, nearly no cells survived. In contrast, no significant reduction in the cell viability was observed in the groups where cells were treated with either SPION alone or the mixture of unconjugated SPION and GOx after up to 24 h in the presence of glucose with the same concentration (4 g/L).

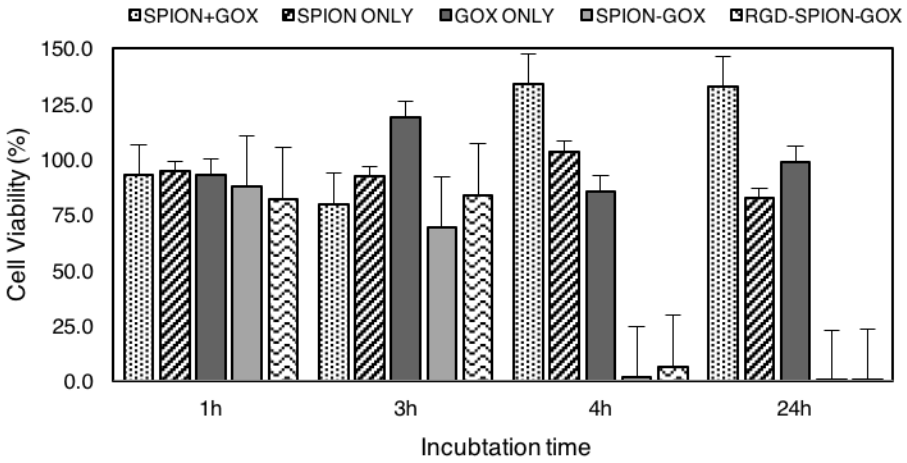

Figure 18. Cell viability 1 h, 3 h, 4 h, 24 h after treatment with mixture of unconjugated SPION and GOx; SPION only; GOx only; SPION-GOx; SPION-GOx-RGD.

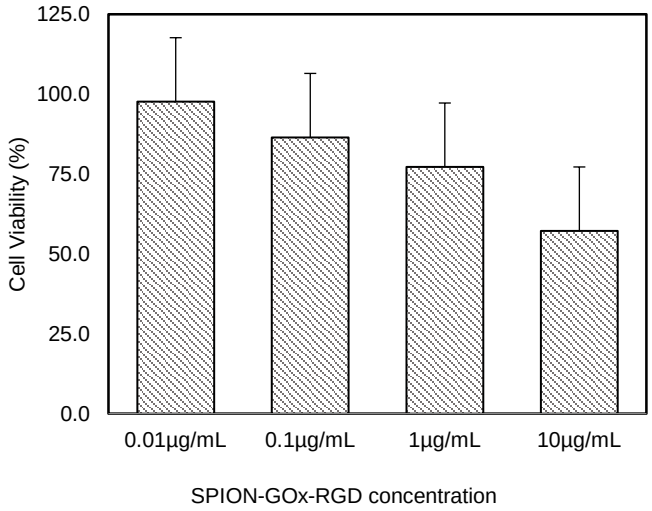

Figure 19. Cell viability 3.5 h after treatment with SPION-GOx-RGD and 4 g/L glucose.

We also studied the cytotoxicity of the system as a function of the concentration of SPION-GOx-RGD. Figure 19 presents cell viabilities after 3.5 h treatment with SPION-GOx-RGD at 4 different concentrations (0.01, 0.1, 1, and 10 μg/mL) in the presence of 4 g/L glucose. The cell viability decreases as the concentration of SPION-GOx-RGD increases.

Moreover, from the cytotoxicity evaluation of SPION-GOx bioconjugates on female balb/c mice, we found that the mice only could not last for more than 48 hours after the administration at the dosages of 10, 7.5, 6 mg/kg mouse. However, at a slightly lower concentration of 5 mg/kg mouse, the mice were able to survive despite experiencing a slight weight loss of approximately 2 g. It should be noted that the cytotoxicity study was performed on healthy mice that were not implanted with any tumor. Knowing that the SPION-GOx bioconjugates will passively accumulate at the tumor site, which has been confirmed in the biodistribution study, we hypothesized the 5 mg/kg would be a reasonable dose for the next step therapeutic efficacy study because the accumulation of the bioconjugates in other organs like

liver and kidney, would be less severe. That is to say, even though the tumor bearing mice are less healthy than normal mice, they may be more tolerant to SPION-GOx bioconjugates. The targeting peptide RGD was not conjugated to the SPION-GOx because we understood from the optical imaging and PEG biodistribution results that SPION-GOx were able to accumulate passively at tumor without the guidance of targeting agent because of the EPR effect. Moreover, a shift in project goal happened since originally, we were going to study a two-step cancer cell destruction with injecting RGD-GOx and SPION separately and let them assemble at tumor to release ROS, in order to minimize the cytotoxicity that might arise in the early stage after injection. Again, though this project was done within a tight schedule and limited resource, we still got to the same conclusion that SPION-GOx can generate the destructive ROS that causes cancer cell death.

2.3.5 Biodistribution of SPION-GOx determined by optical imaging

A preliminary animal study was also conducted to determine the biodistribution of SPION in mice. It was realized by detecting the fluorescence signals emitted by the Cyanine7 labeled SPION in the organs of interest. Animal experiments were conducted in accordance with the guidelines for the Care and Use of Laboratory Animals of the Medical Research Council of University of Pittsburgh. Optical imaging was performed with a Xenogen IVIS Spectrum imaging system (IVIS Lumina XR; excitation, 745 nm; emission, 780 nm; exposure time, 1 s; binning, medium; field of view, C). Imaging and quantification of signals were controlled by the acquisition and analysis software, i.e., Living Image 2.5 software (Xenogen, Alameda, California). Injections of SPION-Cy7 with tumor-bearing mice were performed 14 days after the

implantation of tumor cells. Each mouse was injected with 5mg Fe/kg mouse (dissolved in 200-μL saline) via the tail vein when they were anesthetized by continuous exposure to 2.5% isoflurane. Mice were sacrificed and images at the following time points were collected: 3-, 4-, 5-, 6-, and 7 days post-injection. The main normal organs, such as lung, heart, blood, liver, pancreas, spleen, kidney, stomach and intestine, muscle and bone, as well as the tumor were harvested for in vitro imaging.

It was observed from Figure 20 that SPION had accumulated on the tumor site on the third day after injection. This passive accumulation is due to the enhanced permeability and retention (EPR) effect, which is a property of nanoparticles with ultra-small sizes tending to accumulate in tumor tissue much more than they do in normal tissues. Biodistribution of SPION concentrations in various organs, in the rank order of magnitude, was liver > kidney > pancreas> other. This result shows that SPION mainly accumulates in the liver. The concentration difference in the distribution results from the SPION metabolism.

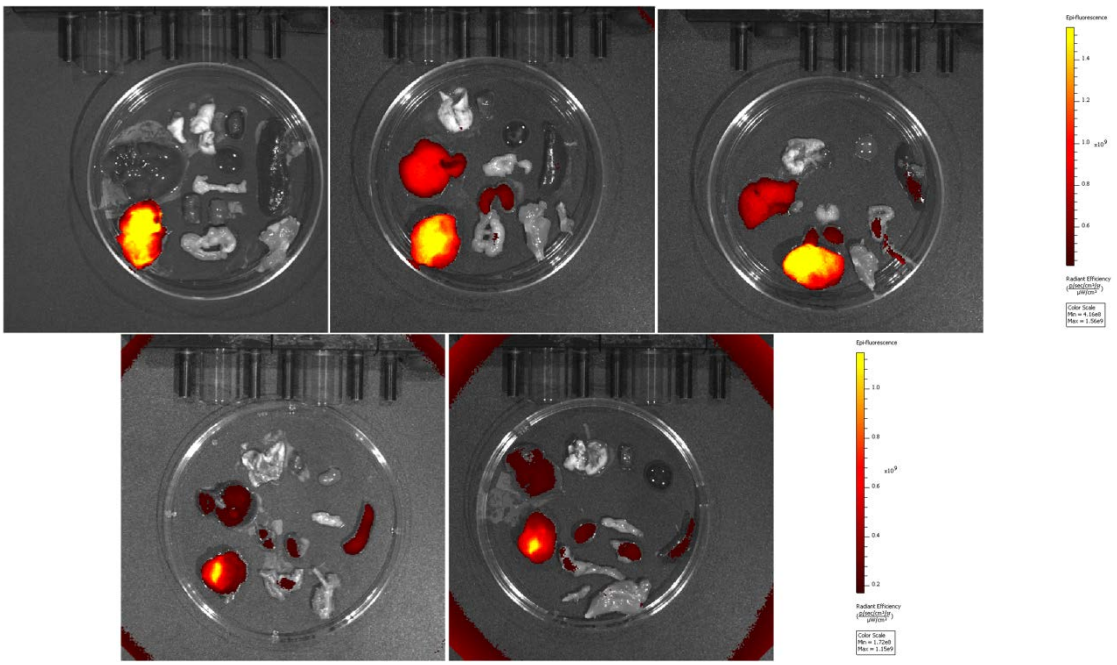

Figure 20. Biodistribution of SPION-Cy7. 3-, 4-, 5-, 6-, 7 days post injection. From upper to lower, left to right: lung, heart, blood, liver, pancreas, spleen, tumor, kidney, stomach and intestine, muscle and bone.

2.3.6 *In vivo* therapeutic efficacy of SPION-GOx on female Balb/c mice

By measuring tumor sizes and weight after treatment, we can evaluate the therapeutic effect of SPION-GOx bioconjugates on 4T1 cancer cells in animals. Shrinking tumors are promising signs indicating the effectiveness of the ROS introduced from SPION-GOx bioconjugates on cell destruction, while no severe toxicity effect like significant weight loss or animal death should be observed. The normalized tumor sizes since the day of mice receiving treatment after tumor implantation in each treatment group are shown in Figure 21.

A great slowdown of tumor growth is observed in the mice treated with SPION-GOx (red) as compared to the all 3 control groups, which agrees with the cell study results that the ROS generated from the conjugated SPION-GOx could effectively destruct cancer cells. The

mice in this group experienced a weight loss of ~2g in the first 4 days but grew back to their normal weights before treatment and kept constant soon after the drop. Unconjugated SPION and GOx (blue), and GOx alone (yellow) both stimulated the tumor growth in the 21-day span, which can be explained by the double role that ROS play to cause cell proliferation when a slight increase in ROS level is introduced. While SPION and GOx mixture yield a steady tumor growth, treatment with GOx at a concentration of 8.5 nmol/kg mouse created an explosion. One mouse in saline group had very fast-growing tumor that yields the outlier in that group and contributes to a large standard deviation on Day 10. It was sacrificed at day 12, leading to a decrease of average tumor size growth rate in the group.

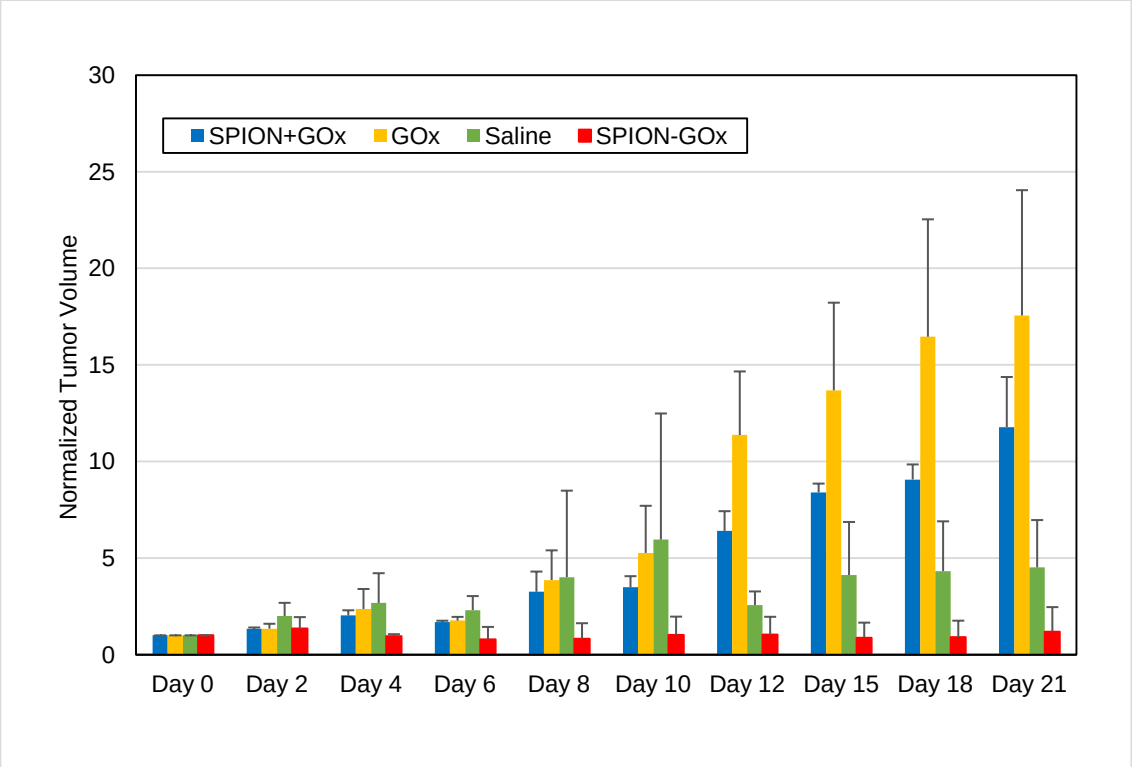

Figure 21. Therapeutic efficacy of the SPION-GOx bioconjugates. 3-5 female balb/c mice bearing 4T1 tumor cells were assigned to each group. The 4 groups were administrated at Day 0 with: unconjugated SPION and GOx (blue), GOx (yellow), saline (green) and SPION-GOx (red), respectively. All mice were sacrificed at Day 21 after tumor size and weight measurement.

2.3.7 Survival curve

The survival curve indicating the living status of the animals is shown in Figure 22. All the decreases in animal number were related to sacrifice due to the outgrowing tumor. No animal died from any type of treatment (SPION-GOx and three control groups, including GOx, unconjugated SPION and GOx mixture and saline) in the 21-day study. Additionally, the SPION-GOx bioconjugates slowed down the tumor growth dramatically so that there were no mice sacrificed until the end point of the *in vivo* study. However, due to a limited number of

animals used in each group, the death of one mouse affects the survival curve result tremendously.

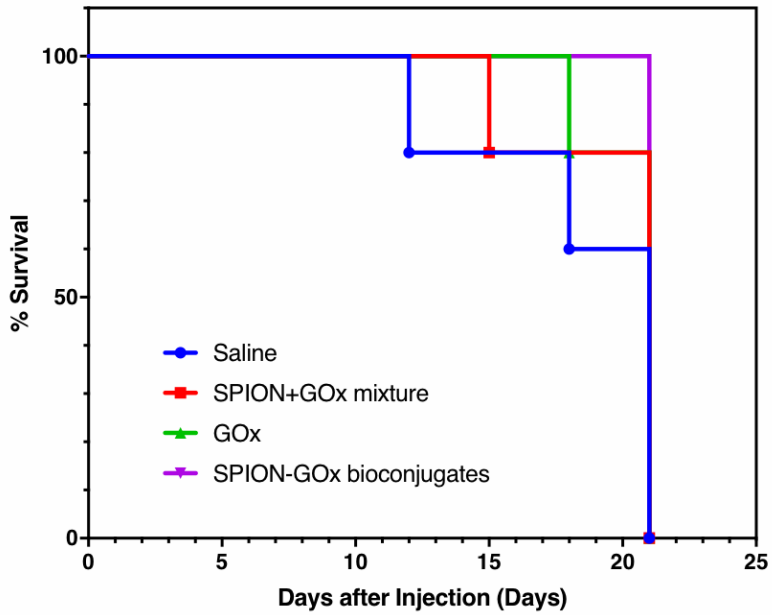

Figure 22. Survival curve.

2.4 DISCUSSION

It is evident that SPION-GOx bioconjugates are able to destruct tumor cells both *in vitro* and *in vivo* via in situ production of ROS. This low side effect treatment can be a promising strategy for cancer therapy.

Uniform and ultra-small size iron oxide nanoparticles were essential for the bioconjugates to effectively accumulate at tumor through EPR effect. Therefore, the thermo

decomposition method was chosen to meet the specific size requirements. The as-synthesized nanoparticles were characterized by transmission electron microscopy (TEM) that shows the Fe_3O_4 core and later using dynamic light scattering (DLS) that represents the hydrodynamic diameter and size distribution when the nanoparticles were functionalized with the PEG chain to be dispersible in aqueous solution. The thickness of the coating layer from the DSPE-PEG2000-NH_2 in aqueous solutions can be estimated with a scaling model, which was originally developed by Johnsson et al[142]. Briefly, the thickness of PEG layer is determined by the following factors: the number of monomeric units per PEG chain, the statistical length of a monomer (= 0.39 nm), the number of PEG chains on the surface, and the radius of the core. It should be noted that both Fe_3O_4 core and the lipid bilayer formed by DSPE and oleic acid/oleylamine contribute to the radius of the core. The lipid bilayer is usually assumed to be the same size of cell membrane (~ 3 nm). The experimental measurements from TEM and DLS agree with theoretical predictions. After the particles were prepared and stabilized, the functionalization of SPION and GOx using click chemistry was performed following a similar procedure. The key step to modify SPION and GOx with the NHS esters is to adjust the pH to 8-9. This is because hydrolysis is a competing reaction with primary amines of proteins/peptides. Acylation is favored using concentrated protein solutions (1 - 5 mg/ml) at pH 7 - 9. It is also important to use an amine-free buffer for the NHS ester reactions. Buffers containing primary amines (e.g. Tris, Glycine) would result in a loss of available NHS esters for the main reactions. NHS esters are moisture-sensitive and readily hydrolyze, so that they need to be dissolved in a dry water-miscible organic solvent such as DMSO or DMF prior to use.

Secondly, the single peak from UV-vis FPLC as well as Z-average particle size from DLS indicated that the click chemistry is an effective method for conjugation of iron oxide

nanoparticles with another large biomolecule, GOx. This is an important progress in the work because the conjugated product is the foundation of the successful generation of ROS and the prerequisite of the delivery to tumor site without a targeting agency attached. It was one of the most challenging preparation steps due to the intrinsic inconsistency of nanoparticles and the batch-to-batch difference because amine functionalized SPION were purchased from OceanNanotech for further modification with TCO-PEG4-NHS esters because of the limited time.

The *in vivo* cytotoxicity evaluation result shows that the mice could tolerate the SPION-GOx at 5.0 mg/kg mouse from a single injection. From the biodistribution obtained from optical imaging, we observed the significant accumulation of SPION-GOx in the tumor, while as time goes by, the residues in other major organs, like liver, kidney, and pancreas were slowly cleared. This result suggests that the SPION-GOx can remain at the tumor site generating ROS as a long lasting therapeutic cancer drug, which is convenient for patients since frequent repeating injections are avoided. Due to the limited resources, in the cytotoxicity assessment, each dose was administrated on only 2-3 mice. This could possibly result in a “pseudo positive” conclusion because of the lack of statistical analysis from multiple data points, which can be resolved by an experimental design with a greater number of animals assigned in each group, and a comprehensive animal study with complete demonstration with all positive and negative control groups.

The key experiment to test the production of ROS from the SPION-GOx system is using the TMB assay. The TMB assay results of the peaks at 650 nm on the UV-vis spectroscopy indicated the existence of ROS in the system. In addition, the result showed that neither GOx nor SPION alone is able to produce highly active ROS from glucose, which is the substrate that is

essential for production of ROS. It is noticeable that a mixture of unconjugated GOx and SPION does not generate as much ROS as the conjugated SPION-GOx does. This result suggests that synergistic activity between GOx and SPION plays a key role in the process of ROS, where GOx generates hydrogen peroxide from glucose and SPION catalyzes the production of ROS from hydrogen peroxide. If GOx and SPION are not in a close enough distance as in the case of SPION-GOx bioconjugates, the intermediate hydrogen peroxide may react with other chemical species in the system quickly before it reaches SPION to generate ROS. Another significant result of our experiment is that mass production of ROS and destruction of cells only takes place when SPION and GOx are conjugated. This sheds new lights to an alternative therapy with unprecedented low-side effect and specificity by first delivering the SPION to specific tumor and then introducing the targeting agent modified GOx to initiate the ROS production. Distinguishable from other ROS-mediated therapies, our platform only requires blood glucose as the reactant for the production of ROS, and it turns a nutrient required for tumor proliferation into a cytotoxin that destroys the tumor cells.

A concern with the platform is the systematic variation introduced by the nanoparticles. Some inconsistency exists from batch to batch, which sometimes leads to inexplicable results. For example, when we were coupling the TCO-PEG4-NHS onto the SPION surface, using the reaction condition, we got very different TCO per SPION results from different batches of nanoparticles. Therefore, repeatability is an issue that needs to be taken into consideration to make any rigorous conclusion.

Overall, our study demonstrates that SPION-GOx bioconjugates is a promising approach for cancer therapy with low side effect in normal tissues but long lasting targeted cancer cell destruction capability. Additionally, with the intrinsic MRI guidance ability, SPION-GOx

delivery process can be guided and confirmed by MRI, which lays the ground for imaging-guided drug delivery and potentially a theranostic (combination of diagnostics and therapy) platform.

3.0 MULTISTAGE SEPARATION OF CELLS USING HYDROPHOBIC INTERACTIONS ENABLED BY TEMPERATURE RESPONSIVE POLYMER

3.1 INTRODUCTION

Despite of the advanced techniques in surgery, metastasis is still one of the most critical problems that affect the prognosis of cancer patients[114]. During metastasis, tumor cells are detached from the original site and shed into the bloodstream, then arrested in the small vessels. These so called circulating tumor cells (CTCs) can finally grow into secondary tumors after they successfully survived the host defense mechanisms and established a microenvironment. In other words, CTCs are the seeds for subsequent growth of additional tumors in fairly distant organs, resulting in the majority of cancer-related deaths.

It is clinically important to find out a way that a small quantity of CTCs can be detected in the relatively large amount of blood sample. In previous studies, disseminated tumor cells in peripheral and mesenteric venous blood were detected by conventional cytology or immunocytological methods using monoclonal antibodies (mAbs), cytokeratin (CK) or epithelial cell membrane markers[115-117]. However, these staining methods are too complicated for routine use, and the sensitivity was limited by its low analysis capacity. Developments in molecular technology have made it possible to detect small numbers of tumor cells in the peripheral blood, and several previous reports have demonstrated the feasibility[42, 47].

Magnetic assisted separation has attracted considerable attentions providing a rapid and simple method for efficient separation of cell population [119, 143-145]. Basically, magnetic particles (MNPs) bind specific cells when added to cell mixture and separate them from the complex heterogeneous mixture when an external magnetic field is applied. One of the highly efficient separation is enabled by the high binding affinity and specificity of certain receptors that are immobilized on the MNPs, such as monoclonal antibody (mAb), peptide, or aptamer, which capture cells selectively[146]. A few magnetic assisted cell sorting (MACS) technologies have been established recently[144, 147-149]. CellSearch is an FDA-approved isolation system using epithelial cell adhesion molecule (EpCAM) coated magnetic beads[13, 147, 150]. The ability of CellSearch to detect circulating tumor cells (CTCs) from the peripheral blood of patients with metastatic breast cancer was validated by Riethdorf et al[151], who found that CTCs were detected in ~70% of metastatic breast cancer patients (n = 97) using CellSearch[151]. Alternatively, Hoshino et al. used a flat dimension microfluidic channel combined with high gradient magnetic field to capture magnetically tagged CTCs[149]. They achieved a 90% capture rate at a flow rate of 10 ml h-1, with 25% fewer particles being required in comparison to CellSearch[149].

However, a major obstacle that hinders the MACS from achieving adequate separation efficiencies is non-specific interactions between cells and MNPs. For instance, epithelial-specific antibodies can label not only non-tumor epithelial cells by specific labelling, but also non-tumor non-epithelial cells by non-specific labelling, thus giving false positive results[152].When very large separation efficiencies are required, problems caused by the non-specific interactions become significant and challenging[153, 154].

Herein, we report a multistage cell separation platform to circumvent the challenge resulting from non-specific interactions in current single-stage magnetic separation, shown in Figure 23. In this platform, we utilized poly(N-isopropylacrylamide) (pNIPAM) which has been applied in protein purification[155-157] and cell separation[158-160], as it undergoes a unique reversible phase transition at its lower critical solution temperature (LCST) of ~32°C[161]. By manipulating the hydrophilic-to-hydrophobic phase transition of the polymers simply through temperature cycling, we were able to reversibly capture and release target cells when pNIPAM was grafted onto both MNPs and target cells. In this work, A431 and HeLa cell lines were used as target and non-target cells, respectively, for their significant difference in epidermal growth factor receptor (EGFR) expression level[162], while Cetuximab (C225) was the mAb used to bind to EGF receptor at a high binding affinity (K_d = 0.39 nM)[163]. Flow cytometry was utilized in the analysis of cell counting. The results showed an increasing enrichment factor after multiple separation cycles, which indicates that A431 cells (target) can be effectively separated from HeLa cells (non-target) using the multistage platform and that the separation efficiency increases with the number of separation cycle.

The key approach to the multistage separation is based on reversible hydrophobic-to-hydrophilic transition of the polymers tethered to the magnetic particles (MNPs) and target cells by changing the temperature. Zhu et al has utilized temperature change in their microfluidic separation device to release the captured CCRF-CEM cells from DNA aptamer sgc8c by raising the temperature to 48°C [164]. In order to provide a mild environment for cells, among various temperature-responsive polymers that undergo a reversible phase transition in aqueous solutions upon changing of the temperature [7-11], poly(N-isopropylacrylamide) (pNIPAM) is chosen in this work. PNIPAM exhibits a well-known temperature-responsive phase transition in aqueous

solution at its LCST of about 32°C [12,13]. It is hydrophilic and water-soluble when the temperature is below LCST but becomes hydrophobic and aggregate in aqueous solutions when the temperature is above LCST. The aggregation can be dissolved in aqueous solutions when the temperature is decreased to below LCST again. This reversible hydrophilic-to-hydrophobic transition is believed to be accompanied by a conformational change of the polymer chain from a disordered, random hydrophilic coil to an ordered, collapsed hydrophobic globule. By attaching pNIPAM to both target cells and MNPs, target cells can be captured and released by the MNPs at a higher efficiency than the non-target cells, which may also be captured and released by the MNPs due to non-specific interactions. The difference in the capture-and-release efficiencies of target cells versus non-target cells in a single cycle will be amplified by multiple separation stages, following a similar concept of the distillation process. Therefore, the overall separation efficiency will increase with the number of separation stages.

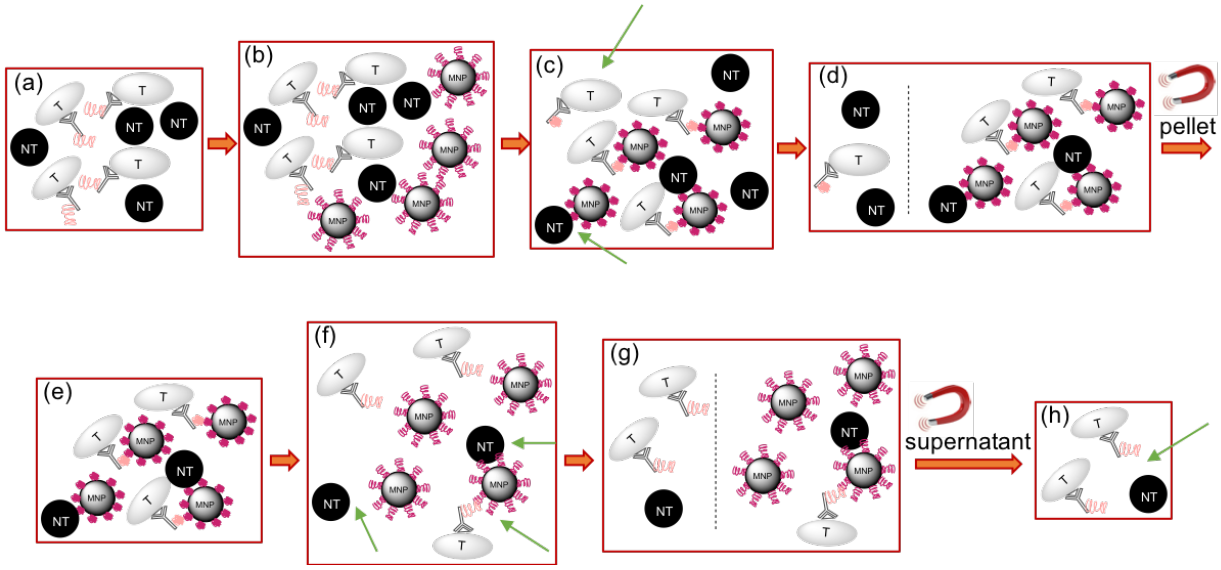

Figure 23. Realistic process flow for multistage separation scheme. (a) Cycle starts with a mixture of target (T) and non-target (NT) cells; (b) PNIPAM-MNPs added; (c)Trigger pNIPAM to its hydrophobic conformation at 37 °C, some target cells may not be captured while some non-target may get captured; (d) Attract MNPs in a magnetic field; (e) Disperse the pellet in fresh buffer; (f) Trigger pNIPAM to hydrophilic phase by cooling the mixture to 4°C, some target may still be attached on MNPs, and some non-target may escape; (g) Separate the MNPs in a magnetic field, the pellet may contain some target while the supernatant may have some non-target; (h) Cycle ends with target-rich in the supernatant but not a complete separation of target from non-target cells.

To tether pNIPAM to MNPs, poly(acrylic acid)-modified Fe_3O_4 magnetic particles (PAA-MNPs) were synthesized in a solvothermal method and amino-terminated pNIPAM was covalently attached to the MNPs via coupling the amine group with the carboxyl groups. On the other side, to selectively attach pNIPAM to target cells, we first conjugated pNIPAM to protein A, which is a secondary antibody that binds the Fc region of immunoglobulin G (IgG) from many mammalian species with a high specific binding affinity[165]. Carboxylic acid terminated pNIPAM (pNIPAM-COOH) was used to react with protein A to form stable amide linkages. Therefore, when the pNIPAM-protein A is mixed with the targeting mAb Cetuximab, the resulting pNIPAM-protein A-Cetuximab complex can selectively capture the cells that overexpress EGFR. It has been reported that the LCST of pNIPAM conjugated to protein A through this approach does not change significantly after the conjugation[166]. Cetuximab is

previously labeled with fluorescence dye to distinguish target cells from non-target cells in the cell mixtures for the subsequent flow cytometry analysis.

After the preparation of pNIPAM tethered MNPs and pNIPAM-protein A-Cetuximab complex, the separation process starts with adding pNIPAM-MNPs to the cell mixtures containing both the target and the non-target cells. Subsequently, the cell mixture is incubated up to 37 °C for 10 min in the dark. The aggregates are then collected by a neodymium−iron-boron magnet attached to the wall of vials. The magnetically collected cell pellet is separated from the bulk solution by removing the supernatant. After the cell pellet is redispersed in the cold PBS buffer, the resulting cell suspension is incubated at 37 °C again and ready to be captured by the MNPs. After multiple capture-and-release cycles described above, the overall or enrichment factor is therefore amplified to achieve a high separation efficiency.

3.2 METHODS

3.2.1 Synthesis of MNP

The PAA-MNPs were synthesized using the solvothermal method. Briefly, $FeCl_3$ (0.8 g) was dissolved in ethylene glycol (40 mL) with vigorous stirring, followed by addition of NaOAc (3.6 g) and PAA (1.0 g). The mixture was stirred continuously for 30 min, sealed in a Teflon-lined stainless-steel autoclave, and then reacted at 200 °C for 10 h. After the reaction, the autoclave was cooled to room temperature. The products were collected, washed several times with ethanol, and then dried under a vacuum at 60 °C before characterization and usage.

3.2.2 Characterization of MNP

The size and morphology of the as-synthesized PAA-MNPs were characterized using scanning electron microscopy (SEM, Philips XL-30 field, 15 kV). The crystal structures of the PAA-MNPs were examined by using powder X-ray diffraction (XRD) (Philips X'pert Diffractometer using CuKα radiation, λ=1.54178 Å). The sample of PAA-MNPs was washed five times with ethanol, redispersed in water and dried in a powder form.

3.2.3 Modification of MNP with pNIPAM

The carboxyl group on the surface of PAA-MNPs was covalently linked to the amino-terminated pNIPAM via 1-ethyl-3-(3-dimethylaminopropyl) carbodiimide hydrochloride (EDC) chemistry. The PAA-MNPs (0.5 mL, 2.5%) were washed three times in 0.1 M carbonate buffer (pH 9.6) and then another three times in 0.1 M MES buffer (pH 6.5). After washing, the MNPs were redispersed in MES buffer. To activate the carboxyl groups, fresh solution of EDC (2%, w/v) in MES buffer was added and the mixture was incubated for 3 h at room temperature in the dark. After incubation, the MNPs were washed three times with MES buffer to remove the unreacted EDC. Then, the MNPs (1-fold) were redispersed in 0.1 M borate buffer (pH 8.5) and 50-fold amino terminated pNIPAM was added for the functionalization. The mixture was incubated overnight at room temperature in the dark. Following conjugation, the MNPs were magnetically separated and thoroughly washed with PBS (pH 7.4) to remove unbound amino-terminated pNIPAM. The MNPs were then rinsed thoroughly, and finally stored in storage buffer (PBS,

0.1% BSA w/v) with a concentration of 1 mg/mL at 4 °C. Similar procedure was used for grafting of carboxyl-terminated pNIPAM to Protein A.

3.2.4 Fluorescence labeling of Cetuximab with FITC

Saturated Sodium bicarbonate ($NaHCO_3$) solution was firstly added to 1ml of 2mg/mL (0.013 nmole) Cetuximab stock solution to adjust pH to 8-9. 0.063 mg (0.13 nmole) 5(6)-Carboxyfluorescein N-hydroxysuccinimide ester dissolved in DMF was added to the Cetuximab solution and incubated at 37°C for 4 h. Afterwards, the excess fluorescence dye was removed by desalting column with a cutoff molecular weight of 7,000. The product was dissolved in PBS buffer (pH 7.4) and ready for use.

3.2.5 Multiple separation enabled by reversible capture-and-release of target cells using pNIPAM-MNPs

The A431 cells and HeLa cells were cultured following the ATCC cell culture procedures. After the cells were harvested from cell culture flasks and counted using a hemocytometer, the two types of cells were mixed at several ratios, including A431: HeLa = 1:1, 1:2, 1:10, 1:20. The cell mixtures were incubated with the protein A-pNIPAM complex at 37°C for 1 h in the dark.

The separation process started with adding a certain amount of pNIPAM-MNPs to the mixtures containing both the target and the non-target cells. Subsequently, cell suspension of 1 mL 4 °C PBS buffer was warmed up to 37 °C and then incubated for 10 min in the dark. The aggregates were then collected by a neodymium−iron-boron magnet attached to the wall of vials.

The magnetically collected cell pellets were separated by removing the supernatant and then redispersed in a 4 °C PBS buffer. The resulting new cell suspension was again incubated at 37 °C for 10 min in the dark. The above capture-and-release cycle was repeated for a specified number of times as needed. A small amount of cell mixture sample was taken after each separation process for flow cytometry cell counting.

3.2.6 Flow cytometry

Samples from cell mixtures were counted and the numbers non-target (HeLa) and target (A431) in PBS buffer after each capture-and-release cycle were determined using a BD FACS Aria flow cytometer (BD BioSciences, San Jose, CA).

3.3 RESULTS

3.3.1 SEM of PAA-MNP

To demonstrate the feasibility of the multistage cell separation scheme, we firstly performed a proof-of-concept experiment by using polystyrene (PS) microspheres to mimic cells. Fluorescent PS microspheres grafted with pNIPAM were used to mimic target cells; carboxylate non-fluorescent PS microspheres (bare spheres with no pNIPAM on the surface) were used to mimic non-target cells, noted that the temperature-responsive polymer pNIPAM was covalently linked to the target spheres in advance. The size of the microspheres is about 5 μm, which is on the

same length scale as cells. Two types of PS microspheres were first mixed and then separated in multiple stages.

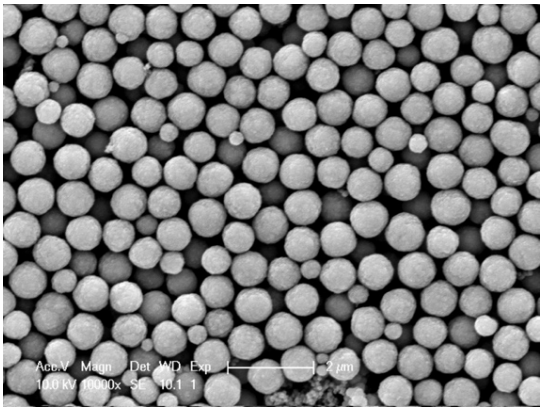

Figure 24. SEM image of poly (acrylic acid) modified MNPs (PAA-MNPs).

Poly(acrylic acid)-modified MNPs (PAA-MNPs) were synthesized and tethered with pNIPAM in a one-step solvothermal method, in which PAA acted both as a ligand and a surface functionalization agent. Figure 24 presents an SEM image of the resulting products. The as-synthesized PAA-MNPs are uniform spheres of about 300 nm in diameter. The PAA-MNPs were well dispersed in water by sonication and the suspension remained stable for more than 0.5 h before precipitation started. The PAA-MNPs were attracted to where the magnet was placed and agglomerated at the vial wall within a few seconds, leaving the supernatant clear. After removing the magnet, the PAA-MNPs were easily redispersed in water with gentle shaking. These results indicate that the synthesized MNPs possess both a high magnetization (so that they can be effectively separated from solution by using a moderate magnetic field) and a superparamagnetic

property (so that the aggregated MNPs can be easily re-dispersed in solution upon removal of the magnetic field). Both properties are required for the separation proposed here.

3.3.2 Multistage separation of A431 from HeLa cells result analysis using flow cytometry

After the demonstration of the separation scheme with microspheres, we moved on to real tumor cells. The cell lines we used here were A431 and HeLa as targets and non-targets, respectively, with their significant difference in expression level of epidermal growth factor receptor (EGFR). EGFR is a membrane bound protein related to cell growth, proliferation for both healthy and cancerous cells. The average EGFR density on A431 cell surface was found to be 636/ μm^2 with an estimation of 5×10^5 EGFR per cell measured by Surface Plasmon Resonance imaging (SPRi) technique, while HeLa were found to be 270 receptors/μm^2, corresponding to 0.53 per cell, much lower than A431. Other than linking pNIPAM to target spheres directly, when it came to cells, pNIPAM were firstly conjugated to protein A and then form a complex with antibodies which will bind to the target cells through antibody-antigen interaction. The commercialized drug used in the treatment of metastatic colorectal cancer, Cetuximab (C225), which is a chimeric IgG_1 monoclonal antibody that blocks the EGFR activation, was used in this study as the antibody that specifically binds to the targets surface.

Flow cytometry data analysis is based on the principle of gating. Gates are placed around populations of cells with common features, usually forward scatter, side scatter and marker expression, to investigate the cell population. Usually, before a flow cytometry experiment, it is a good idea to find out much information about cell lines and include the right controls. The first step in gating is often distinguishing populations of cells based on their forward and side scatter

properties. Forward and side scatter give an estimation of the size and granularity of the cells respectively. Moreover, in our case, we already know that A431 cells have a known overexpressing marker, EGFR, it was helpful to include this information by staining the cells with C225 conjugated to fluorophores as it will help identify the target cells in the later analysis for cell mixtures. Conversely a known negative, in this case, HeLa cells with low expression of EGFR, can allow us to set negative gates and determine real populations. Dead cells often have a lower level of forward scatter and are found at the bottom left corner of the density plot.

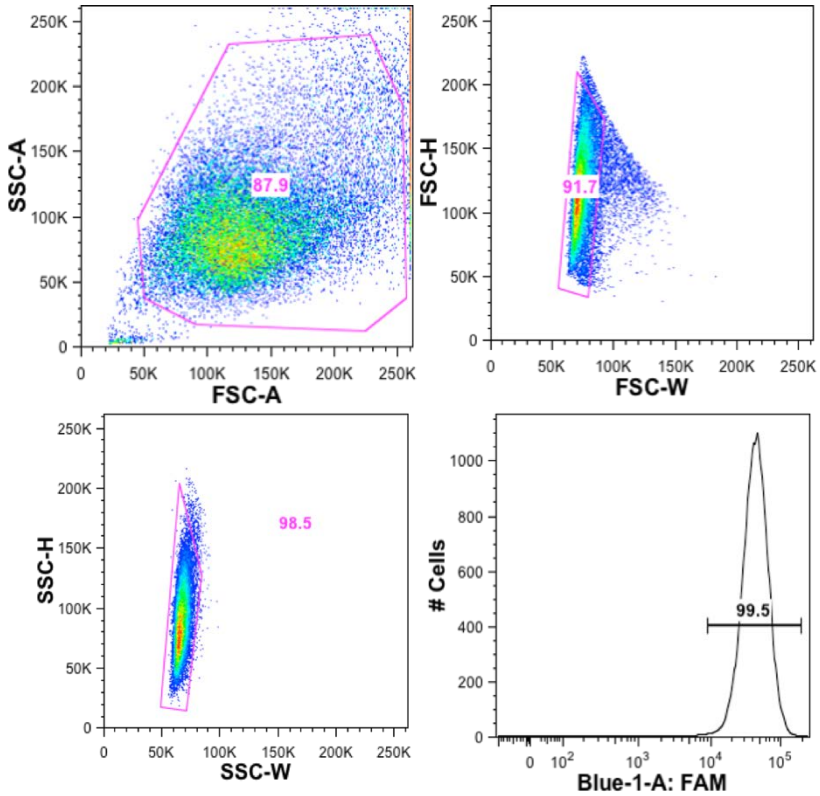

Figure 25. Gating strategies of positive control A431 cells. Top left is SSC vs FCS density plot, each dot on the plot represents an individual particle that has passed through the laser; top right and bottom left are FSC-W vs. FSC-H and SSC-H vs SSC-W respectively, which gives narrow vertical population plots; bottom right is a single parameter histogram to show the high expression of the EGFR marker on A431 cells stained with C225-FAM.

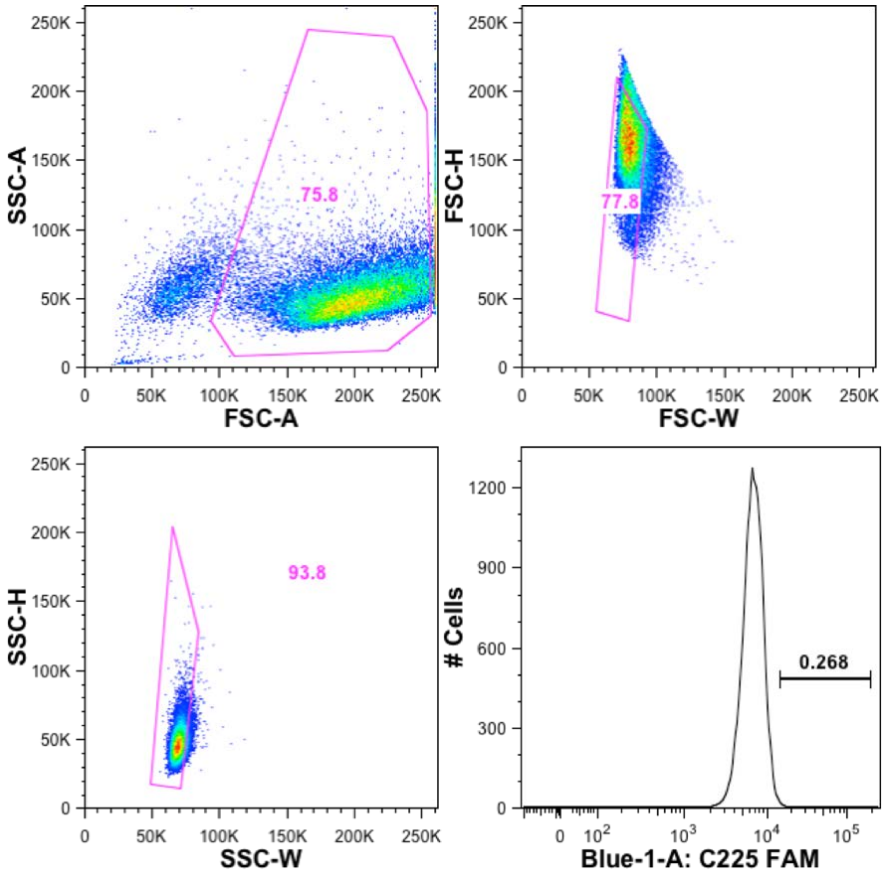

Figure 26. Gating strategies of negative control HeLa cells. Top left is SSC vs FCS density plot; top right and bottom left are FSC-W vs. FSC-H and SSC-H vs SSC-W respectively; bottom right is the histogram to show the low expression of the EGFR marker on HeLa cells incubated with C225-FAM.

Providing all the positive results from the microspheres study showing the proposed multistage separation scheme to be effective, we conducted the experiments with the two types of tumor cells to verify the feasibility of our idea in terms of biologically active cells. We mixed target A431 with non-target HeLa at ratios of ($R_{T/NT}$) of 1:1, 1:2, 1:10 and 1:20, and three separation cycles were conducted for each sample. The antibody C225 was labeled with a green fluorescein, 5 - (and-6)-Carboxyfluorescein (FAM), to create a fluorescent signal that can be identified by the detector during the flow cytometry analysis when it was bound to the target cells. We incubated the FAM-C225 with the cell mixture for 1.5h and removed the free FAM-

antibody in the solution by centrifugation. Afterwards, the pre-prepared protein A/pNIPAM conjugation was added to finally attach pNIPAM to the target cell surface.

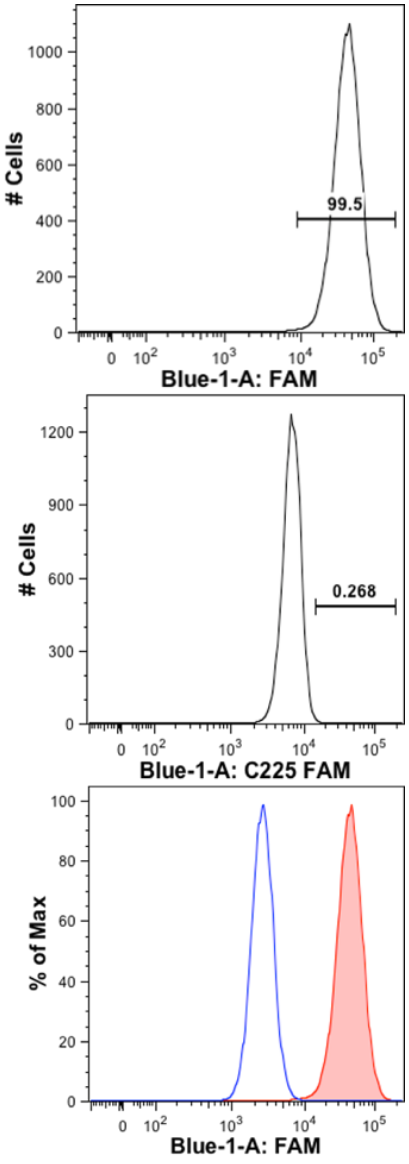

Figure 27. Top two histograms are C225-FAM stained A431 and HeLa cells, respectively; bottom histogram is the overlay of a negative population HeLa onto the stained population A431 allows easy identification of the positive cells.

Figure 25-27 shows the gating strategy adapted by analyzing the A431 and HeLa samples separately, as positive and negative controls and the regimes for the green FAM signals will fall in at the wavelength of 488nm.

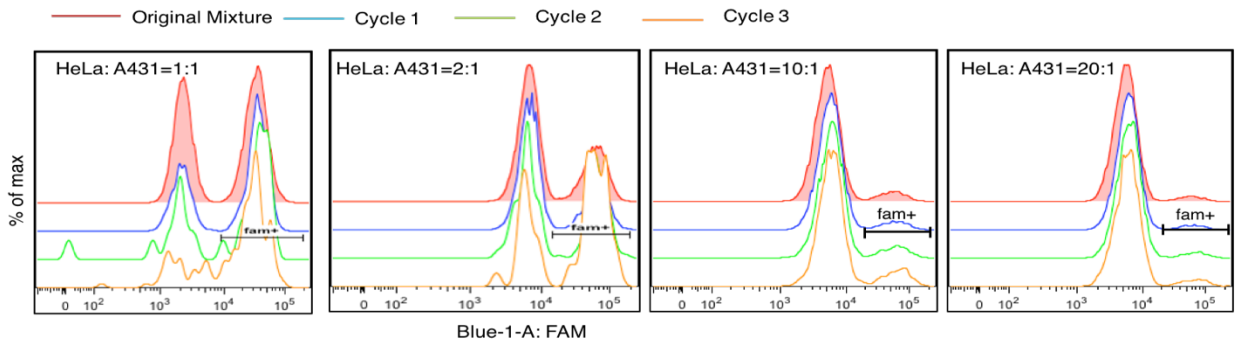

Figure 28. Stacked histogram of FAM fluorescence signals in cell mixture starting at the ratios of HeLa: A431 at 1:1, 2:1, 10:1 and 20:1.

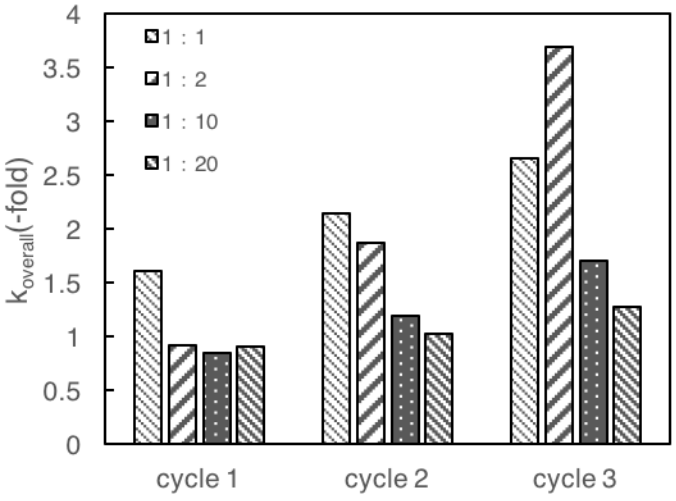

Figure 29. Overall enrichment factor $k_{overall}$ vs. the number of separation cycles with various initial ratios of target to non-target cells.

The $k_{overall}$ calculated from each sample after three capture-and-release cycles (Figure 28) are shown in Figure 29. An ascendant tendency in the overall enrichment factors as the number of capture-and-release cycles increase is still noticeable, even though the overall enrichment factors of 2.65, 3.69, 1.71, 1.27 (when the initial $R_{T/NT}$ was 1:1, 1:2, 1:10 and 1:20 respectively) are not as large as those from the microspheres separation process.

3.4 DISCUSSION

This multistage cell separation process employs the distillation concept that is commonly used in oil industry for transforming crude oil into fuels. Distillation is the process of separating the components from a mixture by selective boiling and condensation. It may result in either nearly pure products or a partial separation that increases the concentration of selected components of the mixture. When the boiling points of the components are sufficiently close so that Raoult's law must be taken into consideration, successive distillations are used to separate the components by repeated vaporization-condensation cycles. Each vaporization-condensation cycle yields a purer solution of the more volatile component. Similarly, since single stage separation cycle is not able to achieve adequate separation efficiency as mentioned, the multistage cell separation platform is designed.

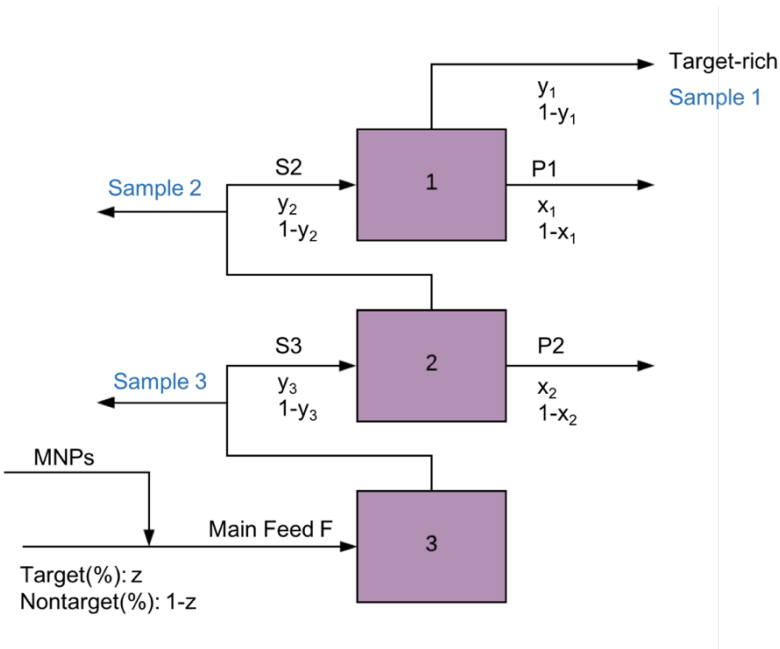

Figure 30. Schematic flow chart for multistage separation of cells.

The target cell corresponds to the more volatile component in the solution as in distillation for its higher binding affinity to the antibody as compared to non-target. In the configuration shown in Figure 30, the cells of "target-rich" streams separated from each flash cycle are used as the feed stream in the next "higher" flash cycle. A small portion of the streams is collected for flow cytometry analysis. The overall enrichment factor of this repeated separation process is y_1/z for target cells.

The as-designed multistage separation of cells using temperature responsive pNIPAM was proven to be feasible by analyzing the resulting samples from each separation. The as-synthesized PAA-MNPs were well dispersed in PBS buffer at both 4°C and 37°C until the multiple separation cycles were completed, which meets the prerequisites for maintaining stable heterogeneous cell-and-MNPs suspension. The enrichment factor for target cells shows an obvious tendency to increase as the number of separation cycles increases, which correlates with

circumvention of the non-specific interaction between MNPs and non-target cells that is described above. Similar to Zhu's strategy to release the captured cells from aptamer by temperature change[164], the capture step here was performed at a moderate temperature of 37°C with the hydrophobization of pNIPAM observed, which provides a gentler separation condition for cells as compared to 48°C.

However, the enrichment factors following the current design are relatively low, in comparison to the ones from multistage microspheres separation study[167], especially considering that the initial target to non-target ratio is much smaller in a blood sample with very rare CTCs. The low $k_{overall}$ might be caused by a few reasons. Firstly, we observed that after the second and third temperature increase to 37°C, the hydrophobic pNIPAM chains that are attached to both cells and MNPs were tangled with each other, resulted in the precipitation of some cells and MNPs from the suspension, which might be related to surface charge change. This leads to a loss of usable magnetic beads for the following separation cycle, which are essential for achieving a high separation efficiency. Adding additional MNPs after each step to the mixture is necessary to maintain the separation efficiency. Meanwhile, some of both target and non-target cells are lost as well because it was difficult to aspirate the precipitation to form a fine suspension again. Moreover, the type of MNPs added to the mixture might also be a factor that can be manipulated to achieve a higher separation effiency. Due to a limited timeframe and resources, we only used one size of MNPs at one initial concentration in this study. The system could be further optimized by tuning the size of MNPs, the density of pNIPAM on MNPs, the amount of pNIPAM modified MNPs added to the mixture, etc.

4.0 OUTLOOK AND SUMMARY

4.1 OUTLOOK

We have demonstrated that the SPION-GOx bioconjugates system can generate ROS causing cell destruction *in vitro*, while the *in vivo* cytotoxicity evaluation indicated that the toxicity of the bioconjugates were able be maintained at a low level with a dosage of 12.5 mg/kg mouse. The therapeutic efficacy of the designed system still needs to be evaluated on animal models. Meanwhile, more control groups should also be studied in the future research, including SPION only, GOx only, mixture of unconjugated SPION and GOx, and blank group (saline). The biodistribution determined from previous study was obtained by optical imaging enabled by fluorescence labeling. To have a better understanding of delivery and clearance of the SPION-GOx bioconjugates in animals starting from the tail vein injection, other imaging technologies like MRI and CT can be utilized to gain more insights.

4.1.1 Biodistribution of Zirconium-89 labeled SPION-GOx bioconjugates using PET imaging

Even though the optical imaging of solid tumors enabled by fluorescence labeling, in this case, with Cy5.5 and Cy7 for biodistribution is simple and sensitive, the mice had to be sacrificed in

order to obtain the organs of interest for an optical imaging in IVIS (In vivo imaging system). This is mainly because the near-infrared (NIR) light (700-100 nm wavelength) is capable of penetrating only several centimeters into tissue so that fluorescence signal from the internal organs deep inside mouse bodies was not intense enough to be detected [168].

An alternative approach to obtain biodistribution information is to use positron emission tomography (PET) to record and detect the γ-rays emitted by the injected radiopharmaceuticals labeled with positron-emitting radionuclide. When the radionuclide decays, a positron is ejected from the nucleus and soon annihilated with an electron to release two 511 keV γ rays that are detected by the PET scanner. The data acquired over time are collected and reconstructed into images showing radiotracer's location within the organism by algorithm developed in computer. PET has higher sensitivity and resolution and therefore has become more popular in clinical diagnosis[168]. Some commonly used radiometals are Cu, Ga, Y, and Zr, since their favorable decay characteristics are greatly useful in coordinating with biological half-lives of different targeting agents like peptides, antibodies, and nanoparticles. The major advantage of the PET imaging over the optical imaging is that the γ-rays emitted are able to penetrate the animal body so that a real-time monitoring of *in vivo* tracer distribution could be fulfilled without sacrificing the mice.

Zirconium-89 is a radioisotope of zirconium with a half-life of 78.4 hours, E_γ = 909 keV[169]. Its long half-live makes it very useful in labeling of antibodies and nanoparticles, which requires slower clearing time, thus PET imaging acquisition at a longer time point. Furthermore, when the monoclonal antibody labeled with radionuclide internalizes, ^{89}Zr-mAbs yields higher tumor-to-normal tissue ratios than the corresponding ^{124}I-labeled mAbs[170], thus showing better contrast on PET images. Hydrated Zr (IV) only exists at high dilution in very

acidic solutions, and the total coordination number of 8 is typical in their X-ray structures[168]. ^{89}Zr labeling can be achieved through several chelators, but primarily through desferrioxamine B (DFO), which forms a stable chelate with ^{89}Zr through 3 hydroxamate groups[171]. Actually in clinical PET imaging studies, all complexation of zirconium are currently performed with the chelator DFO[172]. When efficiently chelated with DFO, the ^{89}Zr-DFO complex can be conjugated to mAbs or nanoparticles without changing the biodistribution of the mAb or nanoparticle thus providing important biodistribution information by PET imaging.

Zirconium-89 is a radioisotope of zirconium with a half-life of 78.4 hours, E_γ = 909 keV[169]. Its long half-live makes it very useful in labeling antibodies and nanoparticles, which requires longer clearing time. Furthermore, when the monoclonal antibody labeled with radionuclide internalizes, ^{89}Zr-mAbs yields higher tumor-to-normal tissue ratios than the corresponding ^{124}I-labeled mAbs[170], thus showing better contrast on PET images. Hydrated Zr (IV) only exists at high dilution in very acidic solutions, and the total coordination number of 8 is typical in their X-ray structures[168]. ^{89}Zr labeling can be achieved through several chelators, but primarily through desferrioxamine B (DFO), which forms a stable chelate with ^{89}Zr through 3 hydroxamate groups[171]. Actually in clinical PET imaging studies, all complexation of zirconium are currently performed with the chelator DFO[172]. When efficiently chelated with DFO, the ^{89}Zr-DFO complex can be conjugated to mAbs or nanoparticles without changing the biodistribution of the mAb or nanoparticles thus providing important biodistribution information by PET imaging.

A few methods can be used to achieve our goal of attaching the chelator DFO to nanoparticles, including lysine methods, thiol methods, and click methods. A recent study by Perk and Vosjan *et al.* using Lysine methods was a great improvement from previous procedures

since they used a *p*-isothiocyanatobenzyl-bearing DFO (DFO-Bz-NCS)[173], which is a commercially available chelate that can form a stable thiourea linkage between chelator and antibody in one step. However, the lack of water insolubility in *p*-isothiocyanatobenzyl-DFO precursor requires more finesse than the straightforward *N*-suc-DFO chemistry[174]. Another concern with this lysine method is that nonspecific attachment in conjugation may hinder immunoreactivity if the chelate binds at an antigen-binding site. Thiol methods can do better because the conjugation through the thiol group of cysteine is more site specific, but no significant advantage in immunoreactivity was demonstrated[175]. Another method to conjugate mAbs or nanoparticles onto zirconium is the click chemistry as we have discussed above in chapter 2.1. Click chemistry is a specialized conjugation method, which expands the possibilities of ^{89}Zr PET imaging application[174]. A great advantage of click chemistry method is its modularity, which allows spontaneous conjugations between different chelator-radiometal pairs or different antibodies pairs[176]. Given that the SPIONs were already functionalized with TCO groups, and the fact that a great amount of the TCO reacting sites were still available after the reaction with GOx-Tz, click chemistry between DFO-Tz and SPION-TCO was chosen as the radiolabeling strategy here.

SPION-GOx bioconjugates were prepared as described above in chapter 2.2, followed by conjugation with ^{89}Zr. labeled tetrazine modified DFO. Briefly, DFO-Tz was synthesized by adding Tz-NHS 5μmole to DFO-NH_2 2μmole dissolved in 0.5ml DMF. Then 20μmole DIEA was subsequently added, and the reaction mixture was stirred at room temperature for 2h. Later the resulting mixture was left in the lyophilizer overnight to remove the solvent. The residue was dissolved in Acetonitrile: H_2O = 1 : 1 afterwards and purified by HPLC. Electrospray ionization mass spectrometry (ESI-MS) was used to verify the molecular weight. Afterwards, ^{89}Zr-labeled

SPION-GOx bioconjugates were prepared following the post-radiolabeling conjugation method. Briefly, Tz-DFO was radiolabeled with ^{89}Zr in 1.0M HEPES (pH = 7.0) at 95°C for 30min. The resulting Tz-(^{89}Zr) DFO with a specific activity of 0.5 mCi/nmole was then mixed with the SPION-GOx bioconjugates (0.05 mCi of Tz-(^{89}Zr)DFO with SPION) in PBS buffer. The reaction mixture was incubated at 37 °C for 60 min, and the extent of labeling was determined by FPLC. The unconjugated Tz-(^{89}Zr)DFO was removed by the Zeba spin desalting column to give ^{89}Zr-labeled SPION-GOx bioconjugates. After the successful labeling of zirconium, ^{89}Zr labeled SPION-GOx and SPION were administrated to two groups of Balb/c female mice bearing 4T1 tumors respectively using the procedures described in chapter 2.0. PET images were taken and analyzed for biodistribution.

4.1.2 Preliminary Results

ESI-MS result showed that the molecular weight of the product from DFO-NH_2 and Tz-NHS was 787.92, which is the exact molecular weight of DFO-Tz. The radioactivity FPLC radio detector results from both SPION-TCO and SPION-GOx labeled with Tz-(^{89}Zr)DFO are shown in Figure 31-32. The shape of the peaks for SPION and SPION-GOx from the radio FPLC is consistent with the ones from absorbance peaks observed from previous FPLC results without radiolabeling. The tiny peaks with the retention time of 33 minutes associate with unreacted ^{89}Zr in the solution. We can see that ~ 98% of the ^{89}Zr was successfully labeled on the SPION-TCO, while ~91% was conjugated with SPION-GOx. The shape of SPION-GOx is different from SPION, which also indicates that GOx was attached to form the bioconjugates from previous step.

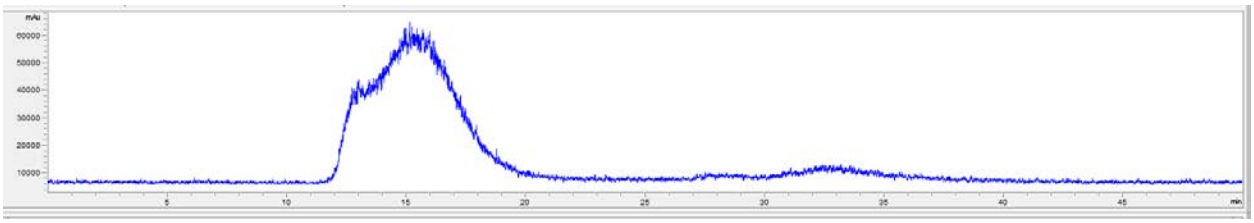

Figure 31. FPLC of Tz-(^{89}Zr) DFO labeled SPION-TCO.

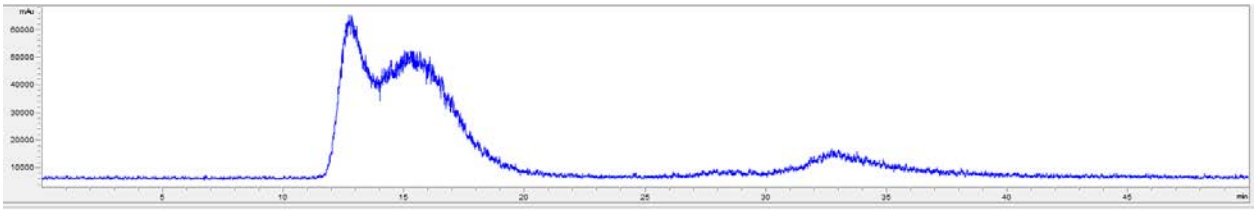

Figure 32. FPLC of Tz-(^{89}Zr)DFO labeled SPION-GOx bioconjugates.

The mice injected with ^{89}Zr labeled SPION-GOx were scanned in PET 1h, 3h, and 24h post injection. The PET images are shown below in Figure 33-34. Biodistribution information was obtained 3h and 24h after the injection and shown in Figure 35-36. The results suggest that SPION-GOx bioconjugates are gradually accumulating in the tumor through 24h.

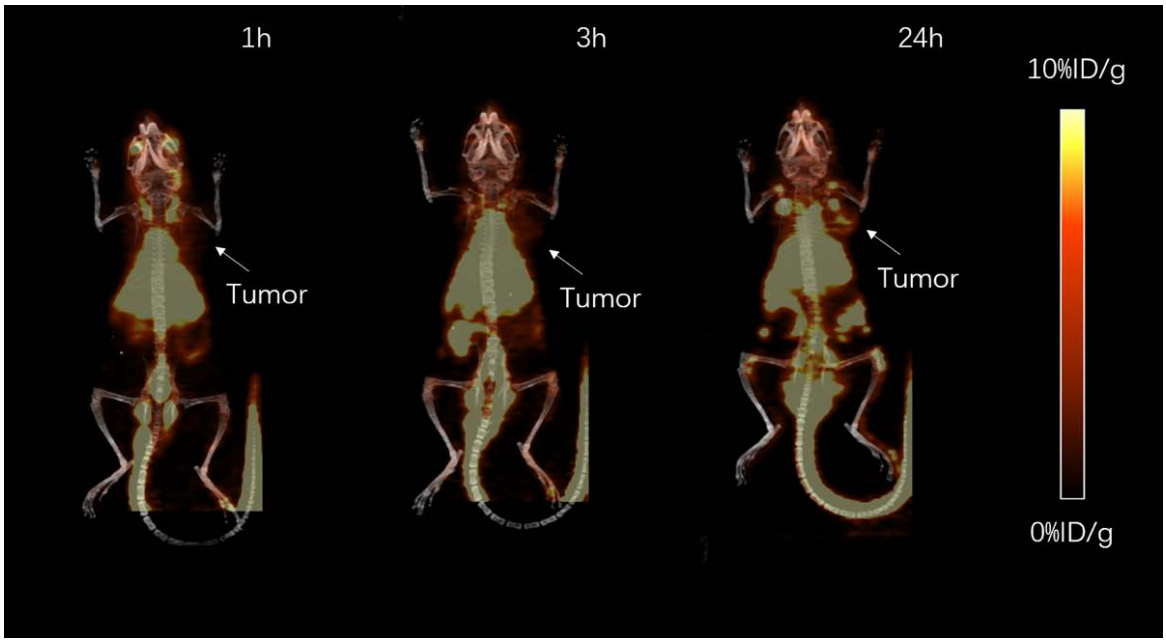

Figure 33. PET imaging of Balb/c mice bearing 4T1 tumors 1h, 3h, 24h post injection of 89Zr labeled SPION-GOx.

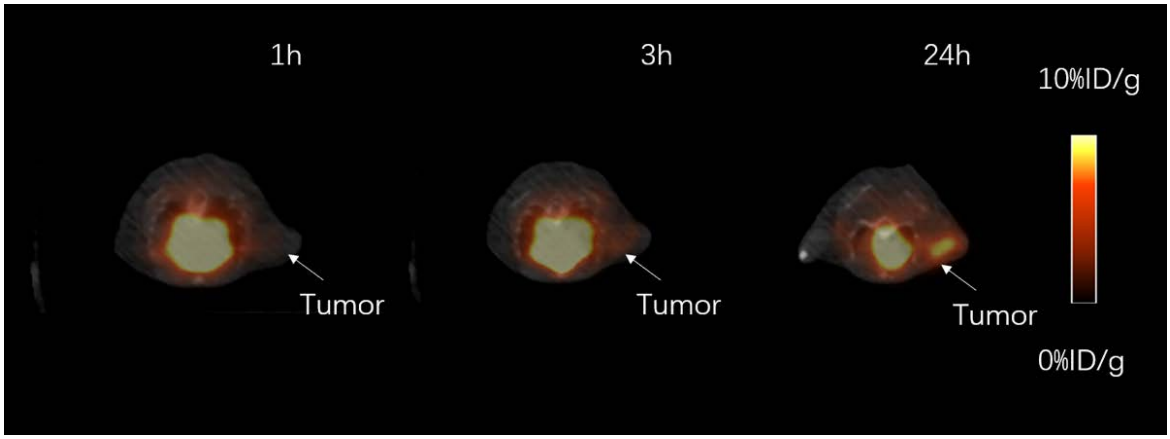

Figure 34. PET imaging of tumor site. 1h, 3h, 24h post injection of 89Zr labeled SPION-GOx.

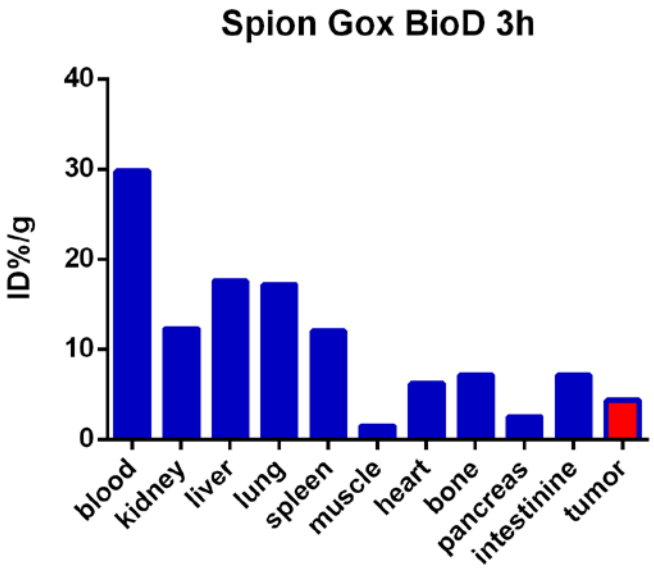

Figure 35. Biodistribution of 89Zr labeled SPION-GOx in major organs 3h after injection.

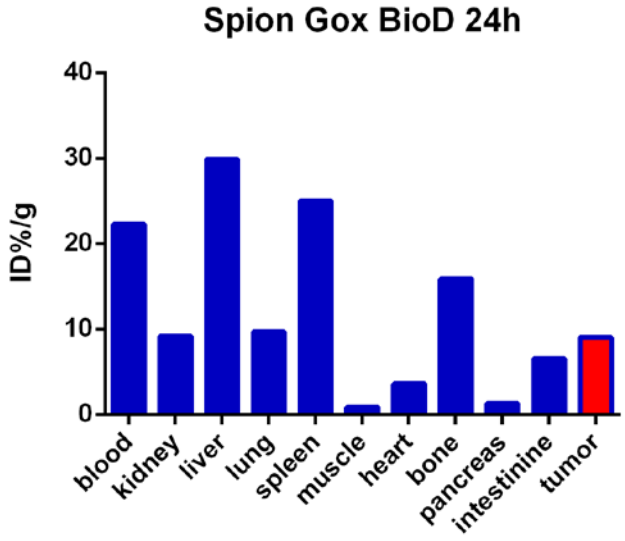

Figure 36. Biodistribution of 89Zr labeled SPION-GOx in major organs 24h after injection.

Increase of radioactivity were observed in some organs other than the tumor, such as kidney, liver, bone, while there was reduction in blood, lung, spleen and pancreas. The amount of SPION-GOx bioconjugates in muscles, heart, and intestine remained at a constant level in the time period of 24 hours. All the three mice in this group were either dead or sacrificed after the 24 h PET scanning.

The other group of two mice were injected with ^{89}Zr labeled SPION using the same procedure, but only PET scanning results were obtained, shown in Figure 37-38. The tumor area became brighter after 24h of injection compared to 1h, indicating the accumulation of SPION in the tumor over time, which is consistent with the trend of SPION-GOx bioconjugates accumulating in this time period. In vivo PET scanning was performed 1h and 24h after the injection. Limited information was obtained from this group because the exact death time of the two mice in this group could not be determined so that the biodistribution obtained from the organs would not be valid.

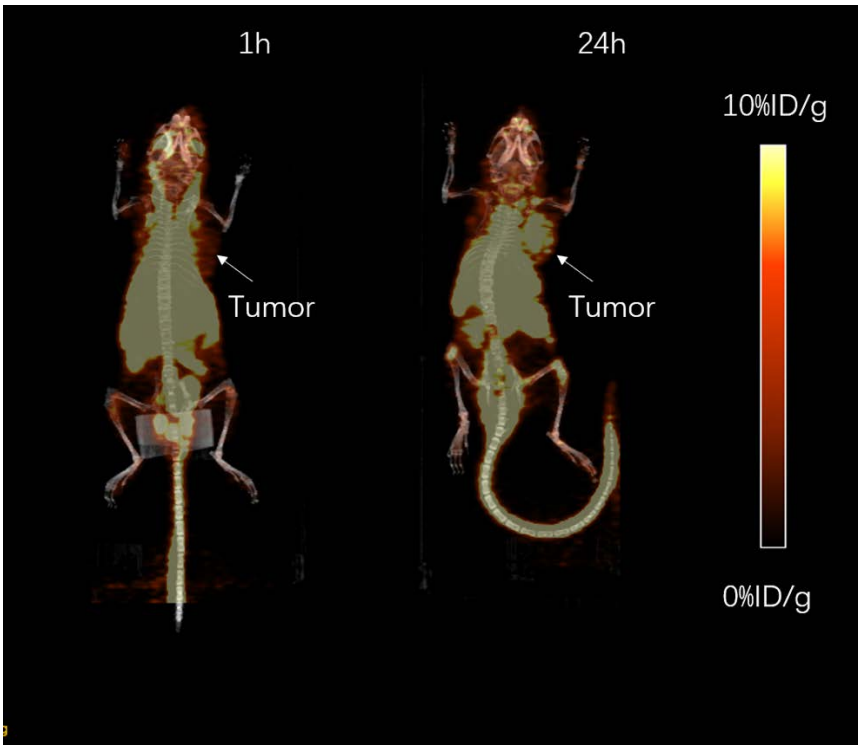

Figure 37. PET imaging of balb/c mice bearing 4T1 tumors: 1h and 24h post-injection of ^{89}Zr labeled SPION.

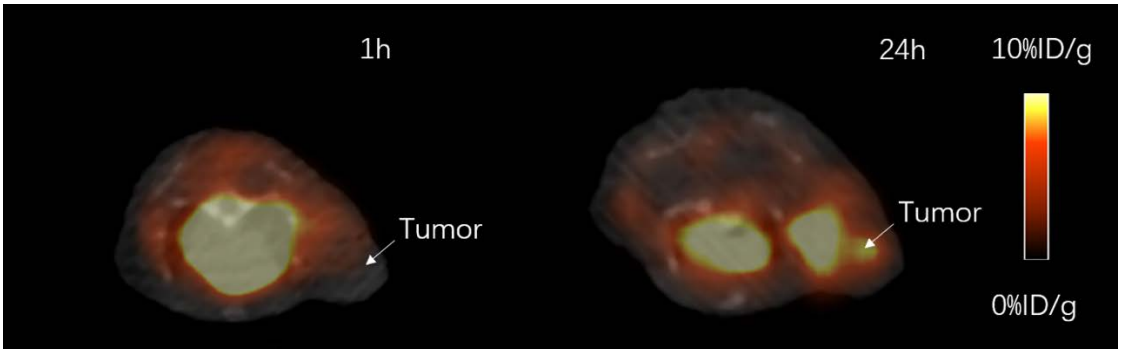

Figure 38. PET imaging of tumor site. 1h and 24h post injection of ^{89}Zr labeled SPION.

4.1.3 Discussion

The biodistribution results and the PET images clearly showed the accumulation of both SPION-GOx and SPION in the tumor over a short time period of 24 hours due to the EPR effect of SPION. This result is very exciting because SPION-GOx bioconjugates can be efficiently delivered to the tumor site without any other modifications with targeting agents like peptides and antibodies, which suggests that this easy and convenient synthesis procedure could be effective. On the other hand, a targeting agent (i.e. peptide or antibody) attached to the bioconjugates could greatly improve the binding specificity of tumor cell, which requires further research in order to establish a pre-targeting 2-step cancer cell destruction system.

Other than the tumor, increase of radioactivity was observed in some major organs, such as kidney, liver, bone as well. At the meantime, there was decrease in blood, lung, spleen and pancreas. The amount of SPION-GOx bioconjugates in muscles, heart, and intestine remained at a relatively constant level during the 24-hour time period. The accumulation in liver is not a major concern since liver has a high tolerance for toxicity. The small drop of SPION-GOx level in blood can be explained by a slow clearance of the large biomolecules. However, the relatively high amount of accumulation in the bone might be a major concern since bone marrow plays the key role in hematopoiesis.

Limited biodistribution information of SPION-GOx and SPION was obtained because the mice in both groups were either dead before a pre-designed time point or had to be sacrificed after the 24 h PET scanning. Further experiments need to be designed and performed to find out the reasons for the inconsistency from the previous *in vivo* cytotoxicity evaluation. The SPION-GOx bioconjugates did not show a very clear cytotoxicity at an even higher dosage of 12.5

mg/kg mouse. The mice administrated with the single dose of 12.5 mg/kg mouse appeared healthy one month after the injection, and no significant weight loss was observed. One of the possible reasons for unexpected death of mice is that the SPION-GOx suspension was not sanitized before the injection. The bacteria and other large size impurities that might exist in the suspension can be removed by simply filtering the suspension with a 0.22 μm membrane filters before the administration. A bacteria test as well as filtration can be conducted to verify that the suspension was safe for injection in the future.

Using ^{89}Zr to label SPION-GOx over other PET isotopes with comparable decay half-lives such as ^{124}I has several advantages. For example, the energy required for ^{89}Zr production is lower[177]. In addition, ^{124}I has a relatively low specificity because ^{124}I links directly to mAbs via tyrosine residues, which can be subjected to dehalogenation *in vivo*. This may lead to significant radioactivity uptake in the organs that are not supposed to be targeted by the mAb-antigen binding[178], whereas ^{89}Zr has the higher specificity realized by the chelator DFO and highly specified conjugation through click chemistry. However, there is limited availability for ^{89}Zr. A major disadvantage of ^{89}Zr is that the gamma emission is at a high energy level of 908.97 keV, which may limit the radioactive dose that can be administered into patients[179].

Overall, PET imaging could be of great use in the future study for acquisition of biodistribution of any system with large biomolecules like nanoparticle or antibodies.

4.2 SUMMARY

Two types of iron oxide nanoparticles, SPION and PAA-MNP have been synthesized via appropriate synthesis and stabilization strategies to meet the needs of desirable size and size distribution, proper functional groups, and great biocompatibility, etc.

The platform using SPION-GOx bioconjugates as a novel approach for ROS-induced cell destruction was demonstrated to be able to effectively produce ROS from H_2O_2 via Fenton's reaction after the oxidation of glucose catalyzed by GOx. TMB assay showed a clear blue color which was characterized in spectroscopy, indicating the generation of large amount of ROS. *In vitro* cell viability assay demonstrated that the SPION-GOx bioconjugates can destruct the tumor cells efficiently, which suggests that the platform could lead to a new cancer therapy with unprecedented low side effect and long-term effectiveness. The *in vivo* cytotoxicity evaluation showed that the balb/c mice can tolerate the bioconjugates with no significant weight loss at a dosage of 5.0 mg/kg mouse. Most importantly, SPION-GOx are able to accumulate in the tumor after 48 hours due to the EPR effect, and release ROS resulting in an oxidative stress that effectively slow down the tumor growth by targeted destruction of cancer cells.

Additionally, MNP that are modified with the temperature responsive pNIPAM to enable the multistage cell separation are capable of enhancing the enrichment factor after a few separation cycles by improving separation efficiency caused by the non-specific interactions between the cells and MNP in traditional MACS system. The multiple capture-and-release cycles was realized by the reversible hydrophobic-hydrophilic interactions between functionalized MNP and target cells. Flow cytometry results suggest that A431 cells (target) could be effectively separated from HeLa cells (non-target) after three separation stages resulting in an

enrichment factor of 3.69 when the starting ratio of target to non-target is 1:2. Even though the separation efficiency was not dramatically enhanced, a lot of parameters in this scheme can potentially be tuned to optimize the system performance, like particle size, polymer density on particle surface, etc.

This work suggests that Fe_3O_4 magnetic nanoparticles are promising material for varieties of biomedical applications like cancer theranostic and cell sorting for their extraordinary characteristics and tons of modification possibilities to meet different requirements in new applications.

BIBLIOGRAPHY

1. Lu, A.H., E.e.L. Salabas, and F. Schüth, *Magnetic nanoparticles: synthesis, protection, functionalization, and application.* Angewandte Chemie International Edition, 2007. **46**(8): p. 1222-1244.

2. Biener, J., et al., *Surface chemistry in nanoscale materials.* Materials, 2009. **2**(4): p. 2404-2428.

3. Gupta, A.K. and M. Gupta, *Synthesis and surface engineering of iron oxide nanoparticles for biomedical applications.* Biomaterials, 2005. **26**(18): p. 3995-4021.

4. Willis, A.L., N.J. Turro, and S. O'Brien, *Spectroscopic Characterization of the Surface of Iron Oxide Nanocrystals.* Chemistry of Materials, 2005. **17**(24): p. 5970-5975.

5. Woo, K., et al., *Sol–Gel Mediated Synthesis of Fe2O3 Nanorods.* Advanced Materials, 2003. **15**(20): p. 1761-1764.

6. Stucki, J.W., B.A. Goodman, and U. Schwertmann, *Iron in soils and clay minerals*. Vol. 217. 2012: Springer Science & Business Media.

7. Laurent, S., et al., *Magnetic iron oxide nanoparticles: synthesis, stabilization, vectorization, physicochemical characterizations, and biological applications.* Chemical reviews, 2008. **108**(6): p. 2064-2110.

8. Jana, N.R., Y. Chen, and X. Peng, *Size- and Shape-Controlled Magnetic (Cr, Mn, Fe, Co, Ni) Oxide Nanocrystals via a Simple and General Approach.* Chemistry of Materials, 2004. **16**(20): p. 3931-3935.

9. Yu, W.W., Y.A. Wang, and X. Peng, *Formation and Stability of Size-, Shape-, and Structure-Controlled CdTe Nanocrystals: Ligand Effects on Monomers and Nanocrystals.* Chemistry of Materials, 2003. **15**(22): p. 4300-4308.

10. Yu, W.W. and X. Peng, *Formation of high ‐quality CdS and other II −VI semiconductor nanocrystals in noncoordinating solvents: tunable reactivity of monomers.* Angewandte Chemie International Edition, 2002. **41**(13): p. 2368-2371.

11. Sun, S. and H. Zeng, *Size-Controlled Synthesis of Magnetite Nanoparticles.* Journal of the American Chemical Society, 2002. **124**(28): p. 8204-8205.

12. Sun, S., et al., *Monodisperse mfe2o4 (m= fe, co, mn) nanoparticles.* Journal of the American Chemical Society, 2004. **126**(1): p. 273-279.

13. Myung, J.H., et al., *Dendrimer‐Mediated Multivalent Binding for the Enhanced Capture of Tumor Cells.* Angewandte Chemie International Edition, 2011. **50**(49): p. 11769-11772.

14. Wu, W., Q. He, and C. Jiang, *Magnetic iron oxide nanoparticles: synthesis and surface functionalization strategies.* Nanoscale research letters, 2008. **3**(11): p. 397.

15. Deng, H., et al., *Monodisperse magnetic single‐crystal ferrite microspheres.* Angewandte Chemie, 2005. **117**(18): p. 2842-2845.

16. Bulte, J.W., et al., *Specific MR imaging of human lymphocytes by monoclonal antibody‐guided dextran‐magnetite particles.* Magnetic resonance in medicine, 1992. **25**(1): p. 148-157.

17. Butterworth, M., L. Illum, and S. Davis, *Preparation of ultrafine silica-and PEG-coated magnetite particles.* Colloids and Surfaces A: Physicochemical and Engineering Aspects, 2001. **179**(1): p. 93-102.

18. Chastellain, M., et al., *Superparamagnetic Silica‐Iron Oxide Nanocomposites for Application in Hyperthermia.* Advanced Engineering Materials, 2004. **6**(4): p. 235-241.

19. Lu, A.-H., et al., *Highly stable carbon-protected cobalt nanoparticles and graphite shells.* Chemical Communications, 2005(1): p. 98-100.

20. Sobal, N.S., et al., *Synthesis and structure of colloidal bimetallic nanocrystals: the non-alloying system Ag/Co.* Nano letters, 2002. **2**(6): p. 621-624.

21. Jeong, J., T.H. Ha, and B.H. Chung, *Enhanced reusability of hexa-arginine-tagged esterase immobilized on gold-coated magnetic nanoparticles.* Analytica Chimica Acta, 2006. **569**(1): p. 203-209.

22. Reddy, L.H., et al., *Magnetic nanoparticles: design and characterization, toxicity and biocompatibility, pharmaceutical and biomedical applications.* Chemical reviews, 2012. **112**(11): p. 5818-5878.

23. Brown, W.J. and M.D. Basil, *Media celebrities and public health: Responses to'Magic'Johnson's HIV disclosure and its impact on AIDS risk and high-risk behaviors.* Health Communication, 1995. **7**(4): p. 345-370.

24. Kievit, F.M., et al., *PEI −PEG −chitosan ‐copolymer ‐coated iron oxide nanoparticles for safe gene delivery: synthesis, complexation, and transfection.* Advanced functional materials, 2009. **19**(14): p. 2244-2251.

25. Gref, R., et al., *'Stealth'corona-core nanoparticles surface modified by polyethylene glycol (PEG): influences of the corona (PEG chain length and surface density) and of the core composition on phagocytic uptake and plasma protein adsorption.* Colloids and Surfaces B: Biointerfaces, 2000. **18**(3): p. 301-313.

26. Shang, H., et al., *Synthesis and characterization of paramagnetic microparticles through emulsion-templated free radical polymerization.* Langmuir, 2006. **22**(6): p. 2516-2522.

27. Flesch, C., et al., *Poly (ethylene glycol) surface coated magnetic particles.* Macromolecular rapid communications, 2005. **26**(18): p. 1494-1498.

28. Gupta, A.K., et al., *Recent advances on surface engineering of magnetic iron oxide nanoparticles and their biomedical applications.* 2007.

29. Larsen, E.K., et al., *Size-dependent accumulation of PEGylated silane-coated magnetic iron oxide nanoparticles in murine tumors.* ACS nano, 2009. **3**(7): p. 1947-1951.

30. Weissleder, R., et al., *Long-circulating iron oxides for MR imaging.* Advanced Drug Delivery Reviews, 1995. **16**(2-3): p. 321-334.

31. Bi, S., et al., *In-situ formation of Fe 3 O 4 nanoparticles within the thermosensitive hairy hybrid particles.* Materials Letters, 2008. **62**(17): p. 2963-2966.

32. Sun, C., J.S. Lee, and M. Zhang, *Magnetic nanoparticles in MR imaging and drug delivery.* Advanced drug delivery reviews, 2008. **60**(11): p. 1252-1265.

33. Lecommandoux, S., et al., *Smart hybrid magnetic self-assembled micelles and hollow capsules.* Progress in Solid State Chemistry, 2006. **34**(2): p. 171-179.

34. Arias, J., et al., *Synthesis and characterization of poly (ethyl-2-cyanoacrylate) nanoparticles with a magnetic core.* Journal of Controlled Release, 2001. **77**(3): p. 309-321.

35. Saravanan, M., et al., *Ultrasonically controlled release and targeted delivery of diclofenac sodium via gelatin magnetic microspheres.* International journal of pharmaceutics, 2004. **283**(1): p. 71-82.

36. Viota, J., et al., *Study of the magnetorheological response of aqueous magnetite suspensions stabilized by acrylic acid polymers.* Journal of colloid and interface science, 2008. **324**(1): p. 199-204.

37. Gómez-Lopera, S.A., et al., *Colloidal stability of magnetite/poly (lactic acid) core/shell nanoparticles.* Langmuir, 2006. **22**(6): p. 2816-2821.

38. Hamoudeh, M., et al., *Elaboration of PLLA-based superparamagnetic nanoparticles: characterization, magnetic behaviour study and in vitro relaxivity evaluation.* International journal of pharmaceutics, 2007. **338**(1): p. 248-257.

39. Cózar-Bernal, M., et al., *Insulin-loaded PLGA microparticles: flow focusing versus double emulsion/solvent evaporation.* Journal of Microencapsulation, 2011. **28**(5): p. 430-441.

40. Liu, X., et al., *Synthesis and characterization of highly-magnetic biodegradable poly (D, L-lactide-co-glycolide) nanospheres.* Journal of Controlled Release, 2007. **119**(1): p. 52-58.

41. Pérez-Artacho, B., et al., *Maghemite/poly (d, l-lactide-co-glycolyde) composite nanoplatform for therapeutic applications.* Journal of Nanoparticle Research, 2012. **14**(4): p. 768.

42. Lee, J., T. Isobe, and M. Senna, *Preparation of Ultrafine Fe3O4Particles by Precipitation in the Presence of PVA at High pH.* Journal of Colloid and Interface Science, 1996. **177**(2): p. 490-494.

43. Kuznetsov, A.A., et al., *Application of magnetic liposomes for magnetically guided transport of muscle relaxants and anti-cancer photodynamic drugs.* Journal of Magnetism and Magnetic Materials, 2001. **225**(1): p. 95-100.

44. Peira, E., et al., *In vitro and in vivo study of solid lipid nanoparticles loaded with superparamagnetic iron oxide.* Journal of drug targeting, 2003. **11**(1): p. 19-24.

45. De Cuyper, M., et al., *Synthesis of magnetic Fe3O4 particles covered with a modifiable phospholipid coat.* Journal of Physics: Condensed Matter, 2003. **15**(15): p. S1425.

46. Cevc, G. and H. Richardsen, *Lipid vesicles and membrane fusion.* Advanced Drug Delivery Reviews, 1999. **38**(3): p. 207-232.

47. De Cuyper, M. and M. Joniau, *Magnetoliposomes.* European Biophysics Journal, 1988. **15**(5): p. 311-319.

48. Pankhurst, Q.A., et al., *Applications of magnetic nanoparticles in biomedicine.* Journal of physics D: Applied physics, 2003. **36**(13): p. R167.

49. O'Brien, M.E.R., et al., *Reduced cardiotoxicity and comparable efficacy in a phase III trial of pegylated liposomal doxorubicin HCl (CAELYX (TM)/Doxil (R)) versus conventional doxorubicin for first-line treatment of metastatic breast cancer.* Annals of Oncology, 2004. **15**(3): p. 440-449.

50. Häfeli, U.O., et al., *Magnetically targeted microspheres for intracavitary and intraspinal Y-90 radiotherapy*, in *Scientific and clinical applications of magnetic carriers*. 1997, Springer. p. 501-516.

51. Jun, Y.-w., et al., *Nanoscale Size Effect of Magnetic Nanocrystals and Their Utilization for Cancer Diagnosis via Magnetic Resonance Imaging.* Journal of the American Chemical Society, 2005. **127**(16): p. 5732-5733.

52. Widder, K.J., A.E. Senyei, and D.G. Scarpelli, *Magnetic microspheres: a model system for site specific drug delivery in vivo.* Proceedings of the Society for Experimental Biology and Medicine, 1978. **158**(2): p. 141-146.

53. McBain, S.C., H.H. Yiu, and J. Dobson, *Magnetic nanoparticles for gene and drug delivery.* International journal of nanomedicine, 2008. **3**(2): p. 169.

54. Mah, C., et al., *Improved method of recombinant AAV2 delivery for systemic targeted gene therapy.* Molecular Therapy, 2002. **6**(1): p. 106-112.

55. Abdallah, B., et al., *A powerful nonviral vector for in vivo gene transfer into the adult mammalian brain: polyethylenimine.* Human gene therapy, 1996. **7**(16): p. 1947-1954.

56. Sun, C., J.S.H. Lee, and M. Zhang, *Magnetic nanoparticles in MR imaging and drug delivery.* Advanced Drug Delivery Reviews, 2008. **60**(11): p. 1252-1265.

57. Wilson, M.W., et al., *Hepatocellular carcinoma: regional therapy with a magnetic targeted carrier bound to doxorubicin in a dual MR imaging/conventional angiography suite—initial experience with four patients.* Radiology, 2004. **230**(1): p. 287-293.

58. Rudge, S., et al., *Adsorption and desorption of chemotherapeutic drugs from a magnetically targeted carrier (MTC).* Journal of Controlled Release, 2001. **74**(1): p. 335-340.

59. Chatterjee, D.K., P. Diagaradjane, and S. Krishnan, *Nanoparticle-mediated hyperthermia in cancer therapy.* Therapeutic delivery, 2011. **2**(8): p. 1001-1014.

60. Bass, H., J. Moore, and W. Coakley, *Lethality in mammalian cells due to hyperthermia under oxic and hypoxic conditions.* International Journal of Radiation Biology and Related Studies in Physics, Chemistry and Medicine, 1978. **33**(1): p. 57-67.

61. Brigger, I., C. Dubernet, and P. Couvreur, *Nanoparticles in cancer therapy and diagnosis.* Advanced Drug Delivery Reviews, 2002. **54**(5): p. 631-651.

62. Hiergeist, R., et al., *Application of magnetite ferrofluids for hyperthermia.* Journal of Magnetism and Magnetic Materials, 1999. **201**(1): p. 420-422.

63. Balivada, S., et al., *A/C magnetic hyperthermia of melanoma mediated by iron (0)/iron oxide core/shell magnetic nanoparticles: a mouse study.* BMC cancer, 2010. **10**(1): p. 119.

64. Elsherbini, A.A., et al., *Magnetic nanoparticle-induced hyperthermia treatment under magnetic resonance imaging.* Magnetic resonance imaging, 2011. **29**(2): p. 272-280.

65. Dale, B.M., M.A. Brown, and R.C. Semelka, *MRI: basic principles and applications*. 2015: John Wiley & Sons.

66. Semelka, R.C. and T.K. Helmberger, *Contrast agents for MR imaging of the liver.* Radiology, 2001. **218**(1): p. 27-38.

67. Harisinghani, M.G., et al., *Noninvasive detection of clinically occult lymph-node metastases in prostate cancer.* New England Journal of Medicine, 2003. **348**(25): p. 2491-2499.

68. Enochs, W.S., et al., *Improved delineation of human brain tumors on MR images using a long‐circulating, superparamagnetic iron oxide agent.* Journal of Magnetic Resonance Imaging, 1999. **9**(2): p. 228-232.

69. Varallyay, P., et al., *Comparison of two superparamagnetic viral-sized iron oxide particles ferumoxides and ferumoxtran-10 with a gadolinium chelate in imaging intracranial tumors.* American Journal of Neuroradiology, 2002. **23**(4): p. 510-519.

70. Xu, C., et al., *Dopamine as A Robust Anchor to Immobilize Functional Molecules on the Iron Oxide Shell of Magnetic Nanoparticles.* Journal of the American Chemical Society, 2004. **126**(32): p. 9938-9939.

71. Gu, H., et al., *Biofunctional magnetic nanoparticles for protein separation and pathogen detection.* Chemical Communications, 2006(9): p. 941-949.

72. Zhao, X., et al., *Collection of Trace Amounts of DNA/mRNA Molecules Using Genomagnetic Nanocapturers.* Analytical Chemistry, 2003. **75**(14): p. 3476-3483.

73. Šafařík, I. and M. Šafaříková, *Use of magnetic techniques for the isolation of cells.* Journal of Chromatography B: Biomedical Sciences and Applications, 1999. **722**(1): p. 33-53.

74. Chen, L.X., et al., *Fe2O3 nanoparticle structures investigated by X-ray absorption near-edge structure, surface modifications, and model calculations.* The Journal of Physical Chemistry B, 2002. **106**(34): p. 8539-8546.

75. Rajh, T., et al., *Surface Restructuring of Nanoparticles: An Efficient Route for Ligand−Metal Oxide Crosstalk.* The Journal of Physical Chemistry B, 2002. **106**(41): p. 10543-10552.

76. Kamata, H. and H. Hirata, *Redox regulation of cellular signalling.* Cellular signalling, 1999. **11**(1): p. 1-14.

77. Ueda, S., et al., *Redox control of cell death.* Antioxidants and Redox Signaling, 2002. **4**(3): p. 405-414.

78. Inoue, M., et al., *Mitochondrial generation of reactive oxygen species and its role in aerobic life.* Current medicinal chemistry, 2003. **10**(23): p. 2495-2505.

79. Pastor, N., et al., *A detailed interpretation of OH radical footprints in a TBP-DNA complex reveals the role of dynamics in the mechanism of sequence-specific binding.* Journal of molecular biology, 2000. **304**(1): p. 55-68.

80. Wang, J. and J. Yi, *Cancer cell killing via ROS: to increase or decrease, that is the question.* Cancer Biol Ther, 2008. **7**(12): p. 1875-84.

81. Li, X., et al., *Targeting mitochondrial reactive oxygen species as novel therapy for inflammatory diseases and cancers.* Journal of Hematology & Oncology, 2013. **6**: p. 19-19.

82. Crichton, R.R. and M. Charloteaux-Wauters, *Iron transport and storage.* European Journal of Biochemistry, 1987. **164**(3): p. 485-506.

83. Winterbourn, C.C., *Toxicity of iron and hydrogen peroxide: the Fenton reaction.* Toxicology letters, 1995. **82**: p. 969-974.

84. Linnane, A.W. and H. Eastwood, *Cellular redox regulation and prooxidant signaling systems.* Annals of the New York Academy of Sciences, 2006. **1067**(1): p. 47-55.

85. Fruehauf, J.P. and F.L. Meyskens, *Reactive oxygen species: a breath of life or death?* Clinical Cancer Research, 2007. **13**(3): p. 789-794.

86. Fiers, W., et al., *More than one way to die: apoptosis, necrosis and reactive oxygen damage.* Oncogene, 1999. **18**(54): p. 7719-7730.

87. Matés, J.M. and F.M. Sánchez-Jiménez, *Role of reactive oxygen species in apoptosis: implications for cancer therapy.* The International Journal of Biochemistry & Cell Biology, 2000. **32**(2): p. 157-170.

88. Ozben, T., *Oxidative stress and apoptosis: impact on cancer therapy.* J Pharm Sci, 2007. **96**(9): p. 2181-96.

89. Valko, M., et al., *Free radicals, metals and antioxidants in oxidative stress-induced cancer.* Chemico-biological interactions, 2006. **160**(1): p. 1-40.

90. Sikka, S.C., *Role of oxidative stress response elements and antioxidants in prostate cancer pathobiology and chemoprevention--a mechanistic approach.* Current medicinal chemistry, 2003. **10**(24): p. 2679-2692.

91. Stoler, D.L., *The hallmarks of cancer.* Cell, 2000. **100**: p. 57-70.

92. Benhar, M., D. Engelberg, and A. Levitzki, *ROS, stress‐activated kinases and stress signaling in cancer.* EMBO reports, 2002. **3**(5): p. 420-425.

93. Li, C.-Y., et al., *Initial stages of tumor cell-induced angiogenesis: evaluation via skin window chambers in rodent models.* Journal of the National Cancer Institute, 2000. **92**(2): p. 143-147.

94. Peng, X. and V. Gandhi, *ROS-activated anticancer prodrugs: a new strategy for tumor-specific damage.* Therapeutic delivery, 2012. **3**(7): p. 823-833.

95. Dearnaley, D.P., et al., *Comparison of radiation side-effects of conformal and conventional radiotherapy in prostate cancer: a randomised trial.* The Lancet, 1999. **353**(9149): p. 267-272.

96. Peeters, K.C.M.J., et al., *Late Side Effects of Short-Course Preoperative Radiotherapy Combined With Total Mesorectal Excision for Rectal Cancer: Increased Bowel Dysfunction in Irradiated Patients—A Dutch Colorectal Cancer Group Study.* Journal of Clinical Oncology, 2005. **23**(25): p. 6199-6206.

97. Shafiq, J., et al., *An international review of patient safety measures in radiotherapy practice.* Radiotherapy and Oncology, 2009. **92**(1): p. 15-21.

98. Barnett, G.C., et al., *Normal tissue reactions to radiotherapy: towards tailoring treatment dose by genotype.* Nat Rev Cancer, 2009. **9**(2): p. 134-142.

99. Dolmans, D.E.J.G.J., D. Fukumura, and R.K. Jain, *Photodynamic therapy for cancer.* Nat Rev Cancer, 2003. **3**(5): p. 380-387.

100. Pass, H.I., *Photodynamic Therapy in Oncology: Mechanisms and Clinical Use.* Journal of the National Cancer Institute, 1993. **85**(6): p. 443-456.

101. Castano, A.P., P. Mroz, and M.R. Hamblin, *Photodynamic therapy and anti-tumour immunity.* Nat Rev Cancer, 2006. **6**(7): p. 535-545.

102. Kashtan, H., et al., *Photodynamic therapy of colorectal cancer using a new light source - From in vitro studies to a patient treatment.* Diseases of the Colon & Rectum, 1996. **39**(4): p. 379-383.

103. Brown, S.B., E.A. Brown, and I. Walker, *The present and future role of photodynamic therapy in cancer treatment.* The Lancet Oncology, 2004. **5**(8): p. 497-508.

104. Allison, R.R., et al., *Photosensitizers in clinical PDT.* Photodiagnosis and Photodynamic Therapy, 2004. **1**(1): p. 27-42.

105. Huang, G., et al., *Superparamagnetic iron oxide nanoparticles: amplifying ROS stress to improve anticancer drug efficacy.* Theranostics, 2013. **3**(2): p. 116-26.

106. Zhou, Z., et al., *Activatable Singlet Oxygen Generation from Lipid Hydroperoxide Nanoparticles for Cancer Therapy.* Angewandte Chemie, 2017. **129**(23): p. 6592-6596.

107. Le Bras, M., et al., *Reactive oxygen species and the mitochondrial signaling pathway of cell death.* Histology and histopathology, 2005. **20**(1): p. 205-219.

108. Fleury, C., B. Mignotte, and J.-L. Vayssière, *Mitochondrial reactive oxygen species in cell death signaling.* Biochimie, 2002. **84**(2): p. 131-141.

109. Liu, J., et al., *Suppression of the malignant phenotype in pancreatic cancer by overexpression of phospholipid hydroperoxide glutathione peroxidase.* Human gene therapy, 2006. **17**(1): p. 105-116.

110. Brenner, C. and S. Grimm, *The permeability transition pore complex in cancer cell death.* Oncogene, 2006. **25**(34): p. 4744-4756.

111. Petronilli, V., et al., *The voltage sensor of the mitochondrial permeability transition pore is tuned by the oxidation-reduction state of vicinal thiols. Increase of the gating potential by oxidants and its reversal by reducing agents.* Journal of Biological Chemistry, 1994. **269**(24): p. 16638-16642.

112. Chakraborti, T., et al., *Oxidant, mitochondria and calcium: an overview.* Cellular signalling, 1999. **11**(2): p. 77-85.

113. Chandra, J., et al., *Resistance of leukemic cells to 2-chlorodeoxyadenosine is due to a lack of calcium-dependent cytochrome c release.* Blood, 2002. **99**(2): p. 655-663.

114. Singletary, S.E., et al., *Revision of the American Joint Committee on Cancer staging system for breast cancer.* Journal of clinical oncology, 2002. **20**(17): p. 3628-3636.

115. Brugger, W., et al., *MOBILIZATION OF TUMOR-CELLS AND HEMATOPOIETIC PROGENITOR CELLS INTO PERIPHERAL-BLOOD OF PATIENTS WITH SOLID TUMORS.* Blood, 1994. **83**(3): p. 636-640.

116. Fisher, E.R. and R.B. Turnbull, *THE CYTOLOGIC DEMONSTRATION AND SIGNIFICANCE OF TUMOR CELLS IN THE MESENTERIC VENOUS BLOOD IN PATIENTS WITH COLORECTAL CARCINOMA.* Surgery Gynecology & Obstetrics, 1955. **100**(1): p. 102-108.

117. Leather, A.J., et al., *Detection and enumeration of circulating tumour cells in colorectal cancer.* Br J Surg, 1993. **80**(6): p. 777-80.

118. Almeida, M., A.C. García-Montero, and A. Orfao, *Cell Purification: A New Challenge for Biobanks.* Pathobiology, 2014. **81**(5-6): p. 261-275.

119. Kuhara, M., et al., *Magnetic cell separation using antibody binding with protein A expressed on bacterial magnetic particles.* Analytical chemistry, 2004. **76**(21): p. 6207-6213.

120. Fotouhi, N., et al., *Carotenoid and tocopherol concentrations in plasma, peripheral blood mononuclear cells, and red blood cells after long-term beta-carotene supplementation in men.* The American journal of clinical nutrition, 1996. **63**(4): p. 553-558.

121. Chesney, J., et al., *The peripheral blood fibrocyte is a potent antigen-presenting cell capable of priming naive T cells in situ.* Proceedings of the National Academy of Sciences, 1997. **94**(12): p. 6307-6312.

122. Parks, D. and L. Herzenberg, *[19] Fluorescence-activated cell sorting: Theory, experimental optimization, and applications in lymphoid cell biology*. Methods in enzymology, 1984. **108**: p. 197-241.

123. Hulett, H.R., et al., *Cell sorting: automated separation of mammalian cells as a function of intracellular fluorescence.* Science, 1969. **166**(3906): p. 747-749.

124. Davey, H.M. and D.B. Kell, *Flow cytometry and cell sorting of heterogeneous microbial populations: the importance of single-cell analyses.* Microbiological reviews, 1996. **60**(4): p. 641-696.

125. Johnson, K., M. Dooner, and P. Quesenberry, *Fluorescence activated cell sorting: a window on the stem cell.* Current pharmaceutical biotechnology, 2007. **8**(3): p. 133-139.

126. Paterlini-Brechot, P. and N.L. Benali, *Circulating tumor cells (CTC) detection: clinical impact and future directions.* Cancer letters, 2007. **253**(2): p. 180-204.

127. Maeda, H., et al., *Tumor vascular permeability and the EPR effect in macromolecular therapeutics: a review*. Journal of controlled release, 2000. **65**(1): p. 271-284.

128. Alexis, F., et al., *Factors affecting the clearance and biodistribution of polymeric nanoparticles.* Molecular pharmaceutics, 2008. **5**(4): p. 505-515.

129. Rejman, J., et al., *Size-dependent internalization of particles via the pathways of clathrin- and caveolae-mediated endocytosis.* Biochemical Journal, 2004. **377**(1): p. 159-169.

130. Gatenby, R.A. and R.J. Gillies, *Why do cancers have high aerobic glycolysis?* Nat Rev Cancer, 2004. **4**(11): p. 891-899.

131. Kim, J.-w. and C.V. Dang, *Cancer's Molecular Sweet Tooth and the Warburg Effect.* Cancer Research, 2006. **66**(18): p. 8927-8930.

132. Wan, S., et al., *Size-controlled preparation of magnetite nanoparticles in the presence of graft copolymers.* Journal of Materials Chemistry, 2006. **16**(3): p. 298-303.

133. Si, S., et al., *Magnetic Monodisperse Fe3O4 Nanoparticles.* Crystal Growth & Design, 2005. **5**(2): p. 391-393.

134. Tong, S., et al., *Coating optimization of superparamagnetic iron oxide nanoparticles for high T2 relaxivity.* Nano letters, 2010. **10**(11): p. 4607-4613.

135. Patnaik, P., *Handbook of inorganic chemicals*. Vol. 529. 2003: McGraw-Hill New York.

136. Sun, S.H., et al., *Monodisperse MFe2O4 (M = Fe, Co, Mn) nanoparticles.* Journal of the American Chemical Society, 2004. **126**(1): p. 273-279.

137. Birdi, K., *Handbook of surface and colloid chemistry*. 2002: CRC Press.

138. Chu, B., *Laser light scattering: basic principles and practice*. 2007: Courier Corporation.

139. Josephy, P.D., T. Eling, and R.P. Mason, *The horseradish peroxidase-catalyzed oxidation of 3,5,3',5'-tetramethylbenzidine. Free radical and charge-transfer complex intermediates.* Journal of Biological Chemistry, 1982. **257**(7): p. 3669-75.

140. Gao, L.Z., et al., *Intrinsic peroxidase-like activity of ferromagnetic nanoparticles.* Nature Nanotechnology, 2007. **2**(9): p. 577-583.

141. Gao, L.Z., et al., *Magnetite nanoparticle-linked immunosorbent assay.* Journal of Physical Chemistry C, 2008. **112**(44): p. 17357-17361.

142. Johnsson, M., P. Hansson, and K. Edwards, *Spherical micelles and other self-assembled structures in dilute aqueous mixtures of poly (ethylene glycol) lipids.* The Journal of Physical Chemistry B, 2001. **105**(35): p. 8420-8430.

143. Douglas, G.C. and B.F. King, *Isolation of pure villous cytotrophoblast from term human placenta using immunomagnetic microspheres.* Journal of Immunological Methods, 1989. **119**(2): p. 259-268.

144. Miltenyi, S., et al., *High gradient magnetic cell separation with MACS.* Cytometry Part A, 1990. **11**(2): p. 231-238.

145. Šafařík, I. and M. Šafaříková, *Use of magnetic techniques for the isolation of cells.* Journal of Chromatography B: Biomedical Sciences and Applications, 1999. **722**(1-2): p. 33-53.

146. Ring, A., I.E. Smith, and M. Dowsett, *Circulating tumour cells in breast cancer*. The Lancet Oncology, 2004. **5**(2): p. 79-88.

147. Miller, M.C., G.V. Doyle, and L.W. Terstappen, *Significance of circulating tumor cells detected by the CellSearch system in patients with metastatic breast colorectal and prostate cancer*. Journal of oncology, 2010. **2010**.

148. Zhao, Y., D. Xu, and W. Tan, *Aptamer-functionalized nano/micro-materials for clinical diagnosis: isolation, release and bioanalysis of circulating tumor cells.* Integrative Biology, 2017. **9**(3): p. 188-205.

149. Hoshino, K., et al., *Microchip-based immunomagnetic detection of circulating tumor cells.* Lab on a Chip, 2011. **11**(20): p. 3449-3457.

150. Wan, Y., et al., *Capture, isolation and release of cancer cells with aptamer-functionalized glass bead array.* Lab on a Chip, 2012. **12**(22): p. 4693-4701.

151. Riethdorf, S., et al., *Detection of Circulating Tumor Cells in Peripheral Blood of Patients with Metastatic Breast Cancer: A Validation Study of the CellSearch System.* Clinical Cancer Research, 2007. **13**(3): p. 920-928.

152. Fehm, T., et al., *Methods for isolating circulating epithelial cells and criteria for their classification as carcinoma cells.* Cytotherapy, 2005. **7**(2): p. 171-185.

153. Kodituwakku, A.P., et al., *Isolation of antigen‐specific B cells.* Immunology & Cell Biology, 2003. **81**(3): p. 163-170.

154. Chalmers, J., et al., *Quantification of non‐specific binding of magnetic micro‐and nanoparticles using cell tracking velocimetry: Implication for magnetic cell separation and detection.* Biotechnology and bioengineering, 2010. **105**(6): p. 1078-1093.

155. Shamim, N., et al., *Thermosensitive polymer coated nanomagnetic particles for separation of bio-molecules.* Separation and purification technology, 2007. **53**(2): p. 164-170.

156. Yoshizako, K., et al., *Regulation of protein binding toward a ligand on chromatographic matrixes by masking and forced-releasing effects using thermoresponsive polymer.* Analytical chemistry, 2002. **74**(16): p. 4160-4166.

157. Cobo, I., et al., *Smart hybrid materials by conjugation of responsive polymers to biomacromolecules.* Nature materials, 2015. **14**(2): p. 143.

158. Okamura, A., et al., *Poly (N-isopropylacrylamide)-graft-polypropylene membranes containing adsorbed antibody for cell separation.* Biomaterials, 2005. **26**(11): p. 1287-1292.

159. Cooperstein, M.A. and H.E. Canavan, *Biological cell detachment from poly (N-isopropyl acrylamide) and its applications.* Langmuir, 2009. **26**(11): p. 7695-7707.

160. Zheng, Y., et al., *Harvesting microalgae using the temperature-activated phase transition of thermoresponsive polymers.* Algal Research, 2015. **11**: p. 90-94.

161. Schild, H.G., *Poly (N-isopropylacrylamide): experiment, theory and application.* Progress in polymer science, 1992. **17**(2): p. 163-249.

162. Zhang, F., et al., *Quantification of epidermal growth factor receptor expression level and binding kinetics on cell surfaces by surface plasmon resonance imaging.* Analytical chemistry, 2015. **87**(19): p. 9960-9965.

163. Goldstein, N.I., et al., *Biological efficacy of a chimeric antibody to the epidermal growth factor receptor in a human tumor xenograft model.* Clinical Cancer Research, 1995. **1**(11): p. 1311-1318.

164. Zhu, J., et al., *Specific capture and temperature-mediated release of cells in an aptamer-based microfluidic device.* Lab on a Chip, 2012. **12**(18): p. 3504-3513.

165. Turkova, J., *Oriented immobilization of biologically active proteins as a tool for revealing protein interactions and function.* Journal of Chromatography B: Biomedical Sciences and Applications, 1999. **722**(1): p. 11-31.

166. Chen, J.P., H.J. Yang, and A.S. Huffman, *Polymer-protein conjugates: I. Effect of protein conjugation on the cloud point of poly (N-isopropylacrylamide).* Biomaterials, 1990. **11**(9): p. 625-630.

167. Wu, J., L. Gao, and D. Gao, *Multistage magnetic separation of microspheres enabled by temperature-responsive polymers.* ACS applied materials & interfaces, 2012. **4**(6): p. 3041-3046.

168. Ke, S., et al., *Near-infrared optical imaging of epidermal growth factor receptor in breast cancer xenografts.* Cancer research, 2003. **63**(22): p. 7870-7875.

169. Lederer, C.M. and V.S. Shirley, *Table of isotopes 7th ed.* New York, 1978.

170. Verel, I., et al., *Long-lived positron emitters zirconium-89 and iodine-124 for scouting of therapeutic radioimmunoconjugates with PET.* Cancer Biotherapy and Radiopharmaceuticals, 2003. **18**(4): p. 655-661.

171. Meijs, W.E., et al., *Evaluation of desferal as a bifunctional chelating agent for labeling antibodies with Zr-89.* International journal of radiation applications and instrumentation. Part A. Applied radiation and isotopes, 1992. **43**(12): p. 1443-1447.

172. Vugts, D.J., et al., *Comparison of the octadentate bifunctional chelator DFO*-pPhe-NCS and the clinically used hexadentate bifunctional chelator DFO-pPhe-NCS for 89Zr-immuno-PET.* European journal of nuclear medicine and molecular imaging, 2017. **44**(2): p. 286-295.

173. Perk, L.R., et al., *p-Isothiocyanatobenzyl-desferrioxamine: a new bifunctional chelate for facile radiolabeling of monoclonal antibodies with zirconium-89 for immuno-PET imaging.* European journal of nuclear medicine and molecular imaging, 2010. **37**(2): p. 250-259.

174. Deri, M.A., et al., *PET imaging with 89 Zr: from radiochemistry to the clinic.* Nuclear medicine and biology, 2013. **40**(1): p. 3-14.

175. Tinianow, J.N., et al., *Site-specifically 89 Zr-labeled monoclonal antibodies for ImmunoPET.* Nuclear medicine and biology, 2010. **37**(3): p. 289-297.

176. Zeglis, B.M., et al., *Modular strategy for the construction of radiometalated antibodies for positron emission tomography based on inverse electron demand diels–alder click chemistry.* Bioconjugate chemistry, 2011. **22**(10): p. 2048-2059.

177. Nayak, T.K. and M.W. Brechbiel, *Radioimmunoimaging with longer-lived positron-emitting radionuclides: potentials and challenges.* Bioconjugate chemistry, 2009. **20**(5): p. 825-841.

178. Koehler, L., et al., *Iodine-124: a promising positron emitter for organic PET chemistry.* Molecules, 2010. **15**(4): p. 2686-2718.

179. Zhang, Y., H. Hong, and W. Cai, *PET tracers based on Zirconium-89.* Current radiopharmaceuticals, 2011. **4**(2): p. 131-139.